Master's thesis

NTNU
Norwegian University of Science and Technology
Faculty of Natural Sciences
Department of Biotechnology and Food Science

Spyridon Damigos

Migration of T-cells in a multi-compartment hydrogel model of inflammation

Master's thesis in Biotechnology
Supervisor: Berit Løkensgard Strand
May 2020

NTNU
Norwegian University of
Science and Technology

Spyridon Damigos

Migration of T-cells in a multi-compartment hydrogel model of inflammation

Master's thesis in Biotechnology
Supervisor: Berit Løkensgard Strand
May 2020

Norwegian University of Science and Technology
Faculty of Natural Sciences
Department of Biotechnology and Food Science

NTNU
Kunnskap for en bedre verden

Preface

The current master thesis project was conducted at the Norwegian University of Science and Technology (NTNU) in Trondheim, Norway. Chemical modification of alginates and fundamental work on the biomaterials was conducted at the Norwegian Biopolymer Laboratory (NOBIPOL). All cell lines were kindly provided by Professor Øyvind Halaas, Department of Clinical and Molecular Medicine, NTNU, Trondheim. Cell culture was mainly conducted at the cell lab of the Department of Biotechnology and Food Science NTNU, Trondheim. Imaging took place at the Department of Physics, NTNU, Trondheim.

I would like to express my deep gratitude to my supervisor Professor Berit Løkensgard Strand and co-supervisor Professor Øyvind Halaas for their invaluable support and giving me the opportunity to participate in this amazing work. Special thanks should be given to my co-supervisor Post-Doc researcher Daria Zaytseva-Zotova for her constructive suggestions and guidance during this work. I would also like to offer my thanks to Post-Doc Researcher Aman Singh Chahal for his concrete feedback.

A big thanks to all the PhD students and engineers that accommodated me in the laboratories and contributed to my training.

Finally, I would like to deeply thank my family.

Special statement:

Due to Covid19 pandemic the access to the campus and the laboratories was limited. The work got affected and further valuable experimentation was restricted.

Abstract

In the present work multi-compartmental hydrogels were established in order to study T-cell migration in 3D. The main approach that was developed for the fabrication of the hydrogel systems, was based on the incorporation of an alginate compartment with an encapsulated bioactive factor, in a surrounding 3D matrix composed of collagen type-I, Matrigel or chemically modified alginate.

The resulted hydrogels were used as 3D *in vitro* platforms, in order to evaluate the migration of T-cells under the influence of pro-inflammatory mediators secreted by stimulated dendritic cells (DCs). DCs where encapsulated into the alginate together with lipopolysaccharide LPS that resulted to the activation of the TLR4 pathway, followed by the secretion of pro-inflammatory mediators. The stimulation of the DCs regulated the migration of the T-cell hybridomas embedded in the surrounding scaffolds. The multi-compartmental hydrogel system was successfully used to demonstrate migration in collagen type-I and Matrigel.

The activity of T-cell hybridomas in response to pro-inflammatory mediators was monitored in fibrillar collagen type-I matrix for the timepoints of 0h, 4h, 6h, 8h, 24h and 48h after the system was assembled, with live cell imaging. The results suggested an elevated accumulation around the alginate compartment throughout time in respect to the inflamed microenvironment that was exponentially increased at 48h. The migration in collagen-type I was in addition quantitated by automated cell tracking at the aforementioned timepoints. No significant differences were observed in terms of migrated distances and cell speed during the first 24h while at 48h the values were significantly increased. In general, the results indicated an increased migration of T-cell hybridomas under the influence of pro-inflammatory mediators with most critical timepoint that of 48h. The motility behavior of T-cell hybridomas was analyzed by mean squared displacement analysis and further discussed.

For multi-compartmental hydrogels where Matrigel was employed as a surrounding scaffold imaging took place at 0h and 96h. The T-cell hybridomas were shown to conglomerate forming a distinguishable line at the edge of the alginate structure at 96h under the presence of activated DCs. The results have indicated a directional migration to the endotoxin stimulated source. The same system was assessed in chemically modified alginates as a surrounding matrix. No activity was demonstrated in sulfated and partially oxidized-reduced (POAred) alginate hydrogels.

Pilot experiments were conducted in RGD-alginate hydrogels of different weight average molecular weight (M_w) compositions. The migration of T-cell hybridomas was recorded in both and M_w compositions. After one day of incubation the migration was increased within the hydrogels of both M_w compositions. The increased motility in the scaffolds after one day could be relevant to transitions that took place in the alginate network and altered the hydrogel architecture.

Lastly, a comparison in T-cell hybridomas morphology during migration in the different biomaterial scaffolds. Cell morphology was found to meet different attributes between the different biomaterials and could be linked to the surrounding matrix architecture.

In conclusion, multi-compartmental hydrogels based on fibrillar collagen and Matrigel with encapsulated alginate microstructures were successfully produced as an *in vitro* platform in order to study T-cell migration in 3D under the influence of an innate immune response. Alginate can be a good surrounding scaffold candidate in future setups since migration of T-cell hybridomas was determined within the hydrogels.

List of Abbreviations

DC	Dendritic cell
LPS	Lipopolysaccharide
M_w	Weight average molecular weight
POAred	Partially oxidized and reduced alginate
PAMP	Pathogen associated molecular pattern
MHC	Major Histocompatibility complex
TCR	T-cell Receptor
PRR	Pattern Recognition Receptor
TLR 4	Toll-like Receptor 4
APC	Antigen Presenting Cell
IL-	Interleukin-
IFN-γ	Interferon-gamma
CD-	Cluster of Differentiation
MSD	Mean Squared Displacement
ECM	Extracellular Matrix
GAG	Glucosaminoglycan
MMP	Matrix metalloprotease
M	β-D-mannuronic acid
G	α-L-guluronic acid
RGD	Arg-Gly-Asp (Arginylglycylaspartic acid)
CLSM	Confocal laser scanning microscopy
CRM	Confocal Reflectance microscopy
SHG	Second harmonic generation
UPLVG alginate	Ultra-Pure Low Viscosity high G-content alginate
UPMVG alginate	Ultra-Pure Medium Viscosity high G-content alginate
FBS	Fetal bovine serum
GFP	Green fluorescent protein
DIC	Differential interference contrast
Th1,2	Helper T-cell subset 1,2
NK	Natural killer
TNF-α	Tumor necrosis factor-α

1 Background

Inflammation is one of the main immune responses generated by the innate immune system after tissue damage or pathogen infection (1). Dendritic cells (DCs) are a part of the innate immune system and they can recognize pathogen associated molecular patterns (PAMPs) via their Toll-like receptors (TLRs) (2). The stimulation of DCs with endotoxins derived from pathogens can initiate a cascade of inflammatory mediators such as pro-inflammatory cytokines and chemoattractants in order to guide the migration of T-cells within the inflamed tissue (3, 4). DCs are antigen presenting cells (APCs) that are capable to present via their major histocompatibility complex (MHC) receptors a cognate antigen to T-cells recognized by the expressed T-cell receptor (TCR) in order to initiate an adaptive immune response (5). The migration of T-cells to the site of inflammation and the factors that dictate their motility are determinant for the tissue immunosurveillance in the terms of adaptive cellular immunity (3). Recent advances in the fabrication of *in vitro* platforms have facilitated the study of immune system interactions in a controlled microenvironment and have offered new insights to the development of adaptive immunotherapies (6). Three-dimensional (3D) cell culture has conferred to a more realistic approach in order to simulate T-cell responses of the *in vivo* microenvironment (7). T-cell motility in engineered 3D scaffolds can resemble characteristics that are found in the extracellular matrix (ECM) (7). The evaluation of T-cell migration in engineered 3D multi-compartmental scaffolds under the presence of stimulated DCs can offer a better understanding for the spatial-temporal events that govern the adaptive immune response in an inflammatory microenvironment.

2 Aims of the study

The primary aim of the current project was to engineer multi-compartmental hydrogels in order to investigate T-cell migration in 3D under inflammatory conditions and secondly, to compare T-cell motility in different biomaterial interfaces. Proper adjustment of the multi-compartmental system was necessary, in order to avoid phase transitions that would influence collagen fiber integrity and affect the migration of T-cells. The migration of T-cells in the multi-compartmental hydrogels was characterized by live cell imaging using confocal laser scanning microscopy and further complex data analysis to quantitate motility parameters and migratory behavior. The migration of T-cells was initially expected in collagen and Matrigel hydrogels, based on previous publications. The initial question was if the secretion of pro-inflammatory mediators in the system would enhance migration towards the gradient. Successful, establishment of the 3D platform would offer new insights to study T-cell responses during inflammatory conditions, by incorporation of various immunogenic factors in the system. T-cell migration was firstly demonstrated in the collagen system. Secondly, T-cell migration was studied in Matrigel and alginates, both native and chemically modified and the T-cell behavior was compared in the different interfaces.

3 Introduction

3.1 Innate immunity

Innate immunity is the first immune system barrier encountered by pathogens and plays an important role in the immune surveillance of tissues in health and disease. One of the major functions of the innate immune system relies on the inflammatory response. Inflammation is a complex biological response that can be initiated as an outcome of pathogen infection or tissue damage. Inflammation triggers the recruitment of leukocytes and plasma proteins at the affected tissue site (1). The initiation of inflammatory responses derived from pathogen invasion is relied to pathogen associated molecular patterns (PAMPs) recognition by pattern recognition receptors (PRRs). PRRs are expressed by many cell types including hematopoietic and non-hematopoietic cells. Various classes of PRRs have discovered including nucleotide oligomerization domain (NOD)-like receptors, retinoic acid inducible gene I (RIG-I) receptors and Toll-like receptors (TLRs) (8).

3.1.1 Toll-like receptor 4 (TLR4)

TLRs were initially correlated with the innate immune defense at Jule's Hoffman laboratory in Strasbourg where TLR4 deficient *Drosophila melanogaster* were susceptible to fungal infection (9). Currently, 13 different TLRs have been identified and among them only TLR1-9 are conserved in humans and mice. TLR1,-2,-4,-5 and -6 are located on the plasma membrane and TLR3, -7, -8, -9 are located subcellularly (10). TLR4 is located on the surface of phagocytic cell subsets including neutrophils, macrophages and DCs and is mainly responsible for the recognition of PAMPs, including the lipopolysaccharide (LPS) derived from Gram-negative bacteria, envelope proteins from syncytial viruses, glycoinositol phospholipids from trypanosomes and heat shock proteins 60 and 70 (10). Furthermore, recent studies have suggested that TLR4 recognizes additional endogenous patterns, such as myeloid-related proteins derived from phagocytes under septic circumstances (11). Various accessory molecules including, myeloid differentiation factor (MD-2), lipopolysaccharide binding protein (LPB) and CD14 are required for the efficient LPS binding and activation of the TLR4. CD14 can be found either in a plasma soluble form or expressed on the surface of different phagocyte subsets and is responsible for the transfer of LPS to the MD-2 that mediates the activation binding complex with the TLR4 on the plasma membrane (12). However an activation model of TLR4 in an LBP-CD14 independent manner has been suggested, including serum albumin as the main endotoxin transporter to MD-2 (13). Upon LPS binding, homodimerization of the TLR4 ectodomains is occurred that leads to conformational changes at the cytoplasmic Toll/Interleukin-1 receptor (TIR) domains that induce dimerization. The dimerized TIR domains provide an activation pattern that is recognized by other adaptor molecules such as myeloid differentiation primary response protein (MyD88) and TIR domain containing-adapter protein (TIRAP) that create a protein complex together with other serine/threonine kinases and initiate the intracellular signaling cascade of the TLR4 (10). The main terminal point of TLR4 signaling cascade includes the translocation of the nuclear factor-kappa-B (NF-κB) to the nucleus and the upregulation of pro-inflammatory genes transcription including the interleukins IL-1β, IL-6, IL-8 and tumor necrosis factor-α (TNF-α) (10). Activation of a parallel signaling pathway that is executed at the endosomes, after internalization of

activated TLR4, begins with the assembly of TIR-domain-containing adapter-inducing interferon-β (TRIF) and TRIF-related adaptor molecule (TRAM) that is followed by the binding of interferon regulatory factor (IRF3) and leads to the induction of type-1 interferons (14). The internalization of the activated TLR4 and trafficking via endosomes has been shown to be CD14 dependent after complex formation with the 1-phosphatidylinositol 4,5-biphosphate phosphodiesterase-γ2 (PLCγ2) and the tyrosine protein kinase Syk (15). The kinetics of pro-inflammatory cytokines and chemokines production followed by TLR4 stimulation with LPS *in vitro* have been investigated on dendritic cells. In general terms at the mRNA level the immune response reaches a maximum pick 3-4 hours after exposure to LPS while at the protein synthesis level, the secretion is increased to the timepoint of 12 hours where the concentration in the medium has reached the maximum level (16).

3.2 T-cells

T-cells are a central part of the adaptive immunity and they play an important role in the host defense against pathogens and tumors. T-cell progenitors are matured in thymus where they undergo somatic gene recombination which results to the expression of the expression of a unique T-cell receptor (TCR) (17). During maturation in the thymus T-cell undergo positive and negative selection. Positive selection process is mediated by the detection of antigens presented on the major histocompatibility complex class 1 (MHC I) or class 2 (MHC II) by the TCR and the differentiation to $CD8^+$ or $CD4^+$ is respectively determined. T-cell that their TCR recognize an autoantigen are eliminated by negative selection. Positively selected T-cell that are not auto reactive exit the thymus and circulate in the blood and lymphatics as naïve (18). Naïve T-cells get activated after the recognition of a cognate antigen by their TCR which is accompanied by a costimulatory signal and contribute to adaptive pathogen immunity as effector cells. $CD8^+$ are categorized as cytotoxic T-cells and $CD4^+$ are characterized as helper T-cell subsets (5). After pathogen elimination the 95% of the effector T-cells undergo apoptosis while the rest are differentiated to specialized memory T-cells (19). The phenotypes that a T-cell can differentiate are shown in Figure 3.1.

3.3 Dendritic cells and their role as APCs

DCs are classified as professional APCs since they are able to cross present antigens by utilizing MHC I and MHC II receptors and prime $CD8^+$ or $CD4^+$ T-cell responses (5). DCs continuously sample proteins and present peptides on their surface. Upon recognition of PAMPs or danger signals released from damaged cells and they migrate to lymphoid organs where they can in turn initiate adaptive immune responses (20). Immunogenic DCs are defined by high MHC class II expression and the upregulation of costimulatory molecules such as CD80, CD86 and CD40 (8). The maturation state of dendritic cells has an important effect on their function as APCs and in the control of T-cell fate. In a steady immature state DCs remain tolerogenic and induce T-cell apoptosis and anergy. Under inflammatory conditions DCs retain their APC potential and guide the differentiation of antigen specific naïve T-cells to various effector T-cell phenotypes. Hence, in addition to the activation of DCs via their TLRs, paracrine inflammatory signals may regulate their maturation state and their role in the regulation of the adaptive immunity (21).

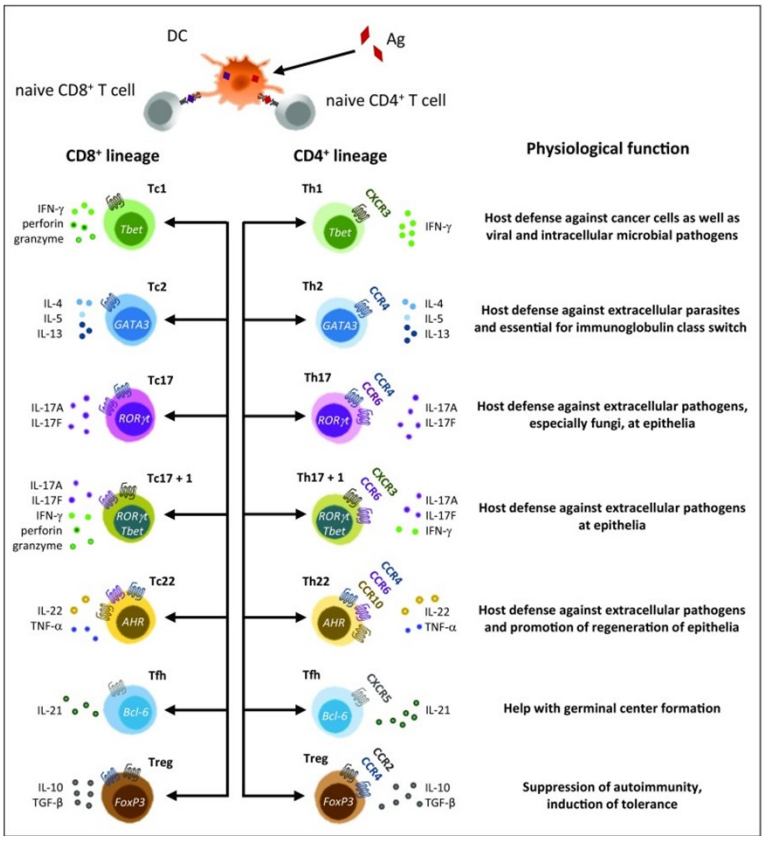

Figure 3.1: Effector T-cell phenotypes in respect to the chemokine receptor expression and to the effector cytokine secretion. Differentiation label transcription factors are also denoted. Figure adapted from (3).

3.4 Formation of the T-cell differentiation niche

During recent decades T-cell differentiation was believed to take place in secondary lymphoid organs (SLOs) such as the lymph nodes and the spleen. However under sustained inflammatory conditions such as those in chronic inflammation, tertiary lymphoid organ (TLOs) structures have been observed to form within the inflamed peripheral tissue site, providing local source of adaptive immunity (22). In addition it has been suggested that certain DC subsets can remain positioned in the inflamed tissue and locally drive T-cell responses (23). During inflammation in the skin macrophages and DCs undergo colocalization, forming clusters that function as gradient reservoirs for the attraction of effector T-cells in order to proliferate and produce cytokines (24). It has been recently supported that more than four different cell types are required for the formation of the T-cell differentiation microenvironment. This microenvironment can be constituted of stromal cells, granulocytes, natural killer (NK) and B-cells in addition to the APCs present (25). After the formation of the immunological synapse that includes the binding of the TCR with an MHC molecule on the surface of an APC presenting a cognate antigen, different effector cytokines that regulate T-cell polarization are secreted (26). IFN-γ secreted by T-cells has a co-stimulatory effect on DC maturation and higher production of IL-12 and IL-1β (27). IL-12 has an important role in inflammation and the T-cell responses by providing proliferation and survival signals (28). In some cases, non-cognate interactions between

costimulatory molecules such as the CD40/CD40L may contribute to the secretion of IL-12 (29). It has been clarified that the main factor that modulates the differentiation of T-cells to certain effector subsets is the cytokine milieu at the site where the pathogen or tissue damage has been encountered (3). Activated T-cells have been shown to obtain a "swarming" behavior at locations where APCs are present and initial antigen recognition has been encountered. This is a process that probably resembles a T-cell differentiation niche microenvironment where different T-cells subsets produce cytokine gradients that modulate the fate of effector T-cells and proliferation (30). In general terms, T-cells differentiation is governed by complex events that include the participation of multiple cells types, that orchestrate certain cytokine gradients. However, the inflammatory response at the level of PRRs could be the initial trigger that would determine the adaptive cell immunity fate to a certain pathogen or tumor.

3.4.1 Effects of TLR4 proinflammatory cytokines on T-cells

The pro-inflammatory cytokine IL-1β plays an important role in adaptive immune responses by promoting T-cell priming and differentiation while it has been shown assist the functions of $CD4^+$ T-cells (31). In addition, IL-1β can induce its own expression by DCs and further the expression of TNF-α, IL-6 and IL-8 (32). TNF-α has a co-stimulatory effect on IL-2 dependent IFN-γ production and promotes T-cell survival by antiapoptotic signals (33, 34). Pro-inflammatory cytokines produced after TLR4 activation such as IL-6 and IL-8 have shown to induce $CD4^+$ T-cell proliferation (35). IL-10 which is another cytokine produced after TLR4 activation can act as a negative regulator to the production of the rest proinflammatory cytokines and have a downregulation impact alone on T-cell responses (36).

3.5 T-cell migration

3.5.1 T-cell motility mechanisms

Cell locomotion is mediated by the polymerization and the depolymerization of the actin cytoskeleton at the leading edge of the cell and traction of the rear by the myosin-II that is bundled with the actin cytoskeleton. Thus, generating a propulsive force that enables the motility of the cell. At the leading edge the protrusions formed dependent on the bundling actin, can denote different modes of motility that are adopted in each microenvironment in order to promote migration to an exact location. In 2D the, leading edge protrusions are mentioned as pseudopodia that can be further distinguished regarding their functionality. In contrast to 2D motility where cell migration is actuated on a surface, in 3D cells may retain further morphological features that can be accompanied by functional properties (37). The formation of lamellipodia is occurred both in 2D and 3D from which are correlated with heavily bundled actin protrusions are mostly relevant to adhesion sites (38, 39). Filopodia in 2D and 3D can act alone or can be formed within lamellipodia, or blebs in order to sense the microenvironment (40). Lobopodia have been characterized as extended cylindrical protrusion resulted from intracellular pressure, similar to blebs. Invadopodia and podosomes have been discriminated as proteolytic protrusions associated with matrix invasion (41-43). Cell migration in 3D is distinguished in mesenchymal migration where integrins and matrix

degradation are involved and amoeboid migration that is independent to focal adhesions and proteolysis (44). The morphology and the molecular profile of the leading edge such as actin bundling and the colocalization of functional modules is coupled to those functions.

The motility characteristics of T-lymphocytes have shown comparable features to those described in the *Dictyostelium discoideum* amoeba. The morphology of T-lymphocyte is characterized by actin-reach leading edge and a highly contractile region that is mentioned as the uropod (45). The amoeboid motility behavior is ensued by dynamical leading edge ruffling, central region traction and the retraction of the adhesive uropod (46). The leading edge of T-cells is characterized by ruffling protrusions rich in actin and at some cases the formation of heavily bundled actin-rich protrusions that denote integrin adhesion(45). T-cell motility is generally characterized by fluctuations in velocity, with periods of high velocity remarked by increased pseudopod extension and dynamic reformation and pausing periods highlighted by a round shape (47). T-cells in contrast to other white blood cell types have shown to perform both mesenchymal and amoeboid modes of migration (44, 48).

In vivo T-cells adopt an average speed of 0.16-0.25 μm/s (10-15 μm/min) in the paracortex of the lymph node. The speed is regulated by integrins, chemokines secreted by DCs and intercellular adhesion molecules (ICAMs) (49). Amoeboid in lymph nodes migration has been characterized of lower values in speed, deviating around 0.06-0.11 μm/s (4-7 μm/min) (50). T-cells acquire average speed values of around 0.08 μm/s (5 μm/min), in the inflamed skin interstitial matrix, mainly composed of fibrillar collagen (51).

In vitro setups utilizing mainly collagen as a 3D matrix, have shown a huge variability in T-cell migration with values varying from 0.03-0.3 μm/s (2-18 μm/min) (52). However, due to variation in collagen concentration between set-ups, it would be hard to accommodate to a standard condition.

3.5.2 T-cell motility patterns

T-cells perform *in vivo* various motility patterns and search strategies that can be relevant to their activation and differentiation level (53). Mean squared displacement (MSD) provides a mathematical representation of the average displacement a cell or a particle undergoes over time. The definition of the MSD in 3D can been expressed as follows:

$$MSD(t_n) = \frac{1}{N-n}\left(\sum_{i=1}^{N-n}(x_{i+n}-x_i)^2 + (y_{i+n}-y_i)^2 + (z_{i+n}-z_i)^2\right) \quad (1)$$

Where x, y, z are the spatial coordinates, N is the total number of timepoints and $t_n = n \times \Delta t$ is the time delay between the analyzed coordinates.

By obtaining the graph of the MSD vs. t_n and one can estimate the profile of the motion. More specifically the MSD is proportional to time to an exponent α:

$$MSD \propto t^{\alpha} \quad (2)$$

The exponent α exponent can be calculated by fitting log(MSD) vs. log(t) and modeling the MSD in a power law:

$$\log(MSD) = a \times \log(t) + \log(\Gamma) \quad (3)$$

Thus, it has been suggested that for a random unconstrained diffusive behavior α=1. For α>1 the behavior is characterized as superdiffusive and for α<1 as subdiffusive (Figure 3.2). In the aspects of T-cell tracking and analysis of each individual cell's trajectory, the α exponent has been proposed to reveal information regarding the search strategies performed and the migration behavior. Phenomena such as directed migration may be characterized by taking into account the exponential characteristic of the MSD curves (53, 54).

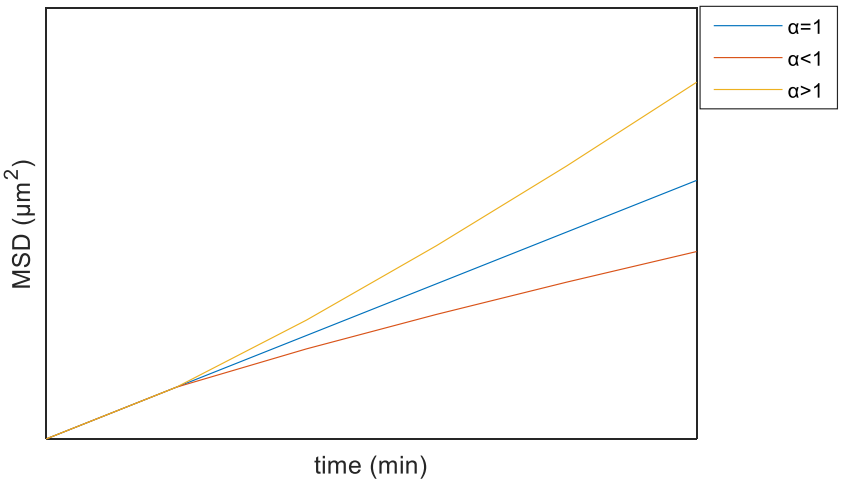

Figure 3.2: Example plot of the MSD vs. time. Different values of the α exponent contribute to a certain MSD curve shape. For α=1 a diffusive profile is highlighted. Values of α<1 correspond to a subdiffusive profile and α>1 indicates a superdiffusive profile.

Diffusive and subdiffusive random walks (Brownian type) represent a motion characterized by non-specific directionality and limited speed fluctuations. Microscale mechanisms involved in superdiffusive motility patterns include speed fluctuations or trajectories of finite speed with short random turning directions during displacement. An example of superdiffusive walk is the Lévy walk which is a mix of long trajectories and short random walks between the covered distances. Speed fluctuations and turning behavior are adapted to the microenvironment in order to satisfy the search criteria of keeping perception while speeding up to cover large distances and of the balance between local search and spreading to distant areas. T-cells can sometimes perform highly directional and straight ballistic movements where the α exponent profile is reflected by speed fluctuations. The T-cell search behaviors have been categorized as explorative and exploitative. Explorative behavior is underlined by a less informed movement based on the environment itself that could be relevant to cell-microenvironment interactions (haptokinesis, chemokinesis). From the other hand exploitative behavior is phenomenon that is attributed to given information and navigation guidance (haptotaxis, chemotaxis) (53). In terms of taxis in the 3D microenvironments the contribution of its mechanical properties can tailor the migration in between

locations of varied stiffness (durotaxis) (55). However, there is a trade-off in between exploitation and exploration that has been met in T-cell search behavior. In spatial cues during exploration superdiffussive behavior may be expected, whereas subdiffussive exploitative search behavior can be expected under the abundance of information cues. On the other hand, superdiffusive walks can be coupled to taxis for the displacement to a distant site and subdiffussive random walks to the presence of restrictive barriers (53). More advanced search theories have been formulated in order to better deal with the trade-off between exploration and exploitation, including the intermittent search theory where overall walks can be segmented in different phases (56).

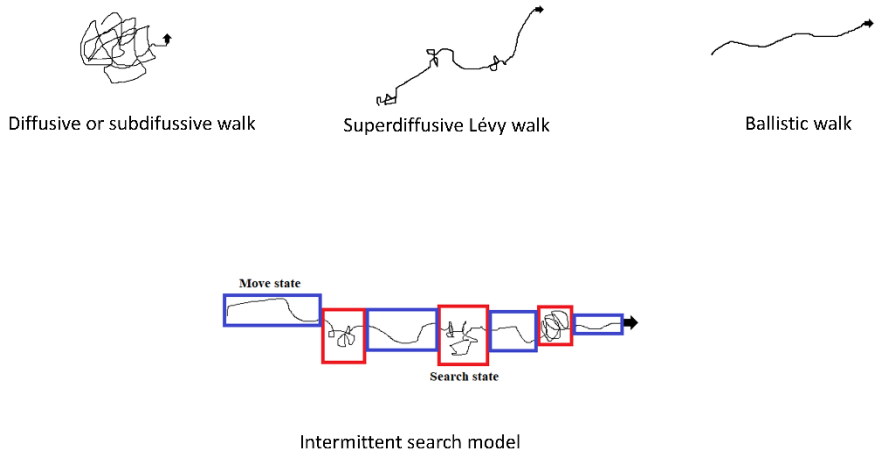

Figure 3.3 : Representation of possible motility patterns T-cells can undergo.

During inflammation T-cell motility patterns have been associated with supperdiffusive Lévy walks while such mechanism has been assumed to govern a more optimized search strategy for T-cells in order to encounter rare antigens presented by DCs (57). On the other hand, under inflammatory conditions in different tissues the interstitial T-cell motility has been associated by subdiffusive random walks and amoeboid migration, probably to highly localized cues provided by the APCs and tissue resident cells (58). Furthermore, intravital imaging of labeled effector T-cell subtypes has shown distinct motility patterns coupled to the phenotype. Th1 cells intrinsically performed subdiffussive highly localized walks around APCs while Th2 cells performed superdiffusive walks around the inflamed location (59).

T-cells can alter between different states of motion or result to transient migration trajectories due to cues in the microenvironment. Efforts have been made in order to set a rolling window within time delays, speed fluctuations and cutoffs in the exponential profile in order to further define the migratory behavior of T-cells or relevant lymphocyte subsets (54, 59). Although, no standards have been established.

3.5.3 Chemotactic cues

T-cell migration is mainly tuned by the expression of chemokine receptors which confer to the optimized migration in the lymphoid organs, recruitment to the inflamed tissue and recirculation to the lymphatics (60). Chemokine receptors belong to a superfamily of G protein-coupled receptors (GPCRs) which is constituted of 18 genes, divided in the CCR, XCR and CXCR subfamilies (60).Combinations of chemokine receptors expressed on the surface $CD4^+$ T-cell effector subsets are characteristic for each effector phenotype and have been defined as separation markers (3). Chemokine receptor ligands secreted by stromal cells and APCs provide chemotactic cues that navigate T-cells in the lymphoid organs in order to detect antigens and get activated. A differential expression of chemokine receptor ligands by stromal cells during an inflammatory response is occurred in contrast to the physiological steady state amounts (61). In addition, alternative mechanisms of self-generating chemotactic gradients have been proposed including the degradation of locally secreted chemoattractants (62).

3.5.4 Haptotactic cues

Different receptors located on the surface of T-cell contribute to motility by regulation of the actin cytoskeleton. Integrins are adhesion receptors playing an important role in the interaction with the ECM and with other cells. Integrins are expressed in α and β subunits that colocalize when activated and create adhesive modules called focal adhesions. The expression of the different α and β subunits varies between T-cell phenotype and is dependent mainly on subset and the tissue of origin (63). The intracellular domain of the β subunit is the main component that interacts with signaling proteins and mediates regulation of the actin cytoskeleton (45). in addition to integrins T-cells obtain receptors that are glucan associated and mediate migration by binding to GAGs and by rolling. Examples of those receptors are the CD44 (Hyaluronan receptor), CD43 and the L-selectins (64). L-selectins and other mucin-like molecules located on the T-cell surface may mediate low affinity interactions with the GAGs in the ECM (65, 66). L-selectin regulates Rho-GTPase activity and therefore plays an important role to the regulation of the actin cytoskeleton polymerization (67, 68).

3.5.5 Physical factors

T-cells are thought to use the surrounding matrix as a physical scaffold to undergo migration by elongation of actin reach protrusions that mediate pushing and subsequent squeezing, generating propulsive forces that mediate a non-adhesive mode of locomotion(45, 69). Neutrophils have shown to transmigrate using a force mediated penetration of 3D matrix or cellular barriers while this force is believed can be enhanced with integrin mediated adhesion. In a similar manner T-cell may benefit their intrinsic locomotion machinery that is assumed as independent of any external stimulation and constantly "turned-on" (69, 70). The stiffness of the extracellular environment has shown to play an important role in cell migration in terms of durotaxis and mechanosensing (55, 69). Finally, in vitro systems have shown that animal cell responses have been shown to be accompanied by the mechanical properties of hydrogels (71).

3.6 The extracellular matrix (ECM) and its role in inflammation

The extracellular matrix (ECM) is the fundamental matter that constitutes the extracellular space. The ECM is consisted of various soluble and in-soluble structural components secreted by the cells comprising the local microenvironment in every tissue. The main types of ECM include basement membranes which are thin layers of highly crosslinked glycoproteins and interstitial matrix that is characterized by a loose fibrillar structure (72). Composite types of ECM are found in the lymphoid tissue providing the sufficient conditions for the immune system function (73).The proteoglycan and the glucosaminoglycans (GAGs) found in the ECM provide multiple binding sites to integrin and non-integrin receptors and reservoirs for the deposition of growth factors and chemoattractants. The ECM provides cleavable sites by (matrix metaloproteases) MMPs that allow its continuous rearrangement (74). During inflammation, the ECM remodeling by immune cells is upregulated together with the secretion and entrapment of chemoattractants. Leukocytes remodel the ECM in order to reside to the inflamed site. Degradation of the ECM components can lead to the formation of immunogenic peptide and glycan fragments that can augment inflammation and act as chemokines or activate certain TLRs such as TLR4 (70). Lastly, the alignment of the ECM components and its stiffness have been shown to alter under inflammatory conditions leading to either a restrictive or a beneficial outcome to the motility leukocytes (69).

3.6.1 Effects of the activated TLR4 pro-inflammatory cytokines on ECM remodeling by T-cells

An additional pleiotropic effect of pro-inflammatory cytokines includes the regulation of the extracellular matrix (ECM) remodeling in the inflamed tissue in order to facilitate immune cell infiltration. TNF-α and IL-8 are responsible for induction of matrix metalloproteases -9 and -2 (MMP-9,MMP-2) release by T-cells and confer to migration(75, 76). From the other hand, interferons such as IFN-β and IFN-γ have shown to downregulate MMPs secretion by T-cells (77). Finally IL-1β and IL-6 have been found to increase MMP-3 secretion in different cell types than T-cells (78, 79). However MMP-3 has been reported to be expressed by other lymphocyte subsets and the secretion by T-cells remains an undetermined, while poor evidence are available regarding T-cell MMP profiling (77).

3.7 Biomaterials

Biomaterials are synthetic or naturally derived compounds with properties that can support biological function. Biomaterials based on natural or synthetic polymeric systems with a defined bioactivity have drawn the attention of tissue engineering, regenerative medicine and cell biology. The development and the establishment of 3D scaffolds for tissue and cell culture has provided a more advanced approach in order to study cell interactions since they can provide 3D bioinstructive interfaces resembling the bioactive properties of the ECM. The development of 3D co-culture systems in order to investigate immune system models has been recently elaborated (80). 3D co-culture systems offer a 3D spatial-temporal observation of immune system activity including cell migration and polarization according to a stimulus (81).

3.7.1 Collagen

Collagen is one of the major extracellular matrix (ECM) components and constitutes up the 25% of the total protein mass in mammals (82). Collagen is found into different types which can be distinguished according to morphological and structural properties as fibrillar, fibril-associated, transmembrane and proteoglycan core protein. The collagen molecule has a rope-like structure that is formed by the alignment of three collagen polypeptide α-chains. Fibrillar collagen type-I is the most abundant collagen type found in mammals and it consists around 90% of the total collagen proteins (82).

Fibrillar collagen type-I, has been used as a scaffold in order to investigate lymphocyte motility and migration in 3D *in vitro* models (54, 83). Acid soluble collagen type-I retains the non-collagenous N- and C- terminal peptide domains that allows crosslinking of lysine residues by neutralizing the pH, which results to the formation of a fibrillar network. From the other hand pepsin-extracted collagen does not include the telopeptide sequences, therefore lacks fibrillar network architecture (84).

Different parameters determine the collagen hydrogels functionality in respect to cell migration and motility. Cell motility has been shown to have a higher correlation to the collagen fibers alignment and directionality as well as to the concentration. At low concentrations, collagen fiber nucleation sites are of a lower amount, that results in stiffer fibrillar network formation, with thick fibers entangled. At high concentrations of collagen matrices adopt nematic-like structures and show increased stiffness. Intermediate concentrations of collagen result in softer polymer matrix with sorter fiber length resulting to a decreased cell speed compared to lower or higher concentrations (85). Cell speed and directionality are highly connected to the thickness and direction of the collagen fibers, while collagen fiber orientation and it has been stated that there is a small correlation with the pore size (86).

Temperature for gelation pH and ionic strength have been shown as well to influence the alignment of collagen fibers. However, unstable pH values and ionic strength can influence cellular viability (86). Gelation of collagen at different temperatures revealed structural differences in its network architecture. At 37 ℃ collagen forms 3D culture scaffolds were cells are able to retain their viability and motility. Collagen fibers promote the formation of focal adhesions to the cells by exposing integrin binding sites (86).

Type-I fibrillar collagen has been used for many decades for lymphocyte migration studies and remains a reference biomaterial up to date, due to its biological origin that offers a good scaffold for the establishment of 3D platforms in order to investigate interstitial T-cell migration (44, 59).

3.7.2 Matrigel

Matrigel is a viscous protein mixture extracted from the secreted ECM of Engelbreth-Holm-Swarm (EHS) sarcoma cells. Matrigel contains large quantities of the components found in the native basement membranes, including collagen IV, laminin, perlecan, and various other enzymes and growth factors. It has been extensively used as 3D cell culture scaffold, while the cellular response in terms of proliferation, differentiation and growth is dependent on the cell type (87). Matrigel is liquid at the temperature of 4-10 ℃ and gels immediately at 37 ℃. The

regenerative properties of Matrigel as a stem cell seeded transplant, have been assessed for the treatment of spinal cord injury in rats (88). From the other hand, the use of Matrigel in human tissue engineering applications has been controversial due to its rodent species origin, but instead, species specific alternatives have been developed (89). Still, the batch-to-batch variability of such biomaterials may be reflected on the developmental outcomes of the engineered system (90).

For instance, Matrigel has been employed as biomaterial interface in order to study lymphocyte infiltration in 3D ex vivo systems. Organotypic co-culture of cancer organoids and cancer associated fibroblasts in Matrigel has been recently tested as a 3D T-lymphocyte infiltration assay. In the presence of cancer organoids in the Matrigel, a proportion of buffy coat isolated T-lymphocytes from the overlaid media were able to infiltrate the Matrigel and migrate towards the tumor (91). In a similar 3D *in vitro* co-culture model NK cell infiltration was evaluated in a combination of Matrigel and Collagen I. Stimulated NK cells were able to migrate towards the cancer organoids whereas non-stimulated NK cells remained stationary (92). Taking under consideration previously published experimental data Matrigel seems to be a good biomaterial to study basement membrane infiltration.

3.7.3 Alginate

Alginate is a linear unbranched polysaccharide that is naturally found in brown algae and is produced by some bacterial strains(93-95). Alginate is composed of β-D-mannuronic acid (M) and α-L-guluronic acid (G) monomers that are linked with 1→4 -O glycosidic linkage. The alginate chain sequence is variable dependent on the source and is composed of homopolymeric patterns (M-blocks and G-blocks) and alternating patterns (MG-blocks) (96). The fractal composition of the alginate chain is expressed in frequencies of monads (F_M , F_G), dyads (F_{GG},F_{GM}, F_{MG}, F_{MM}) and triads which are defined as M-centered (F_{MMM}, $F_{MMG,}$ F_{GMM}, F_{GMG}) or G-centered (F_{GGG}, F_{GGM}, F_{MGM}, F_{MGG}) (97). In the presence of G-blocks alginate chains can be physically cross-linked with divalent cations such as Ca^{2+}, Sr^{2+} and Ba^{2+} contributing to the formation of porous gels. The average length of G-blocks is denoted as $N_{G>1}$. Cross-links by Ca^{2+} are formed by divalent ion binding between diaxial (GG) or equatorial-axial (MG) linked residues resulting to interchain junction described by the "egg-box" model (97). The mechanical properties and the porosity of the alginate gels under physiological conditions are dependent on the chemical composition and concentration of the alginate while can be further modulated by the divalent ion concentration, type and valency as well as the presence of Na^+ counterions (96-98).

Alginate has been widely used as a biomaterial for 3D cell- tissue culture and implantation purposes. In particular alginate has been widely used for tissue engineering applications since it is non-toxic to the cells and forms gels under physiological conditions, with tunable mechanical properties (99). The gelation methods used for the encapsulation of cells into alginate can be categorized as internal or external. External gelation of the alginate occurs when alginate is added in a gelling solution where a dissolved divalent crosslinker is contained. The external gelation mechanism allows for the rapid microencapsulation of living cells and it provides a viable scaffold where nutrients and metabolites can freely diffuse along the capsules (100, 101). Internal gelation can be achieved by mixing the alginate with calcium carbonate ($CaCO_3$), which after the addition of GDL and pH

reduction, is dissolved and Ca^{++} are internally released leading to the physical crosslinking of the alginate chains (102).

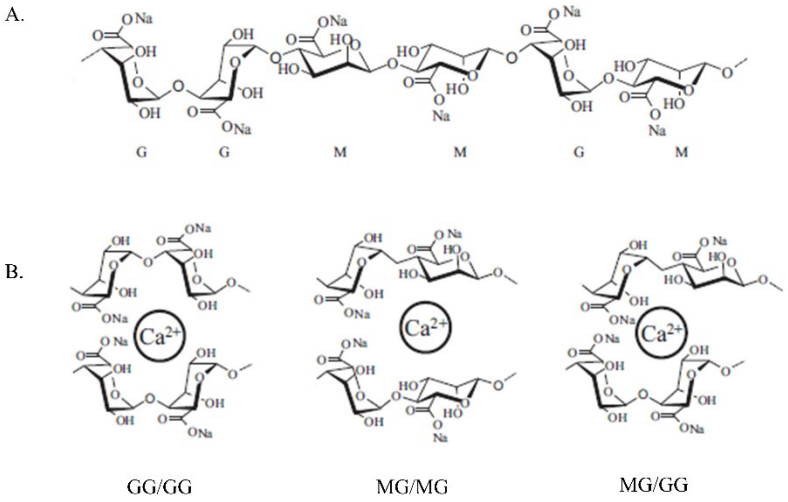

Figure 3.4: Illustration of alginate structures. (A.) Alginate chain block illustration G-block (left), M-block (middle), GM-block (right). Chair conformation denotes the diaxial (GG), axial-equatorial (GM), diequatorial (MM) and equatorial-axial (MG) geometries of O-glycosidic linkages (B.) Different alginate block crosslinking with Ca^{++}. Figures adapted and modified from (97).

Unmodified alginate has been considered of low bioactivity in terms of immunogenic profile and interaction with cells (99). Studies have shown that high M alginate can augment pro-inflammatory responses on macrophages (103). In addition to that oligo guluronate has shown to induce TLR4 mediated responses (104). On the other hand, alginate has mediated free-radical scavenging properties and has shown an effect on the differentiation status of $CD8^+$ T-cells correlated to the expression of anti-oxidative genes (105).

Alginate can be further functionalized with bio-active molecules in order to create bio-instructive interfaces that resemble moieties found in the natural ECM (99, 106). Chemical modification of the alginate chain using periodate oxidation and reductive amination grafting of bio-active peptides including the -RGD- peptide sequence have shown to provide feasible integrin binding sites that can be found in the native ECM (106). Alginates have also been modified with the addition of sulfate chemical groups that resemble the chemical properties of the heparin which contributes to the sequestration of growth factors in the ECM (107). Partial oxidation of alginate results to reactive dialdehyde moieties which increase degradability and chain compaction (99). Partially oxidized alginate gels result to larger pore sizes and decreased stiffness contributing to the higher viability of different cell types (108, 109). The physical and chemical properties that enable reductive amination cross-linking with different bioactive compounds have posed partially oxidized alginate as a good candidate for the development of bio-inks in 3D bio-printing applications (109).

Alginate has been used as a scaffold for DC encapsulation and immunization of mice, where T-cells found to respond to a cognate antigen presented by the DCs

and recirculate to the lymph nodes of the mice (110). Recently, alginate methacrylate cross-linked with poly(ethylene glycol) methacrylate and enriched with Notch ligands cryogel, was injected to mice resulting to supportive scaffold for T-cell differentiation niche formation (111). T-cells that were co-cultured in alginate-chitosan scaffolds with prostate tumor cells migrated to the site of the cancer(112). Up to date, T-cell activity was studied on RGD-alginate scaffolds with varied stiffness. APCs were co-cultured with specific antigen T-cells and the activity of lymphocytes was reported. Interestingly, the authors reported activity, although reduced, in non-modified alginate. Increased motility and activation status of T-cells by APCs was coupled to stiffer interface (113).

3.8 Microscopy

Light microscopy is a classic method, consistently used over centuries in order to image the microworld. The development of high resolution technologies and methods has preserved microscopy as a gold standard for imaging in cell biology. The evolution of confocal microscopy and multi-photon excitation has offered new insights for the 3D observation of biological specimens and tissues. Intra-vital and *in vitro* live cell imaging have contributed to further understanding of biological functions and to the development of 3D *in vitro* platforms.

3.8.1 Confocal microscopy

In the ordinary epifluorescence microscopy a fluorescent dye is excited on a certain wavelength and the emitted optical signal is collected on another wavelength. The main disadvantage of the ordinary epifluorescence microscopy is that the out-of-focus emitted light interferes with the in-focus light that is collected in the focal plane of the acquired image. The working principle of confocal microscopy is based on the implementation of a pinhole that blocks the out-of-focus light which creates a background noise on the focal plane of the specimen. Confocal laser scanning microscopy (CLSM) is a high-resolution method that utilizes the capacity of a laser that emits in a certain wavelength with tunable power. The pinhole aperture is further collecting the in-focus light that is emitted by the sample after the excitation. Smaller pinhole size results to higher z-resolution but lower signal intensity compared to larger size. The laser wavelength is tunable and enables a multi-color excitation that allows the imaging of different dyes at the same sample. CLSM thus allows to the acquisition of different focal planes stacks on the z-axis that can be reconstructed to a 3D image, so called z-stack (114).

3.8.2 Confocal Reflectance Microscopy

Confocal reflectance microscopy is an optical imaging technique that is based on confocal microscopy, where the optical signal is generated by the intrinsic backscattering light reflected by biopolymers or tissues stained with probes that reflect light. Confocal reflectance microscopy has been used *in vitro* for the 3D visualization the ECM structural components and to study either statically or dynamically biopolymer networks such as collagen type-I (115).The incident light of the laser is reflected to the objective and the out-of-focus light is filtered out by the pinhole allowing to pass only signal from the focal plane of the specimen. Confocal reflectance microscopy is used extensively in the medical field of dermatology as a diagnostic tool for skin malignancies and skin inflammatory diseases (116). The flexibility of CRM for collagen type-I imaging relies on its label

free property and on the minimal adjustment that needs to be done on the confocal microscope.

3.8.3 Second Harmonic Generation (SHG) Microscopy

Second harmonic generation microscopy is a non-linear label free two-photon imaging technique and arises from non-symmetrically assembled polar molecules. Structural components within tissues such as collagen type-I and II, myosin and tubulin are capable to produce SHG which makes it suitable for *in situ* and *in vivo* studies. SHG provides intrinsic optical sectioning to point scanning microscopy, high in-depth penetration and reduces the out-of-focus photobleaching and phototoxicity (117). Limitations of the SHG microscopy include the restricted number of biological molecules that can be studied and hurdles when imaging highly scattering tissues. Detailed information dependent on the polarization of the molecules can be extracted only from superficial regions (118).

4 Materials and Methods

The overall system design of the multi-compartmental hydrogels proposed for this work is illustrated in figure 4.1. To generate pro-inflammatory conditions, it was decided to encapsulate DCs into alginate microstructures together with lipopolysaccharide (LPS) that would activate the TLR4 pathway and initiate the secretion of pro-inflammatory cytokines and chemoattractants. In turn, alginate microstructures with stimulated splenic DC line were embedded in a biomaterial interface mixed with $CD4^+$ T-cell hybridomas. Collagen type-I, Matrigel and chemically modified alginate were chosen to compose the compartment that T-cell were localized.

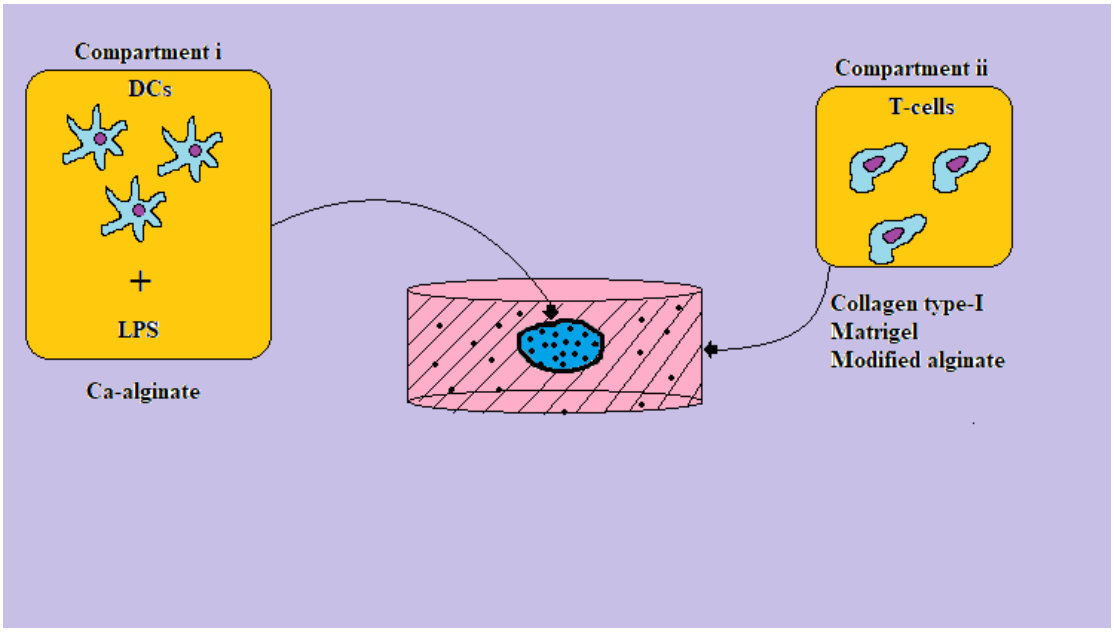

***Figure 4.1*: Schematic representation of the multi-compartmental hydrogel system.** Spenic DCs line (1940DC) were encapsulated in Ca-alginate microstructures and embedded into a biomaterial interface composed of either Collagen type-I, Matrigel or chemically modified alginate that contained T-cell hybridomas (MF2). To stimulate 1940DCs an amount of LPS was used during the encapsulation in order to activate the TLR4 pathway and lead to the secretion of pro-inflammatory mediators that can generate migration cues.

4.1 Polymers

In Table 1 the different alginates used during the study are described together with their molecular fractions, average molecular weight, chemical modification and degree of substitution. Sulfated alginate and POAred were synthesized and characterized as described in sections 4.2-4.4.

***Table 4.1*: Composition of the alginates used in the experimental work.** Supplier and product name,fractions of M and G in monads, dyads and triads (G-centered). average G-block length ($N_{G>1}$), weight average molecular weight (M_w) in kD, degree of substitution (DS).

Name	F_G	F_M	F_{GG}	F_{GM}	F_{MM}	F_{GGM}	F_{MGM}	F_{GGG}	$N_{G>1}$	M_w (kD)	Modification	Degree of substitution (DS)
FMC Biopolymer LF200S	0.677	0.323	0.567	0.110	0.213	0.041	0.082	0.526	14	298	-	-
Pronova ® UPLVG	0.682	0.318	0.572	0.111	0.207	0.040	0.067	0.532	16	237	-	-
Partially Degraded Pronova ® UPLVG	0.682	0.318	0.572	0.111	0.207	0.040	0.067	0.532	16	152	-	-
POAred	0.682	0.318	0.572	0.111	0.207	0.040	0.067	0.532	16	93	Periodate oxidation followed by reduction	8% degree of oxidation
UPLVG - RGD	0.682	0.318	0.572	0.111	0.207	0.040	0.067	0.532	16	97	GRGDSP peptide	5%
Sulfated Pronova ® UPMVG	0.664	0.336	0.545	0.119	0.218	0.046	0.088	0.499	13	163	Sulfation	80%

4.2 Sulfated alginate synthesis

Sulfation of the alginate was performed as previously described (119).Ultra-Pure Medium Viscosity High G-content alginate (UPMVG, Pronova, DuPont, USA) was dispersed in formamide (Merck, USA) to the concentration of 2.5% (w/v). Clorosulfonic acid (99%, Sigma-Aldrich, USA) was added to the amount of 3% (v/v) in suspension and the reaction mixture was placed in a waterbath at 60 ℃ with stirring for 2.5 h. After the reaction was completed the reaction mixture was transferred to centrifuge tubes and acetone (Merck, USA) was added to approximately double the reaction mixture volume. Tubes were centrifuged for at 4700 rpm for 7 min at 10 ℃. The supernatant was discarded and the alginate precipitate was transferred to MQ-water (MilliQ system, Millipore,). Alginate solution was neutralized to pH 7 by adding dropwise 1M NaOH solution. Alginate solution was dialyzed in 12-14 kD dialysis bags against MQ-water until the conductivity was less than 2 µS/cm. Alginates were finally freeze dried and stored in the freezer at -20 ℃. The degree of sulfation was determined by the PhD student Joachim Sebastian Kjesbu with ICP-MS analysis.

4.3 Periodate oxidation and reduction of alginate

Partial oxidation and reduction of the alginate was performed as previously described (106). Ultra-Pure Low Viscosity high G-content alginate (UPLVG, Pronova, DuPont, USA) was weighed out and placed in a desiccator overnight to dry out. The alginate was dissolved in MQ-water to the concentration of 8.89 mg/ml and 10% (v/v) to the final volume 1-propanol was added as a free radical scavenger. The solution was degassed with Nitrogen gas. A stock solution of 0.25 M sodium (meta) periodate ($NaIO_4$, Merck) was prepared and degassed with Nitrogen gas. The alginate solution was cooled down to 4 ℃ and the required amount of 0.25 M sodium periodate solution was added to achieve 8% oxidation of the alginate (0.08:1 molar ratio of periodate per alginate unit). The reaction mixture was left to react at 4 ℃ for 72 h. All handling was carried out in subdued light because of the light sensitivity of sodium periodate. The reaction mixture was dialyzed against 0.05 M NaCl MQ-water in 12-14 kD dialysis bags until the conductivity was less than 2 µS/cm. Alginates were finally freeze dried and stored in the freezer at -20 ℃.

Partially oxidized alginate was dissolved in MQ-water to the concentration of 6 mg/ml under magnetic stirring and methanol (MeOH) was added to the amount of 12% (v/v). Picoline borane (pic-BH3) was dissolved in methanol to the concentration of 0.25 M and the required amount to achieve reduction of the oxidized units was added (20:1 molar ratio of pic-BH3 per oxidized unit of alginate). The pH was adjusted to 5.8 and MQ-water was added until the concentration of partially oxidized alginate was 3 mg/ml. The sample was incubated for 72 h at room temperature (RT) on a shaker. The reaction mixture was dialyzed against one shift in 0.5 M NaCl and one shift in MQ-water, in 12-14 kD dialysis bags until the conductivity was less than 2 µS/cm. Alginates were finally freeze dried and stored in the freezer at -20 ℃.

4.4 Characterlization of the produced alginates

4.4.1 SEC-MALLS

For SEC-MALLS sulfated alginate and partially oxidized and reduced (POAred) samples were dissolved in MQ-water to a final concentration of 4 mg/ml and incubated under magnetic stirring overnight. The analysis was carried out at room temperature. The mobile phase was prepared with 0.15 M $NaNO_3$ and 0.01 M EDTA with the pH adjusted to 6. Samples were dissolved in the mobile phase to 1 mg/ml and filtered through 0,8 µm pore filter. Then, samples were injected to the system. The instrument was equipped with automated injection system and a TSK6000+5000 PWxL column (Toso Haas, Germany), WTC Dawn Heleos II light scattering detector (Wyatt, USA) and ViscoStar II viscosity detector (Wyatt, USA). The resulted data were processed with Astra software v.7 (Waytt, USA). The refractive index increment (dn/dc_μ) was set to 0.15 ml/g as previously reported (120). The SEC-MALLS data processing was carried out at the Department of Biotechnology and Food Science, NTNU, Trondheim by Ann-Sissel Teialeret Ulset.

4.5 Cell lines

4.5.1 1940DC

1940 MutuDC (1940DC) is an adherent cell line derived from $CD8\alpha^+$ DC tumors developed in transgenic CD11c:SV40LgT mice. 1940DC express the SV40LgT oncogene under the CD11c promoter together with an eGFP reporter. 1940DC lines have retained the antigen cross presentation capacity that is found in wild type splenic $CD8\alpha^+$ cDC subset. Additionally, 1940DC cell lines express similar TLR3, TLR4 and TLR9 subsets as found in wild type splenic $CD8\alpha^+$ cDCs and can respond to stimulation with their respective ligands PolyIC, LPS and CpG, accompanied by the expression of costimulatory cell surface antigens CD40, CD80 and CD86 (121).

4.5.2 MF2.2D9 T cell hybridoma

MF2.2D9 T-cell hybridoma (referred to simply as MF2) was a gift from professor K.Rock (University of Massachusetts Medical Center, Worcester, MA). The MF2 T cell hybridoma, has been naturally derived by immunization and further immortalization. The MF2 T-cell hybridomas have a $CD4^+$ phenotype and their TCR recognizes the $OVA_{265\text{-}280}$ peptide, presented by the $I\text{-}A^b$ (122).

4.6 Cell culture

Murine dendritic cell line 1940DC was cultured in Iscove Modified Dubelco Media (IMDM, Gibco™,USA) adjusted to 310 mOsm/kg with $NaHCO_3$ (Sigma-Aldrich, USA). IMDM stock supplemented with 8% Fetal Bovine Serum (FBS, Sigma-Aldrich, USA) heat deactivated at 56 ℃ for 30 minutes, 50 mM β-mercaptoethanol (Gibco™, USA), 10 mM 4-(2-hydroxyethyl)piperazine-1-ethansulfonic acid (HEPES, PanReach/AppliChem, USA) and 50 U/ml penicillin/streptomycin (Sigma-Aldrich, USA). 1940DC cell line was harvested by incubation in 5mM ethylenediaminetetraacetic acid (EDTA, Sigma-Aldrich, USA) based dissociation buffer (5mM EDTA in PBS) with pH adjusted to 7.2-7.4. Cells were maintained and used for the experiments until passage 50. 1940DC cell line was incubated in a 5% CO_2 incubator at 37 ℃.

MF2 T-cell hybridoma cell line was cultured in Roswell Park Memorial Institute 1640 media (RPMI-1640, Gibco™, USA) adjusted with $NaHCO_3$ (Sigma-Aldrich, USA) to 310 mOsm/kg. The stock RPMI-1640 media was supplemented with 10% FBS, heat deactivated at 56 ℃ for 30 minutes, 50μM β-mercaptoethanol (Gibco™, USA), 2 mM L-glutamine (Sigma-Aldrich, USA), 10 mM HEPES (PanReach/AppliChem, USA) and 50 U/ml penicillin/streptomycin (Sigma-Aldrich, USA). MF2 cell were split by 1:100 cells to media ratio every 2 days. MF2 cells were incubated in a 5% CO_2 incubator at 37 ℃.

4.7 Cell staining

MF2 cells were stained for imaging using CellTracker™ Red CMPTX dye (CTRed, ThermoFisher Scientific, USA). The vial content (50 μg) was brought to room temperature and dissolved in 72.9 μl sterile dimethyl sulfoxide (DMSO, ThermoFisher Scientific, USA) to prepare a stock 1 mM solution. The stock solution was stored in the freezer. To prepare the staining solution 5 μl of dye stock solution was dissolved in 1 ml fully supplemented RPMI-1640 without FBS.

MF2 cells were collected from the culture flask and counted using an automated MOXI Z Mini Cell Counter kit (ORFLO®, USA). A suspension, which contained the desired amount of cells, was transferred to 15 ml falcon tubes and centrifuged at 1000 rpm for 5 min. The supernatant was discarded and the cell pellet was resuspended in 1ml of staining solution and incubated at 37 ° C in a 5 % CO_2 incubator for 45 minutes. After the incubation, cells were centrifuged at 1000 rpm for 5 minutes and the staining solution supernatant was discarded and the cell pellet was resuspended in 10 ml fully supplemented RPMI-1640 without FBS. An additional centrifugation was followed at 1000 rpm for 5 minutes, in order to wash the cells and remove any excess of staining solution. The supernatant was discarded and the MF2 cells were resuspended in fresh fully supplemented RPMI-1640 (10% FBS).

4.8 1940DC stimulation

Non-modified, Ultra-Pure Low Viscosity high G content alginate (UPLVG, Pronova, DuPont, USA) was dissolved under magnetic stirring in MQ-water supplemented with 0.3 M mannitol to a concentration of 2% (200 mg/ml) and the pH was adjusted to 7.2-7.4. The solution was sterile filtered through 0.22 μm filter and left in the fridge overnight to remove bubbles. 1940DC were harvested, washed and resuspended in IMDM media supplemented with 2% FBS. Cells were counted with an automated MOXI Z Mini Cell Counter kit (ORFLO®, USA) and a total amount of 5×10^6 cells/ml was mixed with 2% UPLVG alginate. Alginate-cell suspension was mixed with 5 mg/ml *E.coli* K12 strain LPS (LPS-EK, Invivogen, USA) dissolved in IMDM with 2% FBS to the final concentration of 10 μg/ml.

4.9 Formation of alginate microbeads and alginate microstructures

4.9.1 Formation of alginate microbeads using electrostatic bead generator

For the optimization of the collagen-alginate multi-compartmental scaffolds cell free alginate microbeads were produced. Alginate bead formation is largely

described in (123). Alginate microbeads were produced using an electrostatic bead generator that was made by the mechanical workshop at the Department of Physics, Norwegian University of Science and Technology, Trondheim.

LF200S alginate (FMC Biopolymer, Norway) was dissolved in MQ-water with 0,3 M D-mannitol (VWR, USA) under magnetic stirring. LF200S solution was brought to the concentration of 1.8% (w/v) and was aspired in a 1 ml sterile syringe that was placed on a digital syringe pump. The flow rate of the syringe pump was adjusted to 3 ml/h. Tubing was connected to the tip of the syringe and to the needle holder that was connected to a 0.13 mm needle. The needle holder was carefully placed to the bead generator's nozzle holder stand. The holder stand was adjusted to the distance of 2 cm from the surface of the gelling bath. A 95 mm^3 beaker was used as the gelling bath filled with 160 ml of gelling solution. The gelling solution was composed of 0.15 M D-mannitol (VWR, USA), 10 mM HEPES (PanReach/AppliChem, USA), 50 mM $CaCl_2$ (Sigma Aldrich, USA) 1 mM $BaCl_2$ (Sigma Aldrich, USA) dissolved in MQ-water with the pH adjusted to 7.2-7.4. After the bead generator components had been connected the device was turned on the voltage was adjusted to 8 kV. The syringe pump was turned on and the time was monitored until approximately 0.5 ml of alginate had been inoculated into the gelling bath. Afterwards the bead generator and the syringe pump were turned off and the nozzle holder was carefully removed from the apparatus. The alginate beads were let for 10 min into the gelling solution in order to gel properly. In the following step the gelling solution containing the alginate beads was aspired using 25 ml pipettes and the beads were filtered using 40 μm cell strainers adjusted on 50 ml Falcon tubes. The beads were washed with washing solution containing 0.9 % NaCl (VWR, AnalaR NORMAPUR, USA) and 2 mM $CaCl_2$ (Sigma Aldrich, USA) with the pH adjusted to 7.2-7.4. After the washing step the beads were transferred to 15 ml falcon tubes with fully supplemented IMDM media (8% FBS).

4.9.2 Encapsulation of 1940DC in alginate microstructures

Due the incorporation of high amount of endotoxin the use of the electrostatic bead generator was avoided, to prevent contamination of the equipment that was used by the research group for other experimental studies. For the multi-compartmental scaffold system that cells were included alginate microstructures were fabricated manually.

Microstructures produced with encapsulated 1940DC stimulated with LPS or plain alginate. The final concentration of the UPLVG alginate was 1,8% mixed with 1940DC cell suspension to the concentration of 5×10^6 cells/ml and 10 μg/ml LPS in fully supplemented IMDM with 2% FBS. For the formation of empty cell free microstructures 2% alginate solution was brought to the concentration of 1.8% by mixing with fully supplemented IMDM (2% FBS). Aliquots of 5 μl were taken using a 10 μl pipette nozzle and small droplets of random size and shape were arrayed on a 90mm sterile Petri Dish. The petri dish was filled with 10 ml of sterile filtered gelling solution, composed of 0.15M D-mannitol (VWR, USA), 10mM HEPES (PanReach/AppliChem, USA), 50 mM $CaCl_2$ (Sigma-Aldrich, USA) 1 mM $BaCl_2$ (Sigma-Aldrich, USA) dissolved in MQ-water with the pH adjusted to 7.2-7.4. The alginate droplets left to gel for 10 min. The gelling solution was then removed and the resulted alginate microstructures were washed with 10 ml of sterile filtered washing solution that contained 0.9 % NaCl and 2 mM $CaCl_2$ with the pH adjusted to 7.2-7.4. The resulted alginate microstructures with encapsulated 1940DC were

stored in 3 ml of fully supplemented IMDM in 5 ml Eppendorf tubes and stored in ice.

4.10 Collagen-Alginate multi-compartmental hydrogels

Acid solubilized rat tail collagen I (Gibco™, USA) with initial concentration 3 mg/ml was used as a scaffold to form 1,5 mg/ml fibrilar collagen gels. To form 500 µl fibrilar collagen scaffold containing alginate microbeads/microstructures, 250 µl of 3 mg/ml collagen were mixed together with 40 µl 10x HEPES (PanReach/AppliChem, USA), 40 µl 10x RPMI-1640 (Gibco™, USA) 40 µl of 10x $NaHCO_3$ (Sigma, S5761), 24 µl MQ-water, 50 µl of aginate structures suspension with or without activated 1940DC in fully supplemented IMDM (8% FBS), 50 µl of MF2 cell suspension in fully supplemented RPMI-1640 media (10% FBS) and 6.25 µl of 1M NaOH in order to neutralize the pH and initiate the gelation of the collagen. All the preparation of the collagen scaffolds was performed in ice to prevent gelation of collagen. Aliquots of 50 µl were plated into 96-well clear bottom black plates (Corning®, USA), using modified pipette tips where the tip orifice was cut to increase the tip diameter and ensure the aspiration of the alginate structures. The plates were incubated at 37℃ in a 5% CO_2 incubator for one hour. After the gelation of collagen, 50 µl of fresh fully supplemented RPMI media was added on top of the wells. Collagen scaffolds were brought to confocal microscope for imaging.

4.11 Matrigel-Alginate multi-compartmental hydrogels

All pipette tips solutions and plates were kept in the freezer for 30 min and all the procedure was performed in ice. Matrigel scaffolds (13.5 mg/ml, Corning®, #356237, USA) were diluted in 1640-RPMI media (10% FBS) to the concentration of 10 mg/ml. Matrigel was mixed with 0.5×10^6 MF2 cells/ml in fully supplemented RPMI-1640 media (10% FBS). The final concentration of Matrigel was 5 mg/ml. Matrigel mixture was plated into 96-well clear bottom black plates (Corning®, USA) in 50 µl aliquots. Alginate microbeads/microstructures with or without encapsulated 1940DC were picked with sterile tweezers and placed into the wells. Scaffolds were incubated in a 5% CO_2 incubator at 37℃ for 30 min. After complete gelation 50 µl of fully supplemented RPMI-1640 media was added on top of the gels. Scaffolds were brought to confocal microscope for imaging.

4.12 Alginate hydrogels

Chemically modified alginates such as sulfated alginate, 8% POAred and RGD peptide grafted UPLVG alginate were used to fabricate the hydrogels. All hydrogel components were dissolved in buffer contained 25 mM HEPES (PanReach/AppliChem, A 1069.0250), 14 mM sodium citrate (VWR, Prolabo BDH USA), 56 mM fructose (Norsk Medisinaldepot, Norway) and 70 mM NaCl (VWR, AnalaR NORMAPUR, USA) with the pH adjusted to 7.2-7.4.

Sulphated alginate and POAred were synthetized as described above. Sulfated alginate was mixed 1:1 with UPLVG alginate and 8% partially oxidized alginate was mixed 1:3 with UPLVG alginate. The final composition of the hydrogels was 1% alginate, 18 mM $CaC0_3$ (d=0.7 µm, Vicality/ALBAFIL, USA), and 36 mM Glucono-D-Lactone (Sigma-Aldrich, USA). Hydrogels were mixed with 0.5×10^6 MF2 cells/ml and alginate microstructures contained activated 1940DC or plain alginate structures.

The -RGD- sequence peptide grafted UPLVG alginate was produced at NOBIPOL, NTNU, Trondheim and kindly provided. RGD-UPLVG alginate was mixed 1:4 with UPLVG (M_w=237kD) alginate or partially degraded UPLVG (M_w=152kD) alginate. The final composition of the of the RGD-UPLVG alginate hydrogels was 0.5% alginate, 15 mM $CaCO_3$ and 30 mM Glucono-D-Lactone. Hydrogels were mixed with 0.5×10^6 MF2 cells/ml.

Alginate matrices were plated into 96-well clear bottom black plates (Corning®, USA) in 50 µl aliquots and incubated in a 5% CO_2 incubator at 37 ℃ for 2h to form gels. After 2h 150 µl of RPMI with 10% FBS was added on top of the gels and incubated for 30 min. The media was replaced for 2 times in order to fully exchange the cell buffer with media. Finally, the media was removed and the gels brought to confocal microscope for imaging.

4.13 Cell viability assay

To determine the viability of 1940DC cells after encapsulation in the alginate, ethidium homodimer-1 (EthD-1) staining (Invitrogen™, USA) was applied. Viable 1940DC cells would emit eGFP signal only, whereas non-viable cells with compromised plasma membranes would be permeable to EthD-1. The staining solution was prepared by dissolving 4 µl of EthD-1 stock solution in 2 ml of serum free IMDM (IMDM , Gibco™, USA). A 100 µl aliquot of 1940DC cell suspension before encapsulation and a 100 µl aliquot of 1940DC encapsulated in alginate were taken and mixed into separate Eppendorf tubes that contained 100 µl EthD-1 staining solution. The samples were incubated in room temperature for 30 min and transferred to glass bottom petri dishes for confocal imaging. Confocal images were acquired using a Zeiss LSM800 (Carl Zeiss, Germany) confocal laser scanning microscope. A C-apochromat 10x water immersion objective (numerical aperture of 0.45, working distance of 1.8 mm) was used for imaging for the cells in suspension and encapsulated cells. The EthD-1 was excited with a 561 nm laser and the eGFP was excited with a 488 nm laser. The EthD-1 emission was detected with an Airyscan detector at 601-628 nm and the eGFP emission was detected with a GaAsp-Pmt1 detector at 401-546 nm.

4.14 Live cell Imaging

Imaging of the fabricated scaffolds conducted using a Zeiss LSM800 (Carl Zeiss, Germany) confocal laser scanning microscope. A C-apochromat 10x water immersion objective (numerical aperture of 0.45, working distance of 1.8 mm) was used for imaging. The acquisition settings were adjusted using the Zen Blue software (Carl Zeiss). For the acquisition of the eGFP cells were excited with a 488 nm laser and the emitted signal was detected with a GaAsP-Pmt1 detector at 410-546 nm. For the acquisition of the CTRed cells were excited with a 586 nm laser and the emitted signal was detected with an Airyscan detector at 570-601 nm. Pinhole was adjusted to 34-74 µm dependent on the time of acquisition and the signal quality. Laser power was adjusted to 2-10% dependent on the signal quality. Detector gain was adjusted to 500-700 V dependent on the signal quality. For z-stack acquisition the z-distance was adjusted to 20 µm. The digital resolution was optimized using the Zen Blue software to 1024 x 1024 pixels for a focal area of 1277.8 µm x 1277.8 µm corresponding to a voxel size of 1.248 x 1.248 x 20 μm^3. For the collagen-alginate hydrogels 30 minutes time series were set and the total volume was recorded every 200 seconds. For the RGD-alginate and Matrigel-

alginate hydrogels time series were set to 30 minutes and the total volume was recorder every 58 seconds. Sulfated alginate and POAred hydrogels were imaged for 10 or 30 minutes. After fluorescence imaging DIC images of the same z-slice were acquired as a bright field reference. The resolution of the DIC slices was 1936 x 1460 pixels for a focal area of 1.4 x 1.05 mm.

4.15 Second Harmonic Generation and Confocal Reflectance Microscopy

Imaging of the collagen type-I fiber network with incorporated alginate beads in order to evaluate the microarchitecture of the system was conducted on a Leica TCS SP8 MP system (Leica Microsystems, Germany). An HCX IRAPO 25x water immersion objective (NA 0.95, 2.4 mm working distance) was for imaging. The SHG signal was produced by setting the MP laser line to 780 nm at 3.3 W power. For the CRM a White Light Laser was set to 510 nm wavelength with 70% power. The emission for the CRM was detected with a 2x photomultiplier tube (PMT2) adjusted to 600 V gain and the pinhole aperture was optimized to 55.9 μm for the detection of 580 nm wavelength. The SHG signal a 2x HyD detector was used with 250 V gain. The z-distance was adjusted to 0.57 μm and 119 optical sections of 512 x 512 pixel resolution were acquired corresponding to the physical size of 465 μm x 465 μm x 67 μm. The resulted voxel size was 0.91 x 0.91 x 0.57 μm^3.

4.16 Image processing

All images were processed and analyzed using the ImageJ software (NIH). Color intensity of the confocal fluorescence images was adjusted by manually measuring the intensity of cells in-focus and out-of-focus cells. The highest intensity value of the out-of-focus cells was established as a threshold and the images were manually inspected to validate the method. Due to photobleaching and relatively increased proliferation of MF2, which contributed to non-homogeneous signal emission, fluorescence images were adjusted manually after the timepoint of 24h. At the 48h time point in order to compensate for the extended photobleaching effect, color intensity was manually band passed to a narrow level. The noise was removed from the images using a 2 pixel median filter. DIC images were scaled to 1024x1024 pixel and processed manually for color balance and contrast.

Z-stack reconstruction of the confocal fluorescence images was conducted with the ImageJ 3D project function. Initial settings were used and interpolation was optionally applied.

To obtain frame sequence images annotated with cell tracks the Manual Tracking plugin was used and the tracing line was overlaid to the segmented image.

4.17 Live/Dead viability assay

Confocal fluorescence images of 1940DC viability assay were quantified using automated cell counting. The EGFP and the EthD-1 channels were split and the color intensity threshold was established manually as mentioned above. The 3D Object Counter ImageJ plug-in was used to conduct automated cell counting. The threshold was set to 30 and the object size was set to 30-maximum corresponding to the voxel size of a cell. Cell counting was performed for each channel separately and the Live/Dead percentage was calculated by the following formula:

$$\frac{\#\ cells\ EthD1}{\#\ cells\ (EthD1 + eGFP)} \times 100 = Dead\ \% \quad (3)$$

The same procedure was followed for the quantification of cells before and after encapsulation.

4.18 Cell counting

To determine accumulation of the MF2 around the microstructures in collagen under the effect of inflammatory mediators or any external influence, 10 z-stack slices of each sample were chosen. The analysis was undertaken for the 0h, 24h and 48h timepoints. Automated cell counting was conducted with ImageJ 3D Object Counter plugin. Cells were segmented with intensity thresholding that was adjusted dependent to the photobleaching at each timepoint. The minimum value of the size filter varied from 5-30 dependent to the photobleaching. Especially cells at 48 h had been extensively photobleached giving the signal of few pixels.

4.19 Automated Cell Tracking

Cell tracking was performed in ImageJ using the Trackmate plug-in (124). The images were initially processed as mentioned above prior to the analysis. The z-stack dimensions and the frame time were assigned. A Laplacian of Gaussian (LoG) detector was chosen for cell detection since the object diameter was 5-20 pixel. LoG detector has the property to detect objects according to their diameter and color intensity. The blob diameter was set to 20 μm and the intensity threshold was set to 20-50 dependent on the timepoint and the degree of photobleaching. Sub-pixel localization correction was selected and the median filter was turned on. A simple linear assignment problem (LAP) tracker was chosen as a track detector since the current study was not focused on merging or splitting events. The max linking distance was set to 30 μm, and max gap-closing distance was set 15 μm representing ¾ of the cell diameter. Finally, the closing gap frame was set every second time frame. A command was executed and a file in .xml format was obtained that contained the (x, y, z, t) coordinates of all cell trajectories.

4.20 Analysis of tracks

An analysis of tracks was conducted using Trackmate to extract the values of the track displacement, that corresponded to the distance between the first spot and the last spot of the track during time. Further analysis of the cell trajectories and their spatiotemporal coordinate systems was conducted in MATLAB (Mathworks) scripting language with the @msdanalyzer Toolbox (125). Tracks of the cell trajectories generated for each timepoint were inserted into a model structure. Tracks were compensated for drift using the velocity correlation method. This method was the most suitable to apply, since the assessment was focused on moving objects.

The velocity 3D vectors corresponding to each frame of the time series, were calculated with an @msdanalyzer command. The mean speed for each track was calculated based on the following formula, by averaging the speed calculated from every 3D velocity vector at each consecutive time frame of acquisition:

$$\langle speed \rangle = \langle \sqrt{x^2 + y^2 + z^2} \rangle \quad (4)$$

Where x, y and z are the 3D velocity vector coordinates.

The MSD was calculated for each cell trajectory and the MSD vs. t_n graphs were plotted using the corresponding @msdanalyzer commands. Afterwards, a power law was fitted to the curves in order to obtain the alpha (α) exponent value for each trajectory. Fitted power laws with a regression coefficient lower than 0,9 were excluded.

4.21 Statistical analysis

All statistical analysis was conducted in MATLAB using the Statistics and Machine Learning Toolbox. One-way unbalanced ANOVA with post-hoc Tukey test, was used to evaluate statistical significance. The α level of significance was set to 0.05 and $p<0.05$ was considered as a significant difference.

5 Results

5.1 Evaluation of the 1940DC viability after encapsulation

The viability of the 1940DC cell line was decreased after encapsulation into the alginate with external gelation. The percentage of viable cells was 75% before the encapsulation. After the encapsulation procedure the viability of 1940DC reduced to 65%. The results of the Live/Dead assay are shown in a bar chart in Figure 5.1.

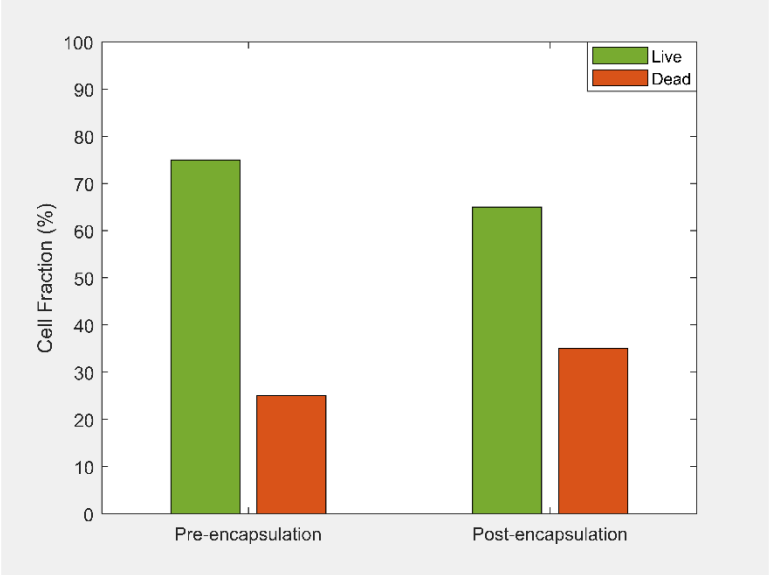

Figure 5.1: Viability results of 1940DC before and after encapsulation in alginate with external gelation. Green color represents viable cells. Red color corresponds to compromised cells. Experimental groups have been plotted against cell fraction (%).

5.2 Multi-compartmental hydrogels as a system to study T-cell migration under inflammatory conditions

5.2.1 Multi-compartmental hydrogels based on collagen and alginate

5.2.1.1 System Evaluation

The collagen-alginate system was optimized in different series of cell free experiments (Figure 5.2) in order to avoid osmotic swelling of the alginate structure that could have a distortive outcome on the surrounding collagen fibrillar network architecture and distribution (Figure 5.2-A). The collagen alginate system was optimized by mixing collagen with an equal concentration of the components found in the media. This avoided osmotic swelling of the beads and the collagen matrix was evenly distributed across all the system area (Figure 5.2-B). The alginate microbeads were distributed at different levels in 3D (Figure 5.2-C).

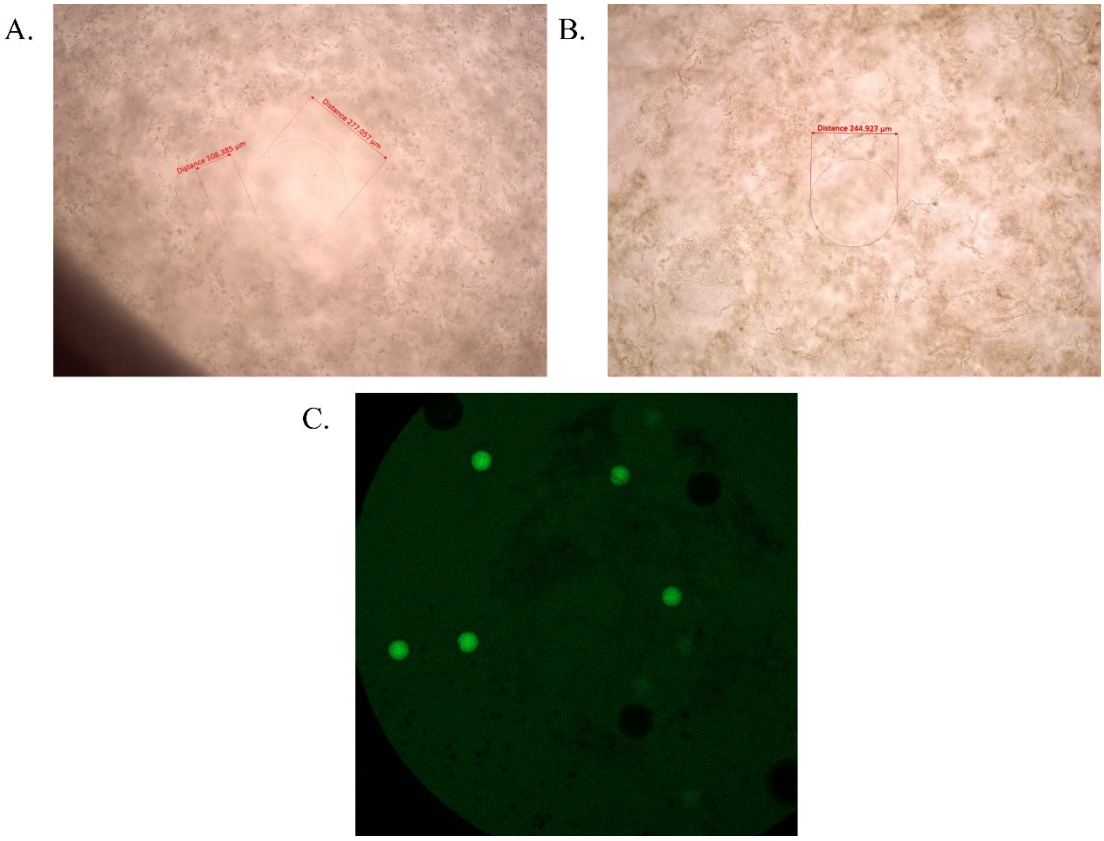

Figure 5.2. Steps followed during collagen-alginate system optimization. (A) Alginate bead in collagen 1.5 mg/ml matrix. A fading gradient of approximately 103 μm radius from the edge of the bead is shown. The bead has been swollen with a resulted diameter of 277 μm. (B) Alginate bead embedded in collagen 1.5 mg/ml matrix under optimized conditions. The bead diameter was measured to 244μm. (C) Fluorescent image with 2.5x air objective of FITC-alginate beads embedded in collagen 1.5 mg/ml matrix under optimized conditions. The alginate beads are randomly distributed along different depth in the collagen. The dark spheres probably represent bubbles that were formed on the top of the gels.

The fibrillar network morphology and distribution was qualitatively evaluated by SHG microscopy and confocal reflectance microscopy. The collagen density was appeared to be evenly distributed across the entire specimen and no density gradient was present around the alginate bead (Figure 5.3). The results indicate that the scaffold fabrication method was effective and the interface architecture would not interfere with the migratory behavior of the T-cells. The pore size was briefly estimated by measuring manually 30 randomly chosen pores in 2D slices. The average pore area was calculated to 771 μm^2 with a standard deviation of 919 μm^2. The minimum pore area size was 34 μm^2 and the was 3436 μm^2. The minimum values corresponded to areas where the density of crosslinked fibers was high. This brief estimation can show a limited contribution of the scaffolds to cell confinement since cell surface occupies the area of around approximately 150 μm^2.

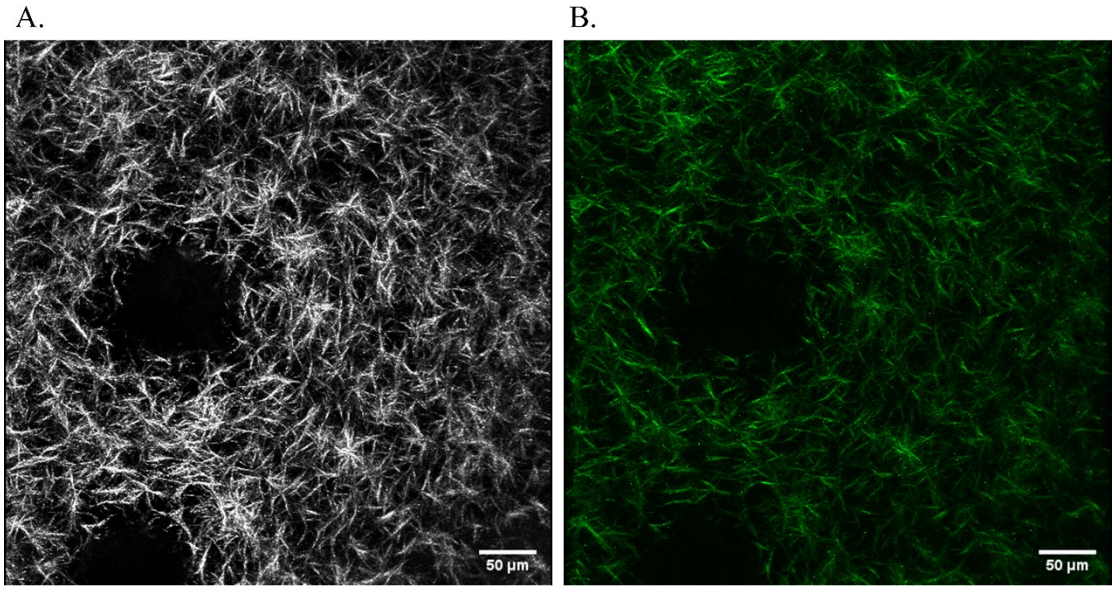

Figure 5.3: Images of the 3D collagen scaffolds (A.) Confocal reflectance microscopy and (B.) SHG microscopy z-stack reconstructions of collagen type-1 fibrillar network with 25x water immersion objective. The circular dark area denotes the alginate bead location. Scale bar 50 µm.

5.2.1.2 Evaluation of MF2 cells migration under pro-inflammatory conditions in collagen

After the assembly of the system was adjusted to the desired context, cells were incorporated in the system. 1940DC were encapsulated into manually produced alginate microstructures with LPS in order to initiate a pro-inflammatory response. The system was additionally tested after incorporation of null alginate microstructures as a control.

The confocal images at 0h, 24h and 48h have shown a distinct accumulation of the MF2 cells towards the alginate structures contained the stimulated 1940DC cells, in contrast to the control sample that contained MF2 with plain alginate structures (Figure 5.4). At 0h of acquisition the number of MF2 around the alginate compartment edges was approximately equal as estimated by cell counting (Figure 5.5). The presence of MF2 around the alginate compartment with 1940DC could be qualitatively observed after 24h of incubation (Figure 5.4-A, 24h). At 48h the amount of 1940DC had been further increased (Figure 5.4-A, 48h). In the control sample the cell density was also increased throughout the timepoints of 24h and 48h since the majority of the MF2 had proliferated (Figure 5.4-B, 24h-48h). Three-dimensional z-stack reconstruction has indicated a similar effect on the accumulation of MF2 cells during the 24h and 48h timepoints between the samples (Figure 5.4, A-B,24h-48h). The increased activity of the MF2 cells around the alginate microstructure with the 1940DC encapsulated was also observable at the 48h after incubation by the observation of 3D movies that generated through 30 min of time lapse imaging (S1-S3 Supplementary movies). The migration of the MF2 cells into the alginate structure was excluded despite their stain signal emitted from the alginate compartment (Figure 5.4-A, 48h). The CTRed signal that is shown in the images is an artifact and probably is a result of the 1940DC phagocytic activity and debris originated by the MF2 cells.

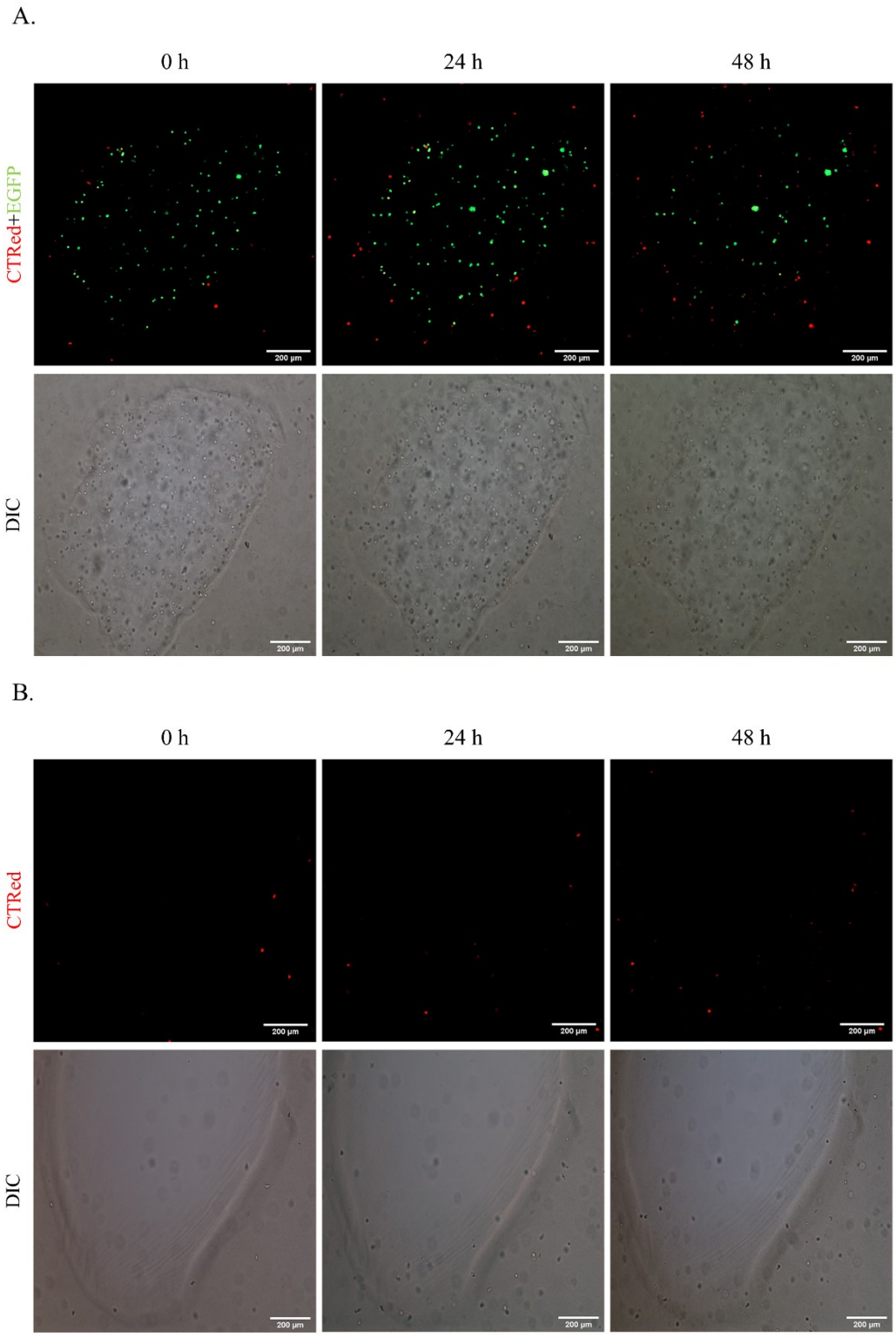

Figure 5.4: Confocal fluorescence images and DIC images of the collagen-alginate multi-compartmental hydrogels. The green color corresponds to the 1940DC EGFP signal and the red color to the MF2 CTRed signal. DIC images indicate the presence of the alginate compartment in the center surrounded by collagen. (A) MF2 cells (red) and alginate with encapsulated 1940DC (green) at 0h, 24h and 48h of acquisition. (B) MF2 cell (red) and plain alginate at 0h, 24h and 48h of acquisition. Scale bar 200 µm.

This artifact was determined from the comparison of the DIC images with the fluorescence images at locations of the alginate where the CTRed signal was emitted. Finally, by the observation of the time-lapse movies none motility events corresponding to the CTRed signal located at the 1940DC-alginate area were shown. In contrast to the colocalized signal, the presence of the MF2 cell in the alginate was excluded.

The accumulation of MF2 in the specimen was estimated by counting cells in a selected number of z-stack slices. The accumulation of the MF2 towards the microstructures with encapsulated 1940DC was higher after 24h, while it was increased exponentially at 48h compared to the absence of pro-inflammatory mediators (Figure 5.5). In the absence of 1940DC in the system, the number of cells was increased linearly in between the consecutive timepoints, probably indicated the uninfluenced proliferation of the MF2 in collagen. The results suggest that the presence of activated 1940DC augmented the proliferation or the further migration of MF2 outside the focal volume, towards the inflammatory microenvironment.

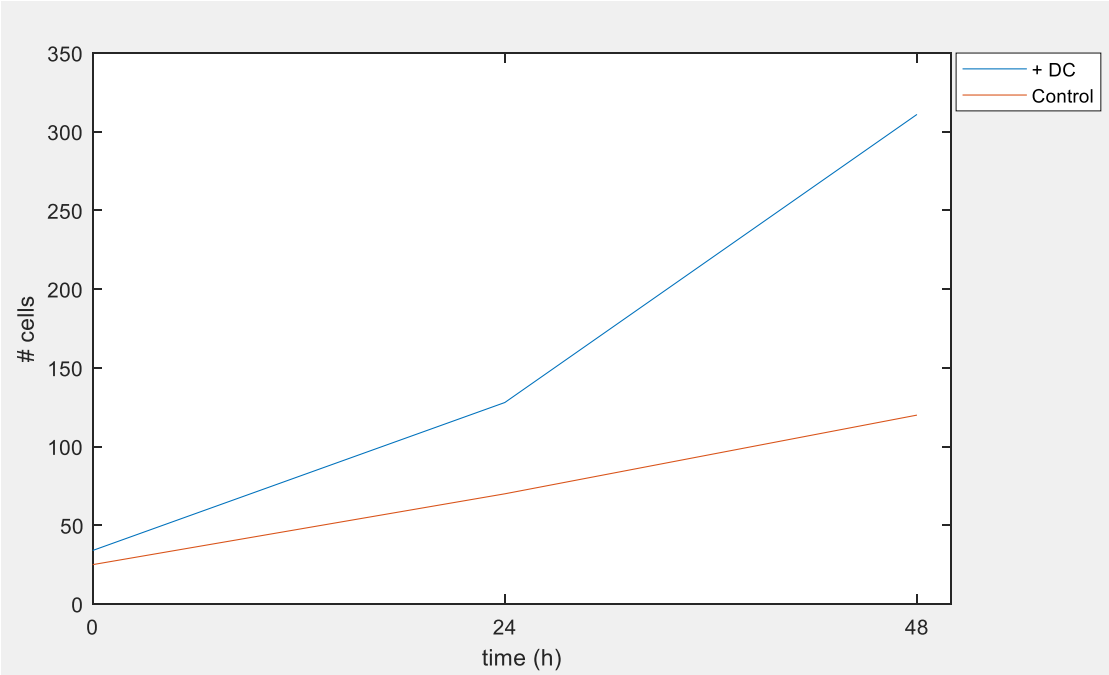

Figure 5.5: MF2 cell number under the presence or the absence of LPS stimulated 1940DC in the system. The red line denotes the number of MF2 detected in the system incubated with alginate microstructures without encapsulated 1940DC. The blue line denotes the number of MF2 detected in the system incubated with alginate microstructures where stimulated 1940DC were encapsulated.

The vast accumulation of the MF2 cells around the alginate microstructure with the stimulated 1940DC compared to control conditions, can be shown in the z-reconstructions of the entire imaged volume (Figure 5.6-A, -B). After one day of incubation, (Figure 5.6-A, -B, 24h) a higher amount of cells was observed in both samples, while the amount of cells around the alginate compartment with the 1940DC, appeared to be further increased. At 48h, (Figure 5.6-A, -B, 48h) the alginate microstructure with the encapsulated 1940DC was overwhelmed by the MF2, whereas in the sample with the null alginate microstructure, MF2 were homogeneously spread around the specimen. Those observations further support the MF2 accumulation around the alginate microstructures

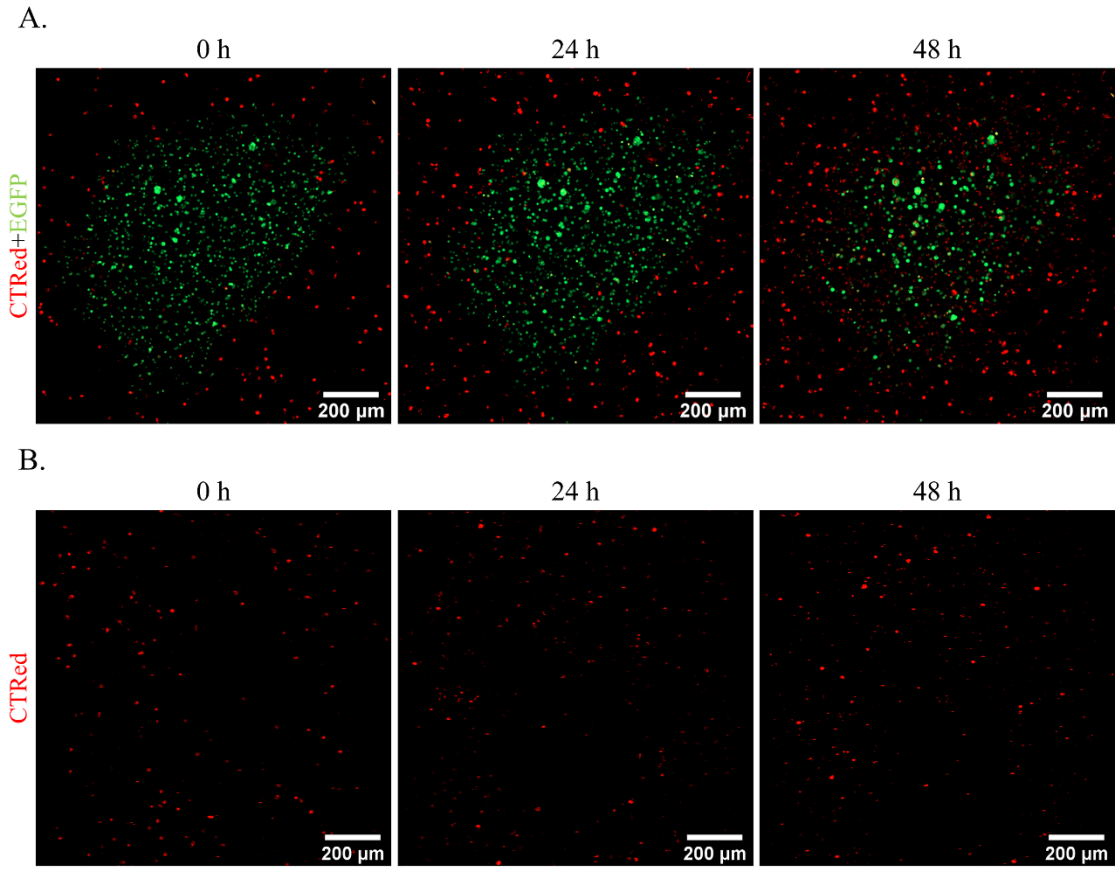

Figure 5.6: Projections of the collagen-alginate multi-compartmental hydrogels. (A). Projections of the encapsulated 1940DC cells (green) surrounded by MF2 cells (red) at 0h, 24h and 48h of acquisition. (B) Projections of the MF2 cells (red) at 0h, 24h and 48h of acquisition (control sample-no DC).

5.2.1.3 Tracking results

The quantitative evaluation of the MF2 cells migration in response to an inflammatory microenvironment was tested using automated cell tracking. For more convenient descriptive purposes the timepoints were chosen to be assigned in respect to the imaging of the system at 0h, 4h, 6h, 8h, 24h and 48h. Assuming that the scaffolds were incubated for 1h prior to the acquisition and 1940DC had been activated 3h prior to system assembly, 0h correspond to 1h in respect to the MF2 and 4h in respect to the 1940DC. Stimulated 1940DC however, had been kept in ice after encapsulation until the scaffolds were assembled, in order to slow down metabolism and prevent the early secretion of pro-inflammatory mediators. The quantitative results of migration were compared between the consecutive timepoints for each condition, reflecting thus the progressive character of migration throughout time under the influence, or not, of pro-inflammatory mediators.

The 3D tracks generated for each individual cell trajectory are presented in Figure 5.7.

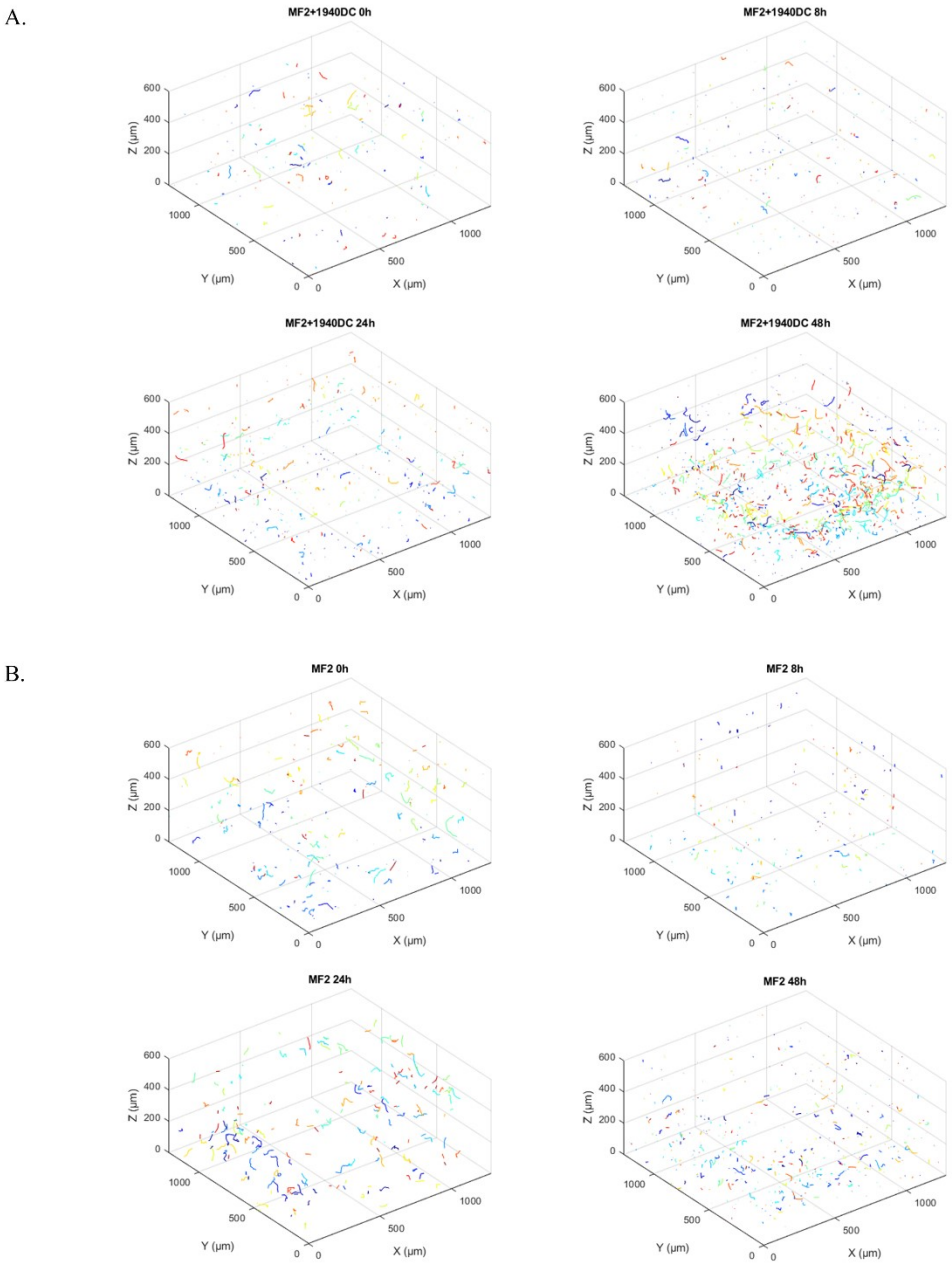

Figure 5.7: 3D track plots of the MF2 cell trajectories in alginate-collagen multi-compartmental hydrogels. (A) Track plots of MF2 cells in the presence of 1940DC, at 0h, 24h and 48h of acquisition. (B) Track plots of MF2 cells in the absence of 1940DC, at 0h, 24h and 48h of acquisition.

By obtaining the displacement for each individual cell trajectory, the distances that MF2 migrated at the different timepoints in the absence or in the presence of stimulated 1940DC could be estimated. In the sample where 1940DC were present no significant differences ($p>0.05$) were detected regarding cell displacement during the consecutive timepoints of 0h to 24h. MF2 displacement was then significantly increased ($p<0.05$) at 48h compared to 24h. Similar trends can be observed in the displacement spreadplot (Figure 5.8-A).

For the sample that did not contain 1940DC, cell displacement was significantly decreased ($p<0.05$) during 4-8h compared to the initial timepoint of 0h. At 24h,

cell displacement was significantly increased ($p<0.05$) compared to 8h. Finally, at 48h cell displacement was significantly decreased ($p<0.05$) compared to 24h. The trends of the MF2 displacement in respect to time for the sample that 1940DC were not included can be observed in the displacement spreadplot (Figure 5.8-B).

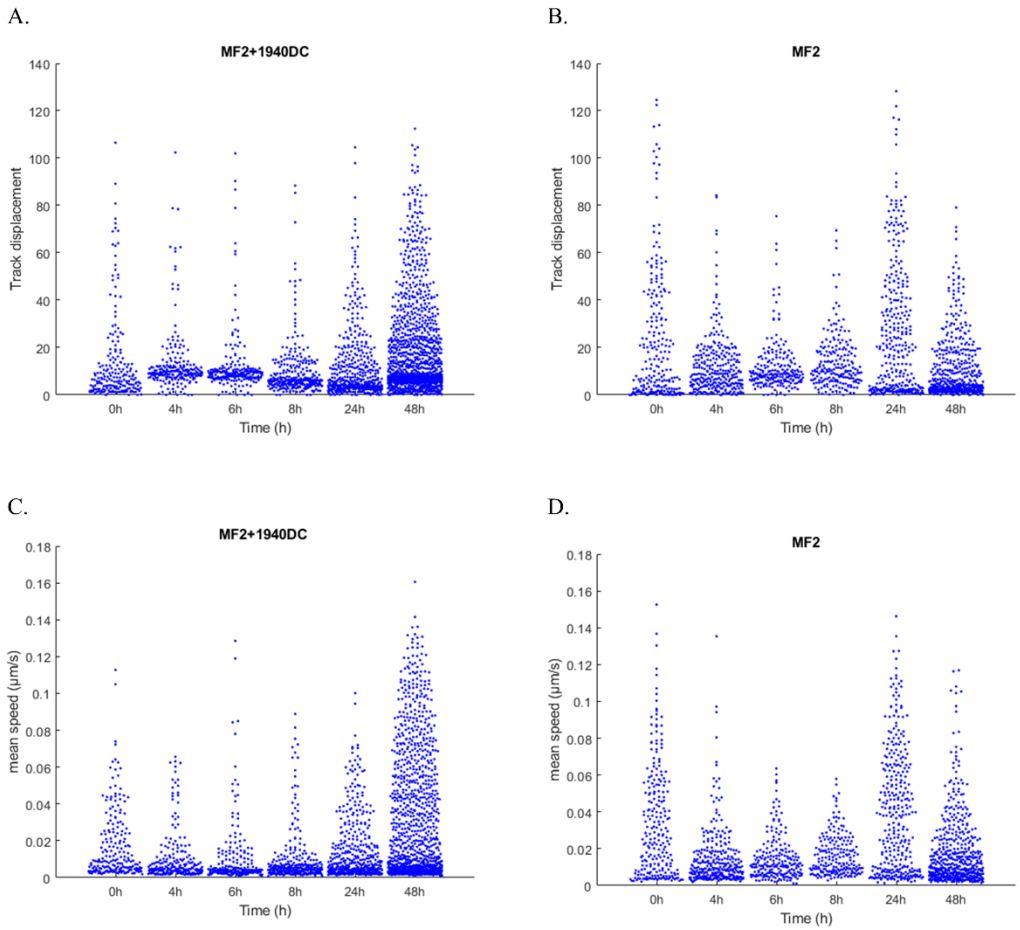

Figure 5.8: Mean speed and displacement beeswarm plots of the collagen-alginate multi-compartmental hydrogels. (A) Displacement of all cell trajectories in the presence of 1940DC at 0h, 4h, 6h, 8h, 25h and 48h of acquisition. (B) Displacement of all cell trajectories in the absence of 1940DC at 0h, 4h, 6h, 8h, 25h and 48h of acquisition. (C) Mean speed of all cell trajectories in the presence of 1940DC at 0h, 4h, 6h, 8h, 25h and 48h of acquisition. (D) Mean speed of all cell trajectories in the absence of 1940DC at 0h, 4h, 6h, 8h, 25h and 48h of acquisition.

Coupled to the distances crossed by each individual cell, the accompanied speed profile could be estimated (Figure 5.8 -C, -D). Graphically the MF2 speed in the sample where 1940DC were included, showed a stable profile during the first 24h with most of cells' mean speed less than 0,08 μm/s and few events over 0.08 μm/s recorded (Figure 5.8-C). The mean speed was shown to be highly elevated at 48h with a vast cell density characterized by values greater than 0.08 μm/s and even greater than 1 μm/s (Figure 5.8-C). At that timepoint individual trajectories recorded a mean speed over 1.4 μm/s (Figure 5.8-C). Statistical analysis revealed no significant differences ($p>0.05$) at 4h compared to 0h. No significant differences were also detected between the 4-24h sequence. The mean speed was found to be significantly increased at 48h compared to 24h.

In the sample where activated 1940DC were not contained the MF2 mean speed was significantly ($p<0.05$) decreased at 4h compared to 0h. No significant differences detected in between 4h, 6h and 8h. Some cells at 4h maintained a similar mean speed levels to 0h, but a huge density was below 0.08 μm/s, but at 6h and 8h it was dropped below 0.06 μm/s (Figure 5.8-D). The mean speed of the population was significantly increased ($p<0.05$) at 24h but did not overcome those of 0h. At 0h and 24h cells recorded mean speed values over 0.08 μm/s, while a proportion of cells, overcame the value of 0.1-0.12 μm/s (Figure 5.8-D). Finally, at 48h the mean speed of the entire population was significantly decreased ($p<0.05$) compared to 24h. As expected, cell speed followed similar trends to displacement. There was a distinct difference in the motility of the MF2 under the effect of pro-inflammatory mediators compared to reference condition where 1940DC were not included in the system. In conclusion under the influence of pro-inflammatory mediators the cells' speed, and the migrated distances did not show to be affected during the first 24h, while they were significantly elevated after 48h.

The MSD plots not only reflected similar trends discussed above but also provided a better image of the migration evolution throughout time. In the sample where 1940DC were included, the MSD curve levels are shown to follow a similar fashion at 0h, 4h and 6h (Figure 5.9-A), while a low reduction at the MSD levels can be observed during 8h (Figure 5.9-A). Furthermore, a similar trend to the previously mentioned timepoints could be observed at 24h. The levels and the density of the displaced trajectories can be distinguished at 48h (Figure 5.9-A). In the sample where 1940DC were absent (Figure 5.9-B) the MSD plots have shown an elevated activity during the initial timepoint of acquisition with many trajectories performed remarkable displacements. The MSD levels were then reduced during 4h, 6h and 8h while no similarities could be observed, compared to 0h (Figure 5.9-B). The trends of 0h and 24h plots are comparable instead of the difference that the number of trajectories had been increased at 24h (Figure 5.9-B). This increase was remarkable compared to the previous timepoints, but did not overcome that of the initial acquisition at 0h. Finally, at 48h the MSD of the trajectories was decreased to levels analogous to those at the intermediate timepoints of 4h, 6h and 8h (Figure 5.9-B), which suggests that the motility was decreased to low levels at 48h.

In every acquisition timepoint, an anomalous behavior in respect to time can be observed in the MSD graphs. A cell intrinsic evolution of the motion can be distinguished, by looking at the MSD curves that recorder by each individual cell trajectory. The MSD curves do not follow a continuous fashion throughout time, while various transitions can be detected. This transient behavior could be coupled to fluctuations in speed in between time of observation, or a biased transition to an alternative search strategy dependent to external factors. The source of those transitions could be owed to structural matrix characteristics or to a bioactive factor that altered motility.

A.

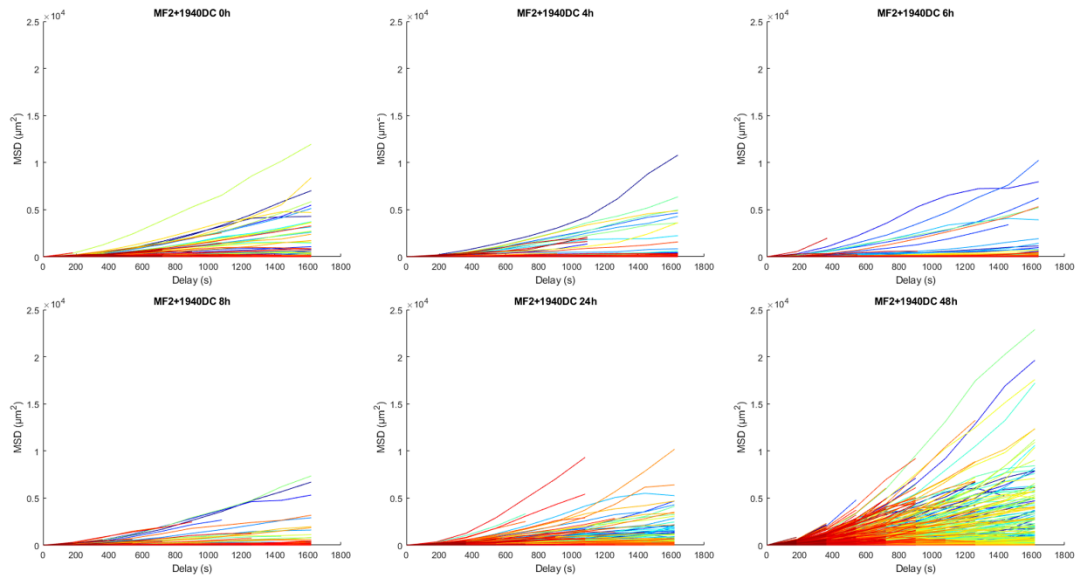

B.

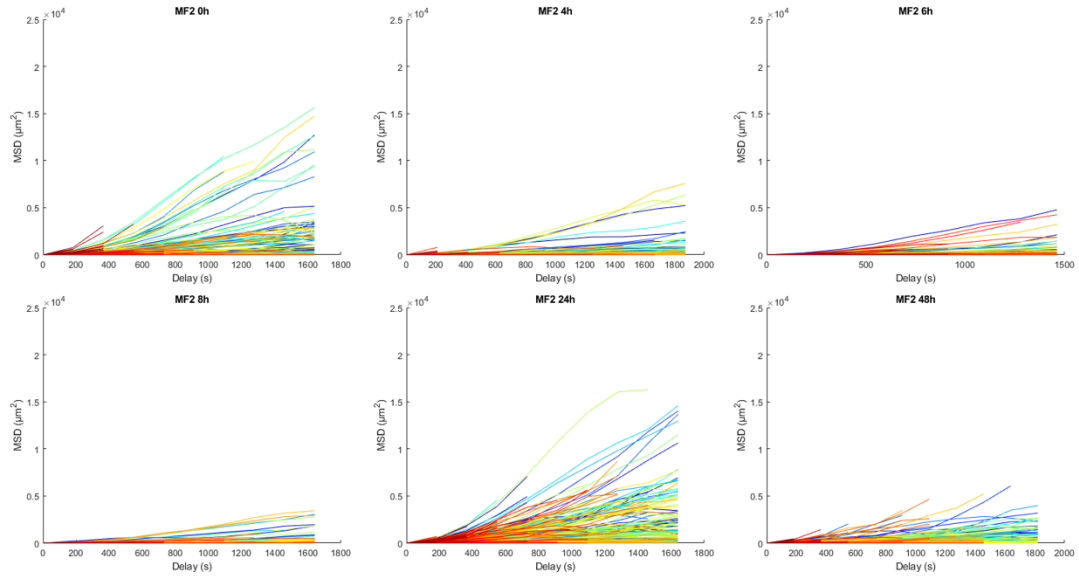

Figure 5.9: MSD plots of the cell trajectories in the collagen-alginate multi-compartmental hydrogels. (A) MSD plots of all the MF2 trajectories at 0h, 4h, 6h, 8h, 24h and 48h of acquisition in the presence of 1940DC. (B) MSD plots of all the MF2 trajectories at 0h, 4h, 6h, 8h, 24h and 48h of acquisition in the absence of 1940DC.

5.2.1.4 Motility patterns

The estimation of the MSD slope plotted on a logarithmic scale, the alpha (α) exponent which reflected the overall mode of motion of each individual cell, during the time interval in each acquisition could be calculated. The α exponent of time analogous to MSD of each individual trajectory, was calculated and the results are represented by distribution histograms (Figure 5.10). In the same logic as before, the comparison was carried out by assessing differences in the overall profile during the consecutive timepoints of acquisition, for each condition separately. That revealed the progressive character of the overall MF2 motility patterns during the experiment, under the effect of pro-inflammatory mediators or under non-stimulated conditions.

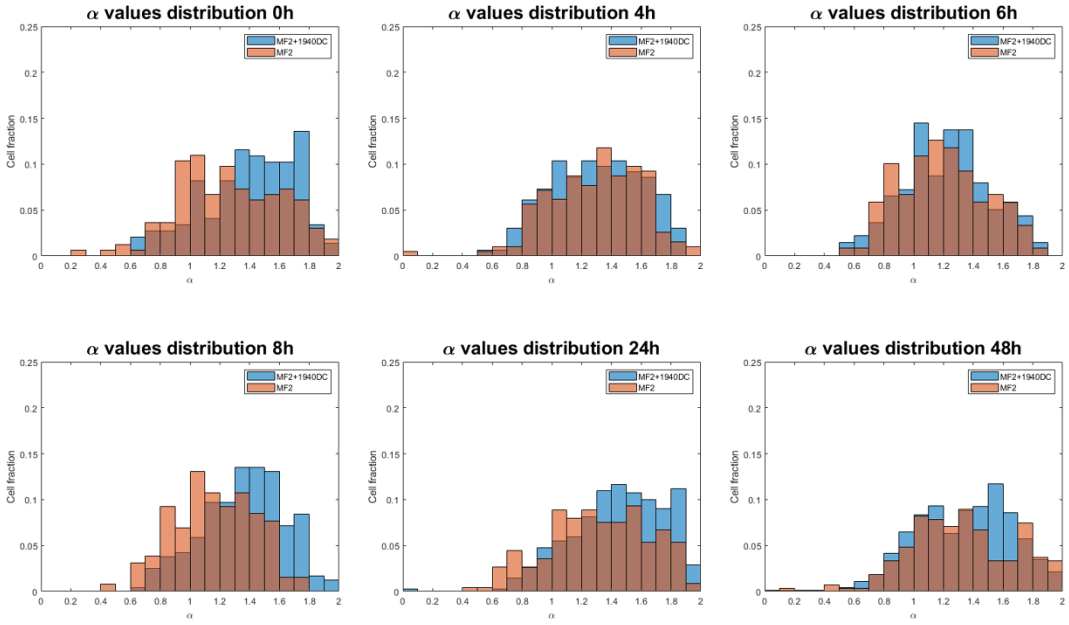

Figure 5.10: Histograms of the α exponent values distribution against the cell fraction collagen-alginate multi-compartmental hydrogels. Both samples are represented on the same histogram for each timepoint of acquisition (0h, 4h, 6h, 8h, 24h and 48h). Blue bins correspond to the sample that 1940DC were included. Red bins correspond to the sample that 1940DC were not included.

In the sample where activated 1940DC were present, the α exponent values of the cell trajectories were significantly decreased ($p<0,05$) from 0h to 4h rendering a more intermediate profile where subdiffusive random walks and superdiffussive events could be observed. A significant decrease ($p<0,05$) was revealed at 6h, compared to 4h, showing a lower activity in terms of speed fluctuations and overall displacement. At 8h a significant increase ($p<0.05$) was resulted compared to 6h with a subsequent significant increase occurred at 24h against 8h. At this point MF2 cells switched to more superdiffusive patterns. Finally, the α values were significantly decreased at 48h compared to the previous timepoint of 24h. During that point, the activity could be described by a mixed character that was observable in the movies. Some of the MF2 had formed distinct clusters at certain locations around the microstructures exploiting the information, to a point that probably a higher grade of stimulators was released. Other cells were rapidly crossing long distances, probably in order to migrate to a distant location (S3 Supplementary movie).

In the sample where only MF2 were present, α values were significantly decreased ($p>0.05$) in a sequential fashion between 0h-4h and 4h-6h, while no significant difference was detected between 6h and 8h. That could be possibly relevant to reduction in motility and confinement during those timepoints. A significant increase ($p<0.05$) of the α values was observed at 24h compared to the previous time point of 8h. At that point, the migration acquired a more superdiffusive character. No significant differences ($p>0.05$) were detected between 24h and 48h timepoints showing no alterations in the overall motility patterns. The α exponent values of the MF2 at all timepoints were more evenly distributed in the sample where the 1940DC were absent.

The motility of the MF2 was shown to acquire a different progressive character dependent on the influence of pro-inflammatory mediators. In both samples subdiffusive and superdiffusive events took place.

5.2.2 Multi-compartmental hydrogels based on Matrigel and alginate

5.2.2.1 Evaluation of MF2 cells migration under pro-inflammatory conditions in Matrigel

The vicinity of the MF2 invasion was tested in the alginate-Matrigel multi-compartmental hydrogels at 0h and 96h (Figure 5.11). Matrigel as a scaffold of different consistency could reveal the behavior of the MF2 migration in a different matrix architecture and composition. At the initial timepoint of acquisition (0h) MF2 cells were distributed evenly in both samples around the alginate compartment (Figure 5.11-A,-B, 0h). After 96h the MF2 cells had formed a distinct band around the alginate structure that contained stimulated 1940DC with LPS, in contrast to the control sample where any distinct layer of cells had been formed no matter the increase of the cell density (Figure 5.11-B, 96h). An increased cell density at 96h could be observed in the sample where the activated 1940DC were encapsulated in the alginate compartment that could be proportional to the sample where MF2 cell were plated alone. Additionally, despite the red signal emitted from the alginate area, the transmigration of the MF2 from the Matrigel to the alginate interface was excluded. The overlap of red and green color could be owed to the phagocytic activity of the 1940DC, while this could be further studied by comparison of the DIC images with the fluorescence images. It was clearly shown that instead of the red signal emission only single cells were found that corresponded to 1940DC (Figure 5.11-A, 96h zoomed). Additionally, the EGFP signal is shown to be reduced at 96h, which could indicate a reduction in the viability of the 1940DC. The results obtained from the Matrigel multi-compartmental scaffolds could suggest a directed migration of the MF2 towards the structure with the encapsulated activated 1940DC compared to the reference conditions where pro-inflammatory mediators were excluded.

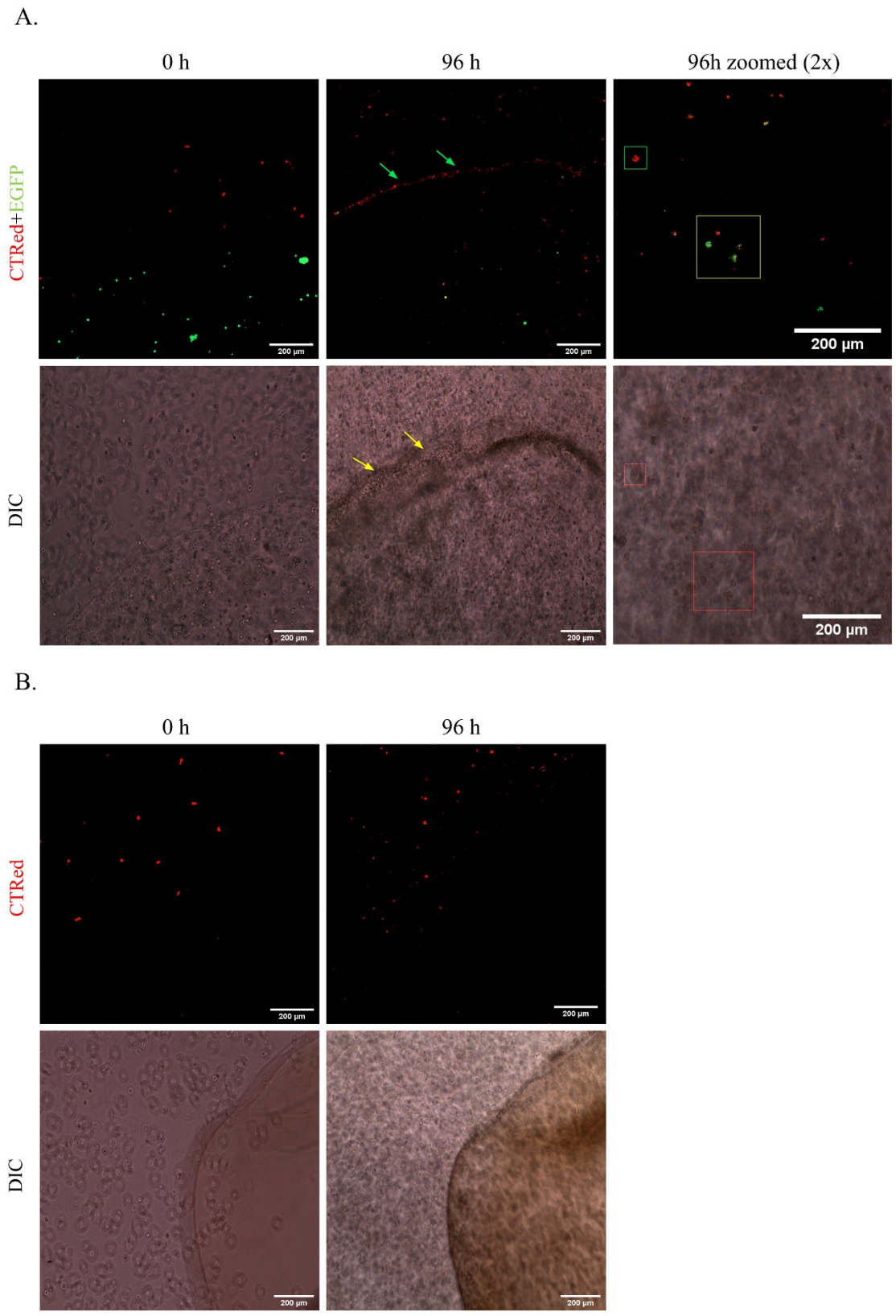

Figure 5.11: Confocal fluorescence images and DIC images of the Matrigel-alginate multi-compartmental hydrogels. (A) Confocal fluorescence images (upper panel) with the corresponding DIC image (lower panel) at 0h and 96h of acquisition. MF2 (red) cells are localized in the Matrigel compartment and 1940DC (green) are encapsulated in the alginate structure. Arrows at the timepoint of 96h indicate a band has been formed by the MF2 around the alginate structure. 2x digital zoom cell in boxes represents the artifact of overlapping

green and red color where only single cells can be observed where red and green channels are emitted. (B) (A) Confocal fluorescence images (upper panel) with the corresponding DIC image (lower panel) at 0h and 96h of acquisition. MF2 (red) cells are localized in the Matrigel compartment around a plain alginate structure. Scale bar 200µm.

5.2.3 Multi-compartmental hydrogels based on alginate

5.2.3.1 Evaluation of MF2 cells migration under pro-inflammatory conditions in sulfated and partially oxidized-reduced (POAred) alginate

The POAred and sulfated alginates were characterized using SEC-MALLS. The results of the chemical composition, degree of substitution and M_w of the modified alginates are described in Table 4.1. UPLVG alginate with encapsulated 1940DC was embedded into scaffolds based on sulfated alginate or POAred. The multi-compartmental hydrogels were fabricated and the motility of the MF2 was tested at 0h (Day0), 24h (Day1) and 48h (Day2). No migration or activity was detected in the scaffolds at the times of acquisition. Viability assay would have helped to determine if the cells were viable in the scaffolds. However, due to time restrictions the possibility to follow up a viability assay in those samples was limited. The immobilization and the inactivity of MF2 cells in the sulfated alginate and POAred hydrogels is shown respectively in S5 and S6 supplementary movies.

5.2.4 Evaluation of MF2 cells migration in RGD-Alginate hydrogels

The motility of the MF2 was tested in two different M_w UPLVG alginates mixed with 20% RGD peptide grafted alginate. An additional compartment with encapsulated 1940DC was not employed in the RGD-alginate hydrogels. Image acquisition was followed during the first 24h after the gels were casted. MF2 motility was detected at the 0h (Day 0) of acquisition and was increased after 24h (Day 1).

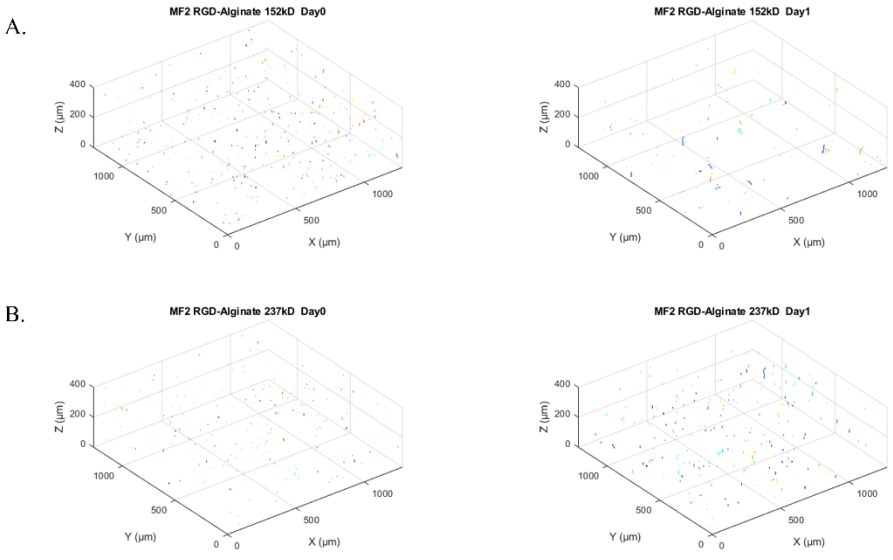

Figure 5.12: 3D track plots of the MF2 cell trajectories in the UPLVG:RGD alginate hydrogels. (A) Track plots of MF2 cells in 152kD UPLVG:RGD alginate at Day0 (left) and Day1 (right). (B Track plots of MF2 cells in 237kD UPLVG:RGD alginate at Day0 (left) and Day1 (right).

5.2.4.1 Quantitative results

All cell trajectories detected via automated cell tracking are presented in 3D plots Figure 5.12. Track displacement was found significantly higher ($p<0,05$) at Day0 for the 152kD UPLVG compared to the 237kD UPLVG sample. At Day1, motility was increased in both samples while the displacement found to be significantly higher in the 237kD UPLVG sample ($p<0,05$) compared to the 152kD UPLVG sample. At Day 0, no significant differences ($p>0,05$) were found in cell mean speed between both samples. The majority of the MF2 did not overcome the value of 0,04 μm/s. At Day 1, mean speed was significantly increased ($p < 0,05$) for both samples while was significantly higher in the sample composed of 152kD UPLVG alginate, where single cell events recorded values greater than 0.12 μm/s. Displacement and speed spreadplots are shown in Figure 5.13(-A Day0,-B Day1).

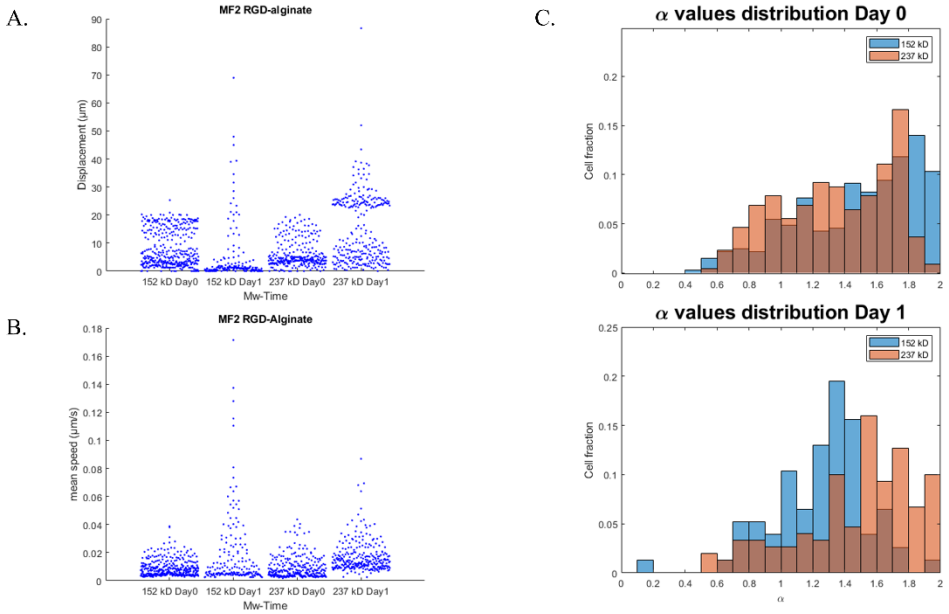

Figure 5.13: Automated cell tracking results of the MF2 in the UPLVG:RGD alginate hydrogels. Displacement (A.) and mean speed (B.) beeswarm plots. Cell trajectories are grouped according to UPLVG Mw and day of acquisition. (C) Histograms showing the distribution of the α exponent values at Day0 (C-upper panel) and Day1 (C-lower panel). Blue bin color corresponds to 152kD UPLVG and red bin color to 237kD UPLVG.

The MSD curves (Figure 5.14) in both samples have denoted identical differences regarding the time of acquisition, while a 10-fold increase was shown in the MSD at Day1, in agreement with the increased migration. At Day0 cell trajectories in both M_w UPLVG alginate reached a maximum MSD of 500 μm^2 (Figure 5.14-A) while at Day 1 the majority in both samples exceeded the MSD of 1000 μm^2 with single cell events reached approximately the values of 4000 μm^2 in the 152kD UPLVG and 7000 μm^2 in the 237kD UPLVG (Figure 5.14-B). The analysis of the motility patterns was shown to be of a superdiffusive character for the majority of the trajectories, particularlly during Day0 in both M_w samples (Figure 5.13-C, upper panel). Those superdifusive events, could had been generated due to noise from cells that contributed to a negligible instantaneous displacement lower than 10μm, probably relevant to blebbing or protrusion elongation. In the 152kD sample during Day1, where the cell number was lower, the distribution of the α values was shown to follow a more normal regime and the overall result can explain easier the migration patterns that where followed in the hydrogel (Figure 5.13-C, lower panel). On the

other hand, in the 237kD sample the motility could be described by a more superdiffusive fashion (Figure 5.13-C, lower panel). Effects of drift, due to the imaging system were high for the 237kD sample during Day1. No matter the drift correction that was applied the results could have been affected. This effect can be also observed in mean speed spreadplot (Figure 5.13-B, 237kD-Day1), where a dense band of cells is distant to 0.

The shape of the MSD graphs has shown trends, that could be more relevant to negligible displacement of some MF2 cells, that could be owed to confinement. However, similar to the observations during Day0 instantaneous displacements could have contributed to the increased α exponent values.

Finally, a similar anomalous regime could hold for the migration behavior at both days of observation, where a mixed exponential profile of the MSD, could be distinguished for both M_W samples. The variability in the progression of the MSD curves could reveal transient behavior that could be accompanied with confinement or rapid release through the pores of the hydrogel.

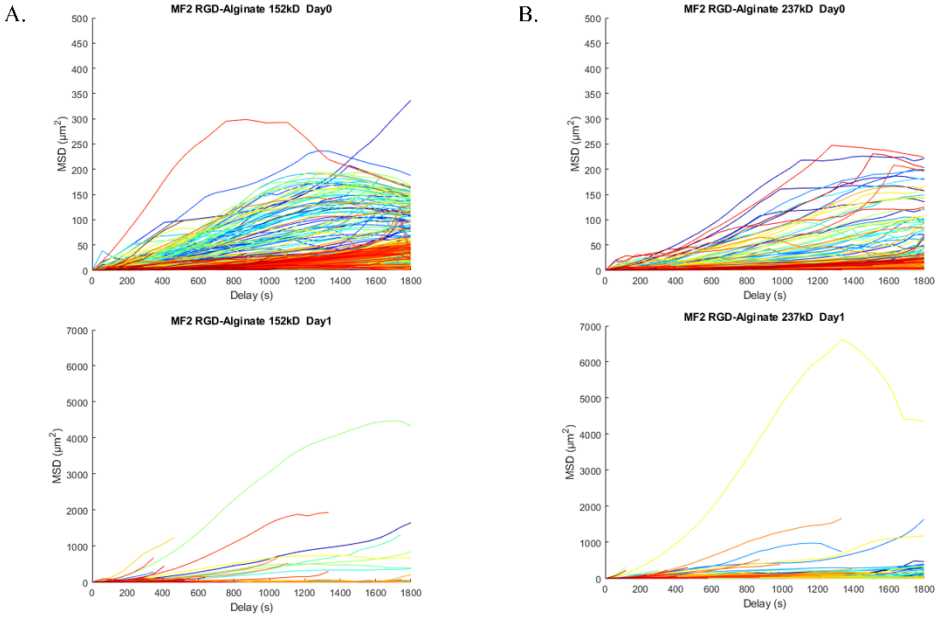

Figure 5.14: MSD plots of the MF2 trajectories in the UPLVG:RGD alginate hydrogels. (A) MSD plots of the MF2 trajectories in the 152kD UPLVG:RGD scaffold at Day0 (upper panel) and Day1 (lower panel). (B) MSD plots of the MF2 trajectories in the 237kD UPLVG:RGD scaffold at Day0 (upper panel) and Day1 (lower panel).

5.3 Morphological characteristics in different biomaterial interfaces

MF2 cells were shown to retain different shapes and morphological features, as it was found by qualitative investigation at different time frames from the time lapse fluorescence images (Figure 5.15). Optimization of the digital image resolution during the acquisition allowed zooming during image processing. This feature facilitated the observation of morphological features in a reasonable resolution where events could reflect the bioactivity of the MF2 in each biomaterial and highlight interactions that could be correlated with physicochemical properties of the different interfaces.

The morphology of migrating MF2 in the fibrillar collagen scaffold (Figure 5.15, top) followed a more universal shape that could be relevant to amoeboid migration. MF2 retained an identical T-cell shape with a flattened leading edge where sort protrusions were formed. At the trailing edge, the T-cell uropod was distinguished from the rest of the cell compartments. The cell translocation was continuous regardless any transitions in the track orientation that could probably reveal that cells followed the collagen fibers. During the time sequence, leading edge demonstrated a dynamical remodeling. However, this was not extensive and could be more relevant to ruffling. The morphology of the MF2 cells in collagen type-I scaffolds is presented in S1-3 supplementary movies.

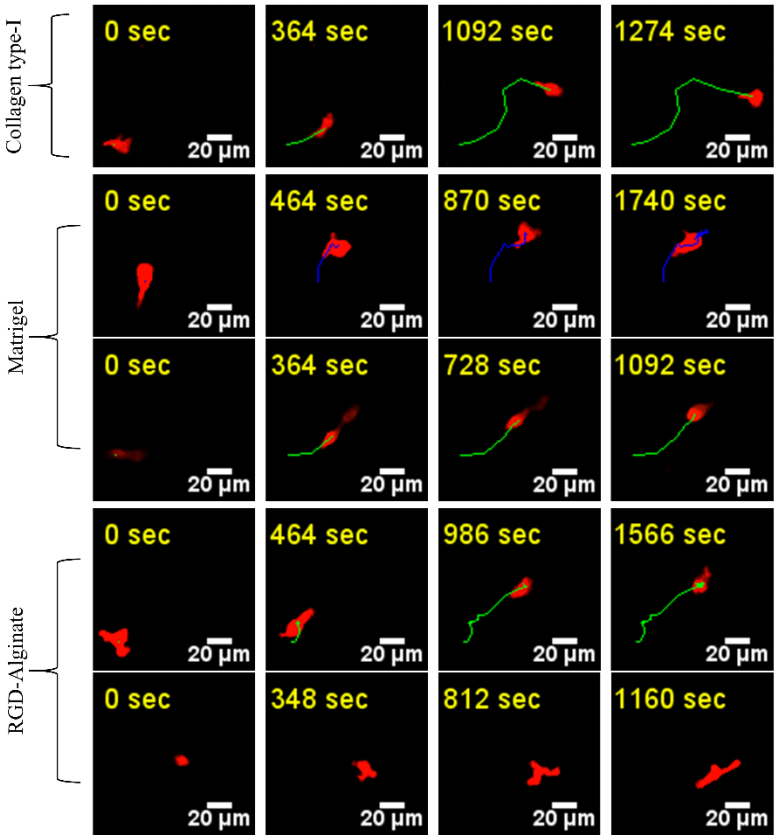

Figure 5.15 :Timelapse fluorescence images showing morphological features of the MF2 during motion in different biomaterial interfaces. Fibrillar collagen (up), Matrigel (middle), RGD-Alginate (bottom). The colored lines represent the track the cell has followed through time.

In the Matrigel scaffold, MF2 cells were found to displace in a non-uniform morphological manner (Figure 5.15, middle). However, their locomotive profile in the Matrigel could be categorized in two separate events or modes. The first sequence (Figure 5.15, Matrigel, top) was highlighted by a similar shape to that was found in the fibrillar collagen scaffold. The characteristic uropod at the trailing edge and a flattened leading edge. However, in the Matrigel the leading edge was shown to retain a more flattened shape. Degree of cell compression would be difficult to estimate, since the z-distance of acquisition (20μm) did not result to a proper 3D reconstruction in the single cell scale. The dynamic remodeling of the flattened leading edge was accompanied by more extended protrusions and membrane blebbing. Translocation was not continuous with retrograde events, where the cell direction was alternating. Non interrupted translocation was also

detected. The second mode of locomotion that was found in the Matrigel scaffolds was characterized by a highly extended and narrowed leading edge while the uropod structure in the trailing edge could not be certainly highlighted. A "wasp"-like shape was obtained in certain frames with the finely bundled leading edge hauling the less extended trailing edge (Figure 5.15, Matrigel, bottom). Videos of migrating MF2 cells in Matrigel scaffold are provided in S4 supplementary movie.

Certain attributes in the cell shape were detected in the RGD-alginate during motion. It could be superficially assumed that the cellular morphology rendered in the RGD-alginate hydrogels could be comparable to that in the Matrigel. Similar flattened or elongated shapes where observed with distinct protrusions and membrane blebbing at the leading edge (Figure 5.15, RGD-alginate, top). However, some events in the RGD-alginate were highly on-the-spot (Figure 5.15, RGD-alginate, bottom). Retrograde events were detected as in Matrigel, while other cells instead were able to follow longer tracks. MF2 cell migration in RGD-alginate hydrogels is presented in S7 supplementary movie.

6 Discussion

6.1 Multi-compartmental hydrogels based on alginate and collagen

The initial aim of the current project was to engineer multi-compartmental hydrogels in order to produce an *in vitro* platform to investigate cell migration in 3D. The goal was to produce alginate beads with an encapsulated bioactive factor embedded in a surrounding matrix that would constitute the compartment where cell motility would be captured. To achieve that, alginate beads of 200-300μm produced with an electrostatic bead generator were incorporated into different biomaterials. It was necessary that the alginate compartment would not interfere with stability of the surrounding matrix and extensive swelling of the alginate bead would be avoided.

Collagen was used as an initial surrounding scaffold and the challenges of alginate bead swelling and phase transitions in the collagen matrix were faced during the first assemblies of the system. The alginate bead swelling in the collagen was prevented by either the crosslinking of the alginate with Ba^{2+} and by adjusting the concentration of media components in the collagen to an equal amount prior to system assembly and gelation procedure. The crosslinking with Ba^{2+} prevented osmotic swelling of the beads during all the washing steps and the incorporation of the beads. This is attributed to the increased crosslinking efficiency of barium and the reduction in the exchange of counterions or other divalent ions that could be present in the system (98). By maintaining an equal amount of media components between the washed alginate beads and collagen solution, during gelation and incubation of the system transitions in the collagen matrix were avoided. The light band that was observed around the alginate bead during the initial experiments could be relevant to osmotic forces that contributed to the exchange of a certain amount of the bead's interface components and water to the point an equilibrium was met (126). The amount of water that was exchanged together with the components of the alginate to the compartment of the collagen probably generated a visible gradient around the bead that was accompanied by a looser collagen network (127). The thickness of the band formed around the alginate bead could indicate the magnitude of the osmotic forces that could be even further expanded under more rough conditions. Imaging of the adjusted scaffolds with SHG and CRM revealed the homogeneity and the integrity of the fibrillar collagen network. Brief estimation of the collagen pore sizes did not suggest any effects on cell confinement. Taking under consideration those results a method for the alginate beads incorporation that was used in further studies was established. The same technique was used to incorporate beads into Matrigel.

After the system was optimized, 1940DC were immobilized into the alginate microstructures and embedded into collagen scaffold with MF2. Cell viability of the 1940DC after encapsulation in the alginate was determined by incubating cells before and after the encapsulation with EthD-1 staining. By counting the overall signal of EthD-1 and of the eGFP, a percentage of non-viable cells could be estimated since in the presence of more compromised cells the EthD-1 signal would increase over the total population of cells. The viability was shown to be 10% reduced after the encapsulation and could be relevant to the exposure of the cells to relatively high concentration of calcium.

After assembly, the system was imaged in order to monitor migration. Initially, the effect of pro-inflammatory mediators was determined by measuring accumulation of MF2 in the specimen by cell counting. It was expected to meet the result of increased MF2 number around the alginate microstructures were pro-inflammatory mediators were secreted (128). The MF2 number increased exponentially after 24h and the accumulation around the alginate microstructures was distinct in contrast to the homogeneous spreading under the absence of 1940DC. Those events could not only be relevant to an increased proliferation of the MF2 under the influence of a pro-inflammatory stimulus but also to the migration of MF2 from other locations of the well.

To further characterize the dynamic migratory behavior of the MF2 cells, their motility was quantitated with automated cell tracking. Under pro-inflammatory conditions, a different profile was detected in the motility parameters of the MF2 cells as well as in their migratory behavior compared to absence of 1940DC. At this point it is important to note that comparison between the two different conditions at each timepoint regarding displacement and speed could not be accurate. Some higher values resulted in speed and displacement of single cells could be attributed to different architecture of the collagen, since the alignment of the fibers was random (54, 83, 86). Probably, the architecture in the sample where stimulated 1940DCs were absent, provided T-cells with local fibrillar structures that resembled more compact straightforward "railways", enabling thus long displacements and high speeds to be reached during certain timepoints (0h, 24h) (83). The comparison of motility progression throughout time in each condition is proposed as a more valuable approach. Another important factor that could influence the analysis could be the absence of a CO_2 chamber when the system was imaged. Temperature could have influenced the results to an extent while the time-lapse imaging lasted approximately for 30 min in ambient temperature.

A distinct difference in terms of cell mean speed and displacement profile throughout the acquisition timepoints could highlight that a pro-inflammatory microenvironment derived from LPS stimulated 1940DCs could influence the motility of the lymphocytes. The profile of the MF2 cells' mean speed and displacement remained consecutively stable under the entire first 24h acquisition timepoints, while motility parameters were highly increased at 48h. In the sample where an immune response was absent, migration speed and displacement were decreased significantly during the intermediate timepoints of 4h-8h, where secretion of pro-inflammatory cytokines after TLR4 stimulation has shown to be elevated (129). The fact that the mean speed of MF2 in the absence of an immune response at 24h was returned to the levels of 0h could be owed to the rest of the system after sequential acquisition for many hours. However, this fact did not seem to influence the behavior of the MF2 under inflammatory conditions. At 48h a distinct difference was obvious between the two different conditions that could be an outcome of an additional non-cognate interaction between the MF2 and the 1940DC (45, 130). 1940DCs that were at the outer part of the alginate structure could have established contact with MF2 cells that could lead to additional secretion of IL-12 and IFN-γ that stimulated the overall behavior (3).

Between the timepoints of acquisition, MF2 cells were detected surrounding encapsulated 1940DCs at the edges of the alginate. However, a moment of a direct contact has not been captured no matter that specific MF2 cells remained

surrounding a marginal 1940DC for enough time. It is uncertain whether alginate blocked the formation of stable cell-cell contacts or the thin alginate layer allowed instantaneous contacts to form. In addition, probable degradation of the alginate structures by free radicals produced after TLR stimulation should not be overlooked (131, 132). Instantaneous contacts on the other hand between surface molecules at the marginal region could not be excluded while it has been shown that short term, non-cognate, CD40/CD40L interactions, can occur without any involved TCR engagement (133). The interaction of the CD40 on the surface of the stimulated DCs with its ligand can lead to further secretion of IL-12 that could have induced further induced MF2 responses (29). Exposure of T helper subsets to IL-12 has highly stimulatory outcome that can explain the vast accumulation of the MF2 around the alginate (134).

Another plausible scenario that could explain the elevated activity in the presence of 1940DC at 48h could be attributed to the increased MF2 number and the over exposure of the 1940DC to debris. Current opinion supports that not only TLRs can confer to an innate immune response by the recognition of specific DAMPs and PAPMPs but additional C-lectin type receptors that can bind to cell debris and initiate a pro-inflammatory cytokine and chemokine cascade that induces the migration of cytotoxic T-cells (135). In the absence of flow in the system, the increased oxidative stress, the vast proliferation from the side of MF2 and the persistent exposure of DCs to damage associated molecular patterns DAMPs could explain the elevated activity that was observed at 48h. Hence, it could be possible that the effect could be correlated with a further innate immune mechanism than an adaptive one.

MF2 cells recorded speed values during the different timepoints that could resemble those found in interstitial matrices, which are mainly composed of fibrillar collagen (51). Interestingly, mean speed in the particular hydrogels overcame values that have been recorded in inflamed skin (51). Amoeboid migration is mainly characterized by lower speed levels compared to integrin dependent migration and amoeboid events in fibrillar collagen interfaces are expected (49). On the other hand, integrin dependent migration, not necessarily mesenchymal, could be met especially at 48h under the effect of inflamed 1940DC. Inflammatory microenvironments have shown to guide the transition to integrin dependent migration in T-cells, which is associated with relatively elevated values compared to non-adhesive amoeboid migration (136). Comparison with other *in vitro* systems would be complicated, since even in the current work collagen fiber alignment may have influenced the results. However, other studies based on collagen matrices have demonstrated remarkable values, relevant to maximal levels that have been recorded *in vivo* (52).

The migratory behavior of the MF2 cells was revealed to follow a superdiffussive fashion for the majority of the trajectories during all timepoints of acquisition in both with and without 1940DC in the alginate microstructures. The decrease in the alpha (α) exponent at the 4-6h timepoints could hold an explanation for the sample that was incubated under secretion of the pro-inflammatory cytokines. Under the abundance of proinflammatory cytokines and chemokines, migratory activity can be switched to exploitative with T-cells performing localized searches around DCs (53). On the other hand, the decrease in α values in the absence of a pro-inflammatory gradient cannot be explained and has a contradictory relationship

with the observations made under the presence of a cytokine gradient (53). At 8h under pro-inflammatory conditions, the character turned to more superdiffusive, but under any stimulus MF2 performed more exploitative subdiffusive searches similar to 6h based on the α values distribution.

During the first 8h timepoints, as mentioned above, cells underwent consecutive acquisition trials in the absence of CO_2 which, together with the effects of phototoxicity, may have influenced the results. At 24h the α values did not further increase for the sample where 1940DCs were present while were increased at the sample where 1940DCs where absent. A stable fraction of exploitative trajectories during pro-inflammatory responses should meet an expectation while cells are following a localized gradient and perform mostly localized movements. It is uncertain for the current system what led to the turnover to a more explorative search in terms of the non-inflamed microenvironment and the highly superdiffussive profile observed in the absence of stimulated 1940DCs. It could be relevant to longer rest and incubation time of the system or collagen architecture. However, according to behavioral ecology, superdiffussive walks are observed where there is lack of prey which could be associated with the extensive search by MF2 (137).

To this moment of discussion the observations get into conflict with previous works where α exponent values greater than 1.5 were assumed as a directed migration cutoff (54). Probably, the most intuitive timepoint to discuss on T-cell search strategies could be that of 48h. Without taking under consideration any numerical results, it was obvious that a further immune response was generated, and the migration of T-cells was vast with high velocities and longer track lengths. Despite that, a higher proportion of cells turned to a subdiffussive mode than the previous time points. An amount of MF2 cells for example, was persistently rotating around the alginate where 1940DCs were located close to the edges which would be translated as a subdiffusive-exploitative pattern. This is in agreement with the an accepted theory of movement ecology, where the amount of prey is abundant in the microenvironment and previous observations on T-cell motility patterns in inflamed lymph nodes (53, 137) . On the other hand, T-cells that covered larger distances in high speed, which was also distinguishable to previous time points, were observed. The biological reason of this highly ballistic behavior could be relevant to an increased pro-inflammatory gradient that led T-cells to cross large distances in order to reach the prey (53).

In general, a more cell intrinsic behavior was detected in all time points that could be further investigated on a single cell level, while different cells performed different migratory patterns. A more defined geometry in the system, since the alginate structures were of random shape, would facilitate the spatial investigation of the single cell events. Additionally, an alternative cell line or isolated peripheral blood lymphocytes could offer better insights to the actual molecular phenotype. MF2 is a hybridoma cell line and probably would not be a valuable candidate for differentiation studies. This fact restricts the suggestion of additional hypotheses could be made in the current system, that could support distinct motility patterns based on effector $CD4^+$ cell subtype differentiation. Interestingly, it has been shown in the inflamed skin that the motility patterns performed by Th1 cells was accompanied by a more subdiffusive profile while Th2 cells were characterized by more superdiffusive walks. The Th1 motility was chemokine dependent whereas

the Th2 was chemokine independent. However the chemokine dependent migration of Th1 cells was bypassed by ectopic expression of β_3 integrin subunit (51).

In terms of the numerical analysis using the MSD, the power law was fitted to the entire curve of each cell trajectory and by observation of the MSD curves, slight variations could be distinguished in between the time points denoting a transient behavior. The segmentation of the MSD curves and a power law fit in between certain intervals could give rise to an evolutionary profile of the α exponent versus time. This approach could be more effective in order to couple experimental data with recent theories that have been formulated in the field of theoretical movement ecology. This includes intermittent search strategies and superdiffusive Lévy walks where instantaneous exploitative patterns can be observed, whereas the overall behavior during the entire time interval would be characterized as superdiffusive (56, 137). Such events have been correlated with specialized T-cell subsets, where a local short subdiffusive event can be followed by a ballistic motion in a repetitive sequence to the moment a cognate antigen presented by an APC is found (138). In the same manner, probably specific single cell trajectories could be characterized by instantaneous localized events and rapidly translocated to another site in order to undergo a local search. Transient behavior of NK cells was observed by other authors in collagen matrix. The switch between different ameboid and mesenchymal migration modes was proposed as an explanation to the motility transition (54). The engineered microenvironment or the ECM composition has been shown to affect the motility of lymphocytes, but there is yet any concluding evidence and there is little known on how the motility is influenced on the level of T-T cell interactions (69). Elegant methods have been formulated in order to bring lymphocyte motility pattern analysis from experimental data to a more detailed level and account for transient behaviors (54, 59).

Finally, a great attention should be paid both in the analysis and in the experimental set up of acquisition in terms of the correct time interval selection. In the current system, the volume was imaged approximately every 3 minutes. The resulted 30 minutes time sequences where composed of 10 frames. A reduction in the resolution of the images would help to acquire more time frames and the analysis would have conducted in a more detailed manner. However, longer live cell imaging of 3h could be more effective in order to study longer tracks. In addition, by the establishment of longer acquisition intervals the timepoints of observation could be reduced to 0h, 12h, 24h and 48h. This application however, would require a CO_2 chamber at 37 ℃ and a microscope stage system that could compensate for drift.

6.2 Multi-compartmental hydrogels based on alginate and Matrigel

Matrigel was employed as a surrounding scaffold in the system and the MF2 infiltration was monitored. Matrigel as native basement membrane derivative lacks the fibrillar structure that is met in collagen and could indicate events related to matrix proteolysis under the influence of pro-inflammatory mediators. A remarkable effect of the pro-inflammatory signals on the capacity of the MF2 to migrate towards the alginate compartment was highlighted in the Matrigel multi-compartmental hydrogels. The distinct layer of MF2 cells that was formed around the alginate structure with the stimulated 1940DCs can support both directed

migration and matrix remodeling influenced by the pro-inflammatory microenvironment. It was obvious that the MF2 cell density was increased in the control sample and proteolysis of the scaffold cannot be excluded under non-inflamed conditions. However, in the presence of 1940DCs a more directed proteolysis could be proposed. Pro-inflammatory cytokines such as TNF-α, IL-1, IL-6 and IL-8 have shown to upregulate the production of MMPs(75, 76, 78, 139). The properties of Matrigel as a composite of native ECM substituents probably conferred to the immobilization of chemotactic compounds and provided haptotactic cues that upregulated matrix proteolysis to a specific direction (140). The diffusion of the pro-inflammatory factors from the 1940DCs encapsulated in the alginate through Matrigel could supposedly generate an instructive gradient, that contributed to the navigation of cells to the target (91). Observation of the time series during the initial acquisition shown that MF2 did not overcome barriers during their displacement that could be relevant to inadequate proteolysis leading to retrograde translocations and alternative path search. Additionally, the presence of MMP-2, and -9 as contaminants in Matrigel should not be excluded (141).

6.3 Multi-compartmental hydrogels based on alginate

There is little information on T-cell migration in alginate scaffolds and especially ionically crosslinked alginate hydrogels. Alginate is a naturally derived biopolymer that can be chemically modified and physically crosslinked while remaining non-toxic to the cells, providing a porous scaffold that could support cell migration. Chemically modified alginates were used as the surrounding scaffold in the system and the activity of the MF2 was monitored. No events were recorded in the multi-compartmental hydrogels where the T-cell embedded compartment was based on either sulfated or partially oxidized and reduced UPLVG alginate. Same features where observed both in the presence or absence of a pro-inflammatory microenvironment. Those observations came into conflict with the expectations based on the background which supports the independence to integrin binding sites during ameboid migration mode and the assumption that 3D motility is mediated by T-cell propulsive forces statically supported by the surrounding as a physical scaffold (142).

6.4 Migration of MF2 cells in RGD-alginate hydrogels

On the other hand, in the pilot experiment where MF2 motility was tested in RGD-alginate hydrogels, various events were recorded independent to any external stimulus since 1940DCs were not included in the setup. Directly proceeding to the attribution of the RGD-peptide sequence as the main causality of this locomotive outcome, could be disregarding to additional physical, chemical and biological sources that could have hindered motility in the sulfated alginate and POAred gels.

The motility could have been influenced by the gel stiffness while concentration of alginate in the RGD-alginate gels was lower (0,5%) than in the sulfated and partially oxidized alginate gels (1%) (96). Cell locomotion can be enhanced in a softer cell-scaffold interface since the physical confinement is rather limited than in stiffer interfaces that may be an outcome of higher polymeric network density (143). A lower concentration of calcium was used for the casting of the RGD-alginate scaffolds that probably had influenced the crosslinking density. In addition, in lower concentration the pore size is expected to be larger than in higher concentrations of alginate (96). Alginate concentration was not the only parameter

that would define the stiffness of the gel based on the empirical observation that POAred hydrogels were much softer due to the different chemical properties and the restriction of crosslinking sites (144, 145). However, in a recent study where RGD-alginate scaffolds were used in order to study T-cell migration in respect to stiffness shown increased migration and cell speed in stiffer scaffolds (113). There is an uncertainty from the description provided by the authors about the real 3D nature of the setup as T-cells where not initially immobilized into hydrogels and the alginate scaffolds were freeze dried and the cells where seeded afterwards. In the hydrogels used in the current project, greater cell speeds for individual trajectories were reported. In addition, activity was reported by the authors in non-modified alginate scaffolds.

There is little information that could support certain interactions that could occur in the T-cell/alginate interface. Non-modified alginate would retain its polyelectrolyte properties and the high degree of negative charges at pH 7,2-7,4. The formation of temporary complexes between the cell surface and the alginate characterized by low affinity that would not result to very "sticky" interactions could provide a supportive scaffold interface for the 3D cell movement. Biological factors of great significance that have been shown to mediate migration of immune cells and T-cell rolling in an integrin independent mechanism, are the CD44 (Hyaluronan receptor) and selectins (64). Specific interactions with mucinous moieties on the T-cell surface and the alginate could be supported by low extent shear forces that could take place between the cells and the alginate (146). However, great attention should be paid while formulating such hypotheses since the glycosylation of T-cells is highly dynamical in terms of modifications dependent on the activation and differentiation status (147). In that concept, the T-cells can move in the alginate porous network utilizing it as a physical scaffold.

Another point for discussion on the experimental setup would be relevant to the cell buffer used in the experiments were internal gelation was employed. The absence of basic metabolites such as amino acids that are detrimental in order to maintain the protein synthesis under sufficient levels in order to satisfy prerequisites for the optimal migration. This could have influenced the overall cell performance, while cells remained almost 3 h along the entire scaffold preparation and gelation procedure. Elevated activity during Day1 could be also relevant to acclimatization in the original media. Cell viability was not estimated in a way in order to make concrete suggestions.

In the RGD-alginate hydrogels, motility was examined and MF2 performed reasonable displacements especially at Day1 where single cells travelled distances greater than 40 μm in both 152kD and 237kD gel compositions. During Day1 the cell trajectories in the 152kD sample were found to be reduced. As an explanation for that, escape of the cells from the gels can be proposed. No cells were observed outside the gel and probably they were removed together with media before acquisition, but that still remains a hypothesis. In the 152kD sample, the displacement and the mean speed were found to be higher in general during Day0 and Day1. Single cell events occurring in the 237kD sample were showing an opposite trend such a long track that was observed in the 237kD sample at Day1 (≈90 μm). However, mean speed was higher in the 152kD sample during both timepoints and this could indicate a more unconfined motility in the 152kD gels where cells were able to obtain speeds higher than 0,1 μm/s corresponding to 6

μm/min. Supposedly, hydrogels composed of lower M_w alginates would have contributed to softer matrices while the incorporation of higher M_w would have resulted to stiffer gels (148). The results in that case indicate that longer displacements were allowed in a stiffer matrix composition while a softer scaffold may had provided an interface that facilitated faster migration.

The difference in the density of the cells that migrated at Day1 in both the molecular weights of alginate, is probably relevant to transitions that were situated in the porous alginate scaffolds. During the Day0 probably the scaffolds were constituted of very small pores that restricted motility to an extent. Probably, the 24h incubation that was followed influenced the pore sizes, and motility parameters like displacement and mean speed were increased due to reduction in cell confinement. The gel network could have undergone transitions relevant to swelling/shrinking and inhomogeneity during the steps where media was removed before the acquisition and afterwards gels were re-supplemented with fresh media. In those steps the Na^+ counterions contained in the media probably were competed the Ca-alginate crosslinks and loosened the network (98). The media formulation was used, on the other hand, contained an amount of Ca^{2+} that could balance the network changes to an extent. Lastly, longer incubation under the influence of media components such as FBS and amino acids that carry various charges may had influenced the gel network architecture (149).

Regarding the motility patterns that T-cells followed in the RGD-alginate matrix, an overall superdiffusive behavior was observed in terms of the α values distribution. However, those results could not be satisfactory to describe the realistic situation. The majority of cells wasn't displaced to long distances and probably the majority of the MSD curves would be descriptive to a minimal motility. This means, that displacements that recorder distances less than 20 μm could be relevant to cell blebbing or formation of protrusions and pseudopod elongation. Observation of the MSD curves could reveal that an overall transient behavior could characterize both molecular weight RGD-alginates during Day0 and Day1. Similar to collagen, because of such fluctuations observed in the graphs, fitting a power law to the entire MSD curve may have led to erroneous assumptions. Indeed, by observation of the time series, single cells performed remarkable displacements followed by pauses and subsequent backwards displacement that would agree with a subdiffusive regime. It was observable in certain trajectories that the motility followed a continuous fashion, but it was hindered after a certain point, probably because of barriers occurred in the porous alginate scaffolds that could not be penetrated by the T-cells. It cannot be excluded that deviations in motility would be relevant to possible mechanical transitions that resulted to an inhomogeneous network. Durotactic events may had taken place and MF2 migrated through a mechanical gradient, moving from a softer interface to a stiffer one (55).

6.5 Cell morphology in the different biomaterials

In addition to motility patterns cellular morphology in the different hydrogels could reveal significant properties of the microenvironment granted by the biomaterials that were employed. The different architecture and the structural components that each scaffold was composed provided a good reference in order to compare T-cell locomotion in distinct microenvironments.

The fibrillar scaffold that was composed of rat-tail collagen type-I was governed by a more universal type of motion with the cell motion not being interrupted for the motile MF2 by any barrier at least for approximately 30 min that imaging took place. The ruffling leading edge and the distinct uropod formation at the rear was found in many cells migrating in collagen. This morphology also is in agreement with the 2D migration in collagen coated surfaces and with intra-vital imaging where T-cells migrate in 3D inflamed skin collagen matrix (45, 51). The collagen fiber network as shown by SHG and CRM imaging was not very dense in order to confine the cell movement. It would be more likely that the T-cells followed the fibers (150). That could be a good reason that few extensive squeezing events were observed, in contrast to Matrigel.

In Matrigel the motility was shown to be underlined by a variable cell morphology. During the 30 min of imaging, some cells were shown to be constantly squeezed, performing a slow trailing edge traction that was accompanied by a penetrative leading edge sharp shape that could be correlated to a 3D lamellipodium. Other MF2 retained a more flattened morphology, but the dynamic formation of thin filamentous protrusions at the leading edge and transitions to a backward direction, that were not observed in collagen. However, there were some events where continuous migration was performed, resembling a more amoeboid shape alike collagen. Matrigel is composed by various native ECM components that include various GAG's and proteoglycans. The random alignment of Matrigel may result to an undefined architecture constituted by various ECM components, and lead to a more confined motional character where migration can be coupled to matrix degradation (151). Probably the dynamic morphology of the leading edge was an outcome of proteolytic activity and integrin binding. T-cells are capable to produce MMP-2 and -9 subsets are capable to degrade components such as collagen IV and laminin that are abundant in Matrigel (152). MMP-2 and -9 are either secreted or co-localized at the plasma membrane with integrin $\alpha_v\beta_3$ and $\alpha_v\beta_6$ respectively, which are found to be expressed in T-cell subsets, thus offering a drilling property in order to overcome certain degradable barriers (63, 152, 153). However, *in vivo* under inflammatory conditions additional cell types such as stromal cells and macrophages secrete various MMPs subsets that are either capable of directly degrade the ECM in order to facilitate T-cell infiltration (70). Thus, the endogenous secretion of MMPs by T-cells that is currently known to be restricted to MMP-2 and -9 could be the reason that the motility was hindered and retrograde events were observed.

In the RGD-alginate hydrogels where motility was monitored, motion appeared similar features to those observed in the Matrigel. Cell where squeezed in order to penetrate through narrow pores and retrograde events were seen during undegradable barriers of the alginate network. A fibrillar architecture was absent as in the Matrigel but instead cleavable sites by MMPs where not employed in the alginate. Certain events that were highlighted by highly localized on-spot motility could be attributed to narrow pores where MF2 were jammed during their effort to forward into the gel. In terms whether RGD functionalization would be necessary in order to render cell morphology through this certain type of motion can be controversial. There have been events that cell morphology could be correlated with an adhesive protrusion that mediated traction, while at specific time point the cells shown to migrate obtaining a flattened ameboid shape. On the one hand, studies support that T-cells do not require functional integrin elaboration in order

to penetrate elastic porous ECM structures of various composition, while actin network expansion has been proposed as the source of the protrusions formation, accompanied by heavily bundled actinomyosin contraction that lead to cell squeezing (142). On the other hand, the adhesive protrusions that had been formed could be relevant to RGD binding.

7 Future work

The multi-compartmental hydrogels that were employed in the current project showed promising results that could be improved in future work. The development of more standardized *in vitro* 3D platforms in the context of the current concept could provide more advanced systems for lymphoid tissue engineering and inflammation research. The screening of different biomaterials in the compartments can also offer new insights to the fabrication of 3D interfaces in order to study dynamical T-cell interactions with the surrounding scaffold.

Establishment of a more defined geometry by incorporation of microbeads would help to obtain additional information according to 3D distances of T-cells to the source of stimulus. Hybridoma T-cell lines are a good choice in order to screen the composition of a hydrogel as shown, but probably could not be a good choice for deeper investigation of phenotypic characteristics coupled to migration, that would offer valuable information to the field of immunology. A good choice for deeper molecular screening would include fluorescence activated cell sorting of peripheral blood isolated T-cells, for example, and staining of selected phenotypes with different fluorescent dyes. In this manner migration of certain T-cell subsets could be screened in the 3D scaffolds under the secretion of inflammatory mediators. Single cell tracking is a high throughput method and in respect to the high intrinsic motility of T-cells those systems can be screened for relatively short time intervals using a confocal microscope.

The acquisition of T-cell migration can be extended to a longer time interval by using a CO_2 chamber and controlled temperature. Scaling down the spatial dimensions of the system by the establishment of microwell based assays could provide a platform that could facilitate imaging of a defined volume. Encapsulation of an antigen with APCs and engineering of the microbead in order to enable migration of the T-cells inside could offer a good adoptive immunotherapy platform for the selection of antigen specific T-cell subsets.

Further methods could be implemented to answer important questions based on the interactions between T-cells and different 3D scaffold compositions. Live cell imaging of the actin cytoskeleton and of further molecular markers that are relevant to actin network, could reveal bundling of actin of T-cell interactions with different interfaces. Confocal reflectance microscopy combined with live cell imaging could be a proper method to investigate T-cell migration in the collagen scaffolds and interaction with the fibers.

The colocalization of matrix remodeling modules with integrins on the protrusions formed in Matrigel could be used to further investigate the ECM remodeling by invading T-cells. Alginate is a promising choice for future work due to its low toxicity, tunable gelling properties and flexibility in chemical modification. Further experimentation with M and G compositions and cross-linking ions in order to define an optimal porous architecture for cell motility could be used as an alternative scaffold that could be implemented into further 3D T-cell migration and activation studies. Furthermore, investigation of T-cell surface glycosylation and probable interactions with alginate would be an interesting topic for future research.

Lastly, the analysis of the migratory behavior during many pathological conditions is of great interest and can reveal patterns that can be coupled to T-cell phenotype and the tissue microenvironment. Further improvement of such analysis methods

is necessary and can offer a more advanced understanding of T-cell migration. Sliding time windows can contribute to a more efficient estimation of the progressive exponential motion character from the MSD graphs. MSD analysis multiplexed with distinct T-cell polarization moments, could provide a basis for the establishment of more sufficient standards for the definition of different T-cell search strategies.

8 Conclusion

In this work, multi-compartmental hydrogels were established as a platform in order to investigate T-cell migration in 3D under inflammatory conditions. Multi-compartmental hydrogels were composed of alginate encapsulated DCs embedded in surrounding scaffolds that contained T-cell hybridomas. The alginate compartment was successfully incorporated into surrounding collagen and Matrigel scaffolds. The collagen-alginate and Matrigel-alginate multi-compartmental hydrogels produced, could reflect the activity of T-cells under the influence of pro-inflammatory mediators. Encapsulation of APCs into alginate microstructures with the addition of TLR ligands can be considered as an effective method to reproduce a desired pro-inflammatory response.

The accumulation of T-cell hybridomas found to be elevated in the collagen-alginate system during the first 24h and increased exponentially at 48h compared to the absence of pro-inflammatory mediators. T-cell hybridomas exposed to pro-inflammatory mediators exhibited consistent levels of speed and displacement during the first 24h. At 48h, migration was elevated and significantly increased values were recorded. Upon exclusion of stimulated DCs from the system, the motility of T-cell hybridomas was downregulated during certain timepoints, while cell speed and displacement levels, did not exceed those of 0h. Thus, the presence of pro-inflammatory mediators secreted from stimulated DCs was found to augment the migration of T-cell hybridomas. The migratory behavior of T-cell hybridomas was underlined by varied character of local search events or long distant searches during all timepoints in both conditions. Fluctuations in the distribution of the search behavior were detected and discussed between the consecutive timepoints in each condition. In conclusion, in the multi-compartmental hydrogels based on alginate and collagen an efficient description of 3D T-cell migration under the influence of pro-inflammatory mediators could be accomplished. This system can be used as a platform for further detailed investigation of the current response or alternative immune responses.

In the multi-compartmental hydrogels based on alginate and Matrigel the migration of the T-cell hybridomas towards the DCs encapsulated in the alginate compartment was distinguishable, compared to the absence of pro-inflammatory mediators. The migration results in the Matrigel scaffolds could indicate directed migration coupled to matrix proteolysis.

The migration of T-cell hybridomas could not be demonstrated in the multi-compartmental hydrogels where sulfated or partially oxidized and reduced alginates where used as a surrounding matrix. However, those results cannot be disappointing and further optimization of the scaffolds in order to support migration may be necessary.

The 3D migration of T-cell hybridomas was successfully demonstrated in RGD-modified alginate hydrogels and the results indicated an effect of the molecular weight distribution in the motility parameters. After 24h of incubation, migration in the hydrogels was found to be enhanced probably due to transitions that occurred in the architecture of the alginate network.

T-cell hybridomas locomotion revealed a different morphology within the different biomaterials used during this project. Differences could be detected within the Matrigel and alginate scaffolds compared to collagen. In general, an ameboid shape

was more identical to collagen which could be correlated to the fibrillar architecture. In Matrigel the cell morphology was governed by mixed events, such as amoeboid shape or elongated cell shape that could be relevant to squeezing, adhesion and matrix proteolysis. In RGD-alginate the cell shape was described by an elongated shape that could be coupled to squeezing and integrin adhesion.

9 References

1. Medzhitov R. Origin and physiological roles of inflammation. Nature. 2008;454(7203):428-35.

2. Satoh T, Akira S. Toll-Like Receptor Signaling and Its Inducible Proteins. Microbiol Spectr. 2016;4(6).

3. Sabat R, Wolk K, Loyal L, Docke WD, Ghoreschi K. T cell pathology in skin inflammation. Semin Immunopathol. 2019;41(3):359-77.

4. Husebye H, Halaas Ø, Stenmark H, Tunheim G, Sandanger Ø, Bogen B, et al. Endocytic pathways regulate Toll-like receptor 4 signaling and link innate and adaptive immunity. The EMBO journal. 2006;25(4):683-92.

5. Thomas J. Kindt RAG, Barbara A. Osborne editor. KUBY Immunology 6th ed2007.

6. Rosa PM, Gopalakrishnan N, Ibrahim H, Haug M, Halaas Ø. The intercell dynamics of T cells and dendritic cells in a lymph node-on-a-chip flow device. Lab on a Chip. 2016;16(19):3728-40.

7. Di Modugno F, Colosi C, Trono P, Antonacci G, Ruocco G, Nisticò P. 3D models in the new era of immune oncology: focus on T cells, CAF and ECM. Journal of Experimental & Clinical Cancer Research. 2019;38(1):117.

8. Joffre O, Nolte MA, Spörri R, Sousa CRe. Inflammatory signals in dendritic cell activation and the induction of adaptive immunity. Immunological reviews. 2009;227(1):234-47.

9. Lemaitre B, Nicolas E, Michaut L, Reichhart J-M, Hoffmann JA. The dorsoventral regulatory gene cassette spätzle/Toll/cactus controls the potent antifungal response in Drosophila adults. Cell. 1996;86(6):973-83.

10. Satoh T, Akira S. Toll-like receptor signaling and its inducible proteins. Myeloid Cells in Health and Disease: A Synthesis. 2017:447-53.

11. Vogl T, Tenbrock K, Ludwig S, Leukert N, Ehrhardt C, Van Zoelen MA, et al. Mrp8 and Mrp14 are endogenous activators of Toll-like receptor 4, promoting lethal, endotoxin-induced shock. Nature medicine. 2007;13(9):1042-9.

12. Weiss J, Barker J. Diverse pro-inflammatory endotoxin recognition systems of mammalian innate immunity. F1000Res. 2018;7.

13. Esparza GA, Teghanemt A, Zhang D, Gioannini TL, Weiss JP. Endotoxin· albumin complexes transfer endotoxin monomers to MD-2 resulting in activation of TLR4. Innate immunity. 2012;18(3):478-91.

14. Kagan JC, Su T, Horng T, Chow A, Akira S, Medzhitov R. TRAM couples endocytosis of Toll-like receptor 4 to the induction of interferon-β. Nature immunology. 2008;9(4):361-8.

15. Zanoni I, Ostuni R, Marek LR, Barresi S, Barbalat R, Barton GM, et al. CD14 controls the LPS-induced endocytosis of Toll-like receptor 4. Cell. 2011;147(4):868-80.

16. Langenkamp A, Messi M, Lanzavecchia A, Sallusto F. Kinetics of dendritic cell activation: impact on priming of TH 1, TH 2 and nonpolarized T cells. Nature immunology. 2000;1(4):311-6.

17. Krangel MS. Gene segment selection in V(D)J recombination: accessibility and beyond. Nat Immunol. 2003;4(7):624-30.

18. Klein L, Kyewski B, Allen PM, Hogquist KA. Positive and negative selection of the T cell repertoire: what thymocytes see (and don't see). Nat Rev Immunol. 2014;14(6):377-91.

19. Williams MA, Bevan MJ. Effector and memory CTL differentiation. Annu Rev Immunol. 2007;25:171-92.

20. Iwasaki A, Medzhitov R. Regulation of adaptive immunity by the innate immune system. Science. 2010;327(5963):291-5.

21. Qian C, Cao X. Dendritic cells in the regulation of immunity and inflammation. Semin Immunol. 2018;35:3-11.

22. Hughes CE, Benson RA, Bedaj M, Maffia P. Antigen-presenting cells and antigen presentation in tertiary lymphoid organs. Frontiers in immunology. 2016;7:481.

23. Worbs T, Hammerschmidt SI, Forster R. Dendritic cell migration in health and disease. Nat Rev Immunol. 2017;17(1):30-48.

24. Natsuaki Y, Egawa G, Nakamizo S, Ono S, Hanakawa S, Okada T, et al. Perivascular leukocyte clusters are essential for efficient activation of effector T cells in the skin. Nat Immunol. 2014;15(11):1064-9.

25. Eisenbarth SC. Dendritic cell subsets in T cell programming: location dictates function. Nat Rev Immunol. 2019;19(2):89-103.

26. Tau G, Rothman P. Biologic functions of the IFN-γ receptors. Allergy. 1999;54(12):1233.

27. Pan J, Zhang M, Wang J, Wang Q, Xia D, Sun W, et al. Interferon-gamma is an autocrine mediator for dendritic cell maturation. Immunol Lett. 2004;94(1-2):141-51.

28. Yoo JK, Cho JH, Lee SW, Sung YC. IL-12 provides proliferation and survival signals to murine CD4+ T cells through phosphatidylinositol 3-kinase/Akt signaling pathway. J Immunol. 2002;169(7):3637-43.

29. Ma DY, Clark EA. The role of CD40 and CD154/CD40L in dendritic cells. Semin Immunol. 2009;21(5):265-72.

30. Bousso P. T-cell activation by dendritic cells in the lymph node: lessons from the movies. Nat Rev Immunol. 2008;8(9):675-84.

31. Jain A, Song R, Wakeland EK, Pasare C. T cell-intrinsic IL-1R signaling licenses effector cytokine production by memory CD4 T cells. Nat Commun. 2018;9(1):3185.

32. van den Bosch MHJ, van Lent P, van der Kraan PM. Identifying effector molecules, cells, and cytokines of innate immunity in OA. Osteoarthritis Cartilage. 2020.

33. Mehta AK, Gracias DT, Croft M. TNF activity and T cells. Cytokine. 2018;101:14-8.

34. Scheurich P, Thoma B, Ucer U, Pfizenmaier K. Immunoregulatory activity of recombinant human tumor necrosis factor (TNF)-alpha: induction of TNF receptors on human T cells and TNF-alpha-mediated enhancement of T cell responses. The Journal of Immunology. 1987;138(6):1786-90.

35. Angelot F, Seilles E, Biichle S, Berda Y, Gaugler B, Plumas J, et al. Endothelial cell-derived microparticles induce plasmacytoid dendritic cell maturation: potential implications in inflammatory diseases. Haematologica. 2009;94(11):1502-12.

36. Couper KN, Blount DG, Riley EM. IL-10: the master regulator of immunity to infection. J Immunol. 2008;180(9):5771-7.

37. Petrie RJ, Yamada KM. At the leading edge of three-dimensional cell migration. J Cell Sci. 2012;125(Pt 24):5917-26.

38. Giannone G, Dubin-Thaler BJ, Dobereiner HG, Kieffer N, Bresnick AR, Sheetz MP. Periodic lamellipodial contractions correlate with rearward actin waves. Cell. 2004;116(3):431-43.

39. Driscoll MK, Welf ES, Jamieson AR, Dean KM, Isogai T, Fiolka R, et al. Robust and automated detection of subcellular morphological motifs in 3D microscopy images. Nat Methods. 2019;16(10):1037-44.

40. Jacquemet G, Hamidi H, Ivaska J. Filopodia in cell adhesion, 3D migration and cancer cell invasion. Curr Opin Cell Biol. 2015;36:23-31.

41. Petrie RJ, Gavara N, Chadwick RS, Yamada KM. Nonpolarized signaling reveals two distinct modes of 3D cell migration. J Cell Biol. 2012;197(3):439-55.

42. Eddy RJ, Weidmann MD, Sharma VP, Condeelis JS. Tumor Cell Invadopodia: Invasive Protrusions that Orchestrate Metastasis. Trends Cell Biol. 2017;27(8):595-607.

43. Cougoule C, Lastrucci C, Guiet R, Mascarau R, Meunier E, Lugo-Villarino G, et al. Podosomes, But Not the Maturation Status, Determine the Protease-Dependent 3D Migration in Human Dendritic Cells. Front Immunol. 2018;9:846.

44. Wolf K, Muller R, Borgmann S, Brocker EB, Friedl P. Amoeboid shape change and contact guidance: T-lymphocyte crawling through fibrillar collagen is independent of matrix remodeling by MMPs and other proteases. Blood. 2003;102(9):3262-9.

45. Dupré L, Houmadi R, Tang C, Rey-Barroso J. Lymphocyte Migration: An Action Movie Starring the Actin and Associated Actors. Front Immunol. 2015; 6: 586.

46. Friedl P, Weigelin B. Interstitial leukocyte migration and immune function. Nat Immunol. 2008;9(9):960-9.

47. Murray J, Vawter-Hugart H, Voss E, Soll DR. Three-dimensional motility cycle in leukocytes. Cell Motil Cytoskeleton. 1992;22(3):211-23.

48. Friedl P, Entschladen F, Conrad C, Niggemann B, Zanker KS. CD4+ T lymphocytes migrating in three-dimensional collagen lattices lack focal adhesions and utilize beta1 integrin-independent strategies for polarization, interaction with collagen fibers and locomotion. Eur J Immunol. 1998;28(8):2331-43.

49. Katakai T, Habiro K, Kinashi T. Dendritic cells regulate high-speed interstitial T cell migration in the lymph node via LFA-1/ICAM-1. The Journal of Immunology. 2013;191(3):1188-99.

50. Lämmermann T, Bader BL, Monkley SJ, Worbs T, Wedlich-Söldner R, Hirsch K, et al. Rapid leukocyte migration by integrin-independent flowing and squeezing. Nature. 2008;453(7191):51-5.

51. Gaylo-Moynihan A, Prizant H, Popovic M, Fernandes NRJ, Anderson CS, Chiou KK, et al. Programming of Distinct Chemokine-Dependent and -Independent Search Strategies for Th1 and Th2 Cells Optimizes Function at Inflamed Sites. Immunity. 2019;51(2):298-309.e6.

52. Friedl P, Brocker EB. T cell migration in three-dimensional extracellular matrix: guidance by polarity and sensations. Dev Immunol. 2000;7(2-4):249-66.

53. Krummel MF, Bartumeus F, Gerard A. T cell migration, search strategies and mechanisms. Nat Rev Immunol. 2016;16(3):193-201.

54. Olofsson PE, Brandt L, Magnusson KEG, Frisk T, Jalden J, Onfelt B. A collagen-based microwell migration assay to study NK-target cell interactions. Sci Rep. 2019;9(1):10672.

55. Ebata H, Moriyama K, Kuboki T, Kidoaki S. General cellular durotaxis induced with cell-scale heterogeneity of matrix-elasticity. Biomaterials. 2020;230:119647.

56. Bénichou O, Loverdo C, Moreau M, Voituriez R. Intermittent search strategies. Reviews of Modern Physics. 2011;83(1):81.

57. Harris TH, Banigan EJ, Christian DA, Konradt C, Tait Wojno ED, Norose K, et al. Generalized Levy walks and the role of chemokines in migration of effector CD8+ T cells. Nature. 2012;486(7404):545-8.

58. Sarris M, Sixt M. Navigating in tissue mazes: chemoattractant interpretation in complex environments. Curr Opin Cell Biol. 2015;36:93-102.

59. Sadjadi Z, Zhao R, Hoth M, Qu B, Rieger H. Migration of Cytotoxic T Lymphocytes in 3D Collagen Matrices. arXiv preprint arXiv:200105331. 2020.

60. Ebert LM, Schaerli P, Moser B. Chemokine-mediated control of T cell traffic in lymphoid and peripheral tissues. Mol Immunol. 2005;42(7):799-809.

61. Malhotra D, Fletcher AL, Astarita J, Lukacs-Kornek V, Tayalia P, Gonzalez SF, et al. Transcriptional profiling of stroma from inflamed and resting lymph nodes defines immunological hallmarks. Nat Immunol. 2012;13(5):499-510.

62. Tweedy L, Susanto O, Insall RH. Self-generated chemotactic gradients-cells steering themselves. Curr Opin Cell Biol. 2016;42:46-51.

63. Bertoni A, Alabiso O, Galetto AS, Baldanzi G. Integrins in T Cell Physiology. Int J Mol Sci. 2018;19(2).

64. Suzuki T, Suzuki M, Ogino S, Umemoto R, Nishida N, Shimada I. Mechanical force effect on the two-state equilibrium of the hyaluronan-binding domain of CD44 in cell rolling. Proceedings of the National Academy of Sciences. 2015;112(22):6991-6.

65. Lasky LA, Singer MS, Dowbenko D, Imai Y, Henzel WJ, Grimley C, et al. An endothelial ligand for L-selectin is a novel mucin-like molecule. Cell. 1992;69(6):927-38.

66. Carlow DA, Tra MC, Ziltener HJ. A cell-extrinsic ligand acquired by activated T cells in lymph node can bridge L-selectin and P-selectin. PLoS One. 2018;13(10):e0205685.

67. Limanjaya I, Hsu TI, Chuang JY, Kao TJ. L-selectin activation regulates Rho GTPase activity via Ca(+2) influx in Sertoli cell line, ASC-17D cells. Biochem Biophys Res Commun. 2020;525(4):1011-7.

68. Brenner B, Gulbins E, Busch GL, Koppenhoefer U, Lang F, Linderkamp O. L-selectin regulates actin polymerisation via activation of the small G-protein Rac2. Biochemical and biophysical research communications. 1997;231(3):802-7.

69. Gaylo A, Schrock DC, Fernandes NR, Fowell DJ. T Cell Interstitial Migration: Motility Cues from the Inflamed Tissue for Micro- and Macro-Positioning. Front Immunol. 2016;7:428.

70. Sorokin L. The impact of the extracellular matrix on inflammation. Nat Rev Immunol. 2010;10(10):712-23.

71. Naghieh S, Karamooz-Ravari MR, Sarker M, Karki E, Chen X. Influence of crosslinking on the mechanical behavior of 3D printed alginate scaffolds: Experimental and numerical approaches. Journal of the mechanical behavior of biomedical materials. 2018;80:111-8.

72. Korpos E, Wu C, Song J, Hallmann R, Sorokin L. Role of the extracellular matrix in lymphocyte migration. Cell and tissue research. 2010;339(1):47-57.

73. Lokmic Z, Lämmermann T, Sixt M, Cardell S, Hallmann R, Sorokin L, editors. The extracellular matrix of the spleen as a potential organizer of immune cell compartments. Seminars in immunology; 2008: Elsevier.

74. Hynes RO. The extracellular matrix: not just pretty fibrils. Science. 2009;326(5957):1216-9.

75. Robinson SC, Scott KA, Balkwill FR. Chemokine stimulation of monocyte matrix metalloproteinase-9 requires endogenous TNF-alpha. Eur J Immunol. 2002;32(2):404-12.

76. El-Shabrawi Y, Walch A, Hermann J, Egger G, Foster CS. Inhibition of MMP-dependent chemotaxis and amelioration of experimental autoimmune uveitis with a selective metalloproteinase-2 and -9 inhibitor. J Neuroimmunol. 2004;155(1-2):13-20.

77. Edsparr K, Basse PH, Goldfarb RH, Albertsson P. Matrix metalloproteinases in cytotoxic lymphocytes impact on tumour infiltration and immunomodulation. Cancer Microenviron. 2011;4(3):351-60.

78. Aigner T, McKenna L, Zien A, Fan Z, Gebhard PM, Zimmer R. Gene expression profiling of serum-and interleukin-1β-stimulated primary human adult articular chondrocytes–A molecular analysis based on chondrocytes isolated from one donor. Cytokine. 2005;31(3):227-40.

79. Porée B, Kypriotou M, Chadjichristos C, Beauchef G, Renard E, Legendre F, et al. Interleukin-6 (IL-6) and/or soluble IL-6 receptor down-regulation of human type II collagen gene expression in articular chondrocytes requires a decrease of Sp1· Sp3 ratio and of the binding activity of both factors to the COL2A1 promoter. Journal of Biological Chemistry. 2008;283(8):4850-65.

80. Kuen J, Darowski D, Kluge T, Majety M. Pancreatic cancer cell/fibroblast co-culture induces M2 like macrophages that influence therapeutic response in a 3D model. PloS one. 2017;12(7).

81. Sun W, Luo Z, Lee J, Kim HJ, Lee K, Tebon P, et al. Organ-on-a-Chip for Cancer and Immune Organs Modeling. Advanced healthcare materials. 2019;8(4):1801363.

82. Alberts B JA, Lewis J, et al. Molecular Biology of the Cell. 4th edition. New York: Garland Science; 2002. The Extracellular Matrix of Animals. Available from: https://www.ncbi.nlm.nih.gov/books/NBK26810/.

83. Pruitt HC, Lewis D, Ciccaglione M, Connor S, Smith Q, Hickey JW, et al. Collagen fiber structure guides 3D motility of cytotoxic T lymphocytes. Matrix Biol. 2020;85-86:147-59.

84. Eyre DR, Paz MA, Gallop PM. Cross-linking in collagen and elastin. Annu Rev Biochem. 1984;53:717-48.

85. Fraley SI, Wu P-h, He L, Feng Y, Krisnamurthy R, Longmore GD, et al. Three-dimensional matrix fiber alignment modulates cell migration and MT1-MMP utility by spatially and temporally directing protrusions. Scientific reports. 2015;5(1):1-13.

86. Wu P-H, Gilkes DM, Wirtz D. The biophysics of 3D cell migration. Annual Review of Biophysics. 2018;47:549-67.

87. Kleinman HK, Martin GR. Matrigel: basement membrane matrix with biological activity. Semin Cancer Biol. 2005;15(5):378-86.

88. Wang J, Chu R, Ni N, Nan G. The effect of Matrigel as scaffold material for neural stem cell transplantation for treating spinal cord injury. Sci Rep. 2020;10(1):2576.

89. Polykandriotis E, Arkudas A, Horch RE, Kneser U, Mitchell G. To matrigel or not to matrigel. The American journal of pathology. 2008;172(5):1441-2.

90. Huch M, Knoblich JA, Lutolf MP, Martinez-Arias A. The hope and the hype of organoid research. Development. 2017;144(6):938-41.

91. Tsai S, McOlash L, Palen K, Johnson B, Duris C, Yang Q, et al. Development of primary human pancreatic cancer organoids, matched stromal and immune cells and 3D tumor microenvironment models. BMC Cancer. 2018;18(1):335.

92. Osswald A, Hedrich V, Sommergruber W. 3D-3 Tumor Models in Drug Discovery for Analysis of Immune Cell Infiltration. Methods Mol Biol. 2019;1953:151-62.

93. Govan J, Fyfe J, Jarman T. Isolation of alginate-producing mutants of Pseudomonas fluorescens, Pseudomonas putida and Pseudomonas mendocina. Microbiology. 1981;125(1):217-20.

94. Draget KI, Smidsrød O, Skjåk-Bræk G. Alginates from algae. Biopolymers Online: Biology• Chemistry• Biotechnology• Applications. 2005;6.

95. Gorin P, Spencer J. Exocellular alginic acid from Azotobacter vinelandii. Canadian journal of chemistry. 1966;44(9):993-8.

96. Smidsrød O, Skja G. Alginate as immobilization matrix for cells. Trends in biotechnology. 1990;8:71-8.

97. Skjåk-Bræk G, Donati I, Paoletti S. Alginate hydrogels: properties and applications. Polysaccharide Hydrogels: Characterization and Biomedical Applications. 2015:443-92.

98. Morch YA, Donati I, Strand BL, Skjak-Braek G. Effect of Ca2+, Ba2+, and Sr2+ on alginate microbeads. Biomacromolecules. 2006;7(5):1471-80.

99. Andersen T, Strand BL, Formo K, Alsberg E, Christensen BE. Carbohydrate Chemistry. 2012.

100. Hals IK, Rokstad AM, Strand BL, Oberholzer J, Grill V. Alginate microencapsulation of human islets does not increase susceptibility to acute hypoxia. J Diabetes Res. 2013;2013:374925.

101. Qi M, Mørch Y, Lacík I, Formo K, Marchese E, Wang Y, et al. Survival of human islets in microbeads containing high guluronic acid alginate crosslinked with Ca2+ and Ba2+. Xenotransplantation. 2012;19(6):355-64.

102. Johansen A, Flink JM. Immobilization of yeast cells by internal gelation of alginate. Enzyme and microbial technology. 1986;8(3):145-8.

103. Yang D, Jones KS. Effect of alginate on innate immune activation of macrophages. Journal of Biomedical Materials Research Part A: An Official Journal of The Society for Biomaterials, The Japanese Society for Biomaterials, and The Australian Society for Biomaterials and the Korean Society for Biomaterials. 2009;90(2):411-8.

104. Fang W, Bi D, Zheng R, Cai N, Xu H, Zhou R, et al. Identification and activation of TLR4-mediated signalling pathways by alginate-derived guluronate oligosaccharide in RAW264. 7 macrophages. Scientific reports. 2017;7(1):1-13.

105. Fan Y, Li Y, Zhang J, Ding X, Cui J, Wang G, et al. Alginate enhances memory properties of antitumor CD8+ T Cells by promoting cellular antioxidation. ACS Biomaterials Science & Engineering. 2019;5(9):4717-25.

106. Dalheim MØ, Vanacker J, Najmi MA, Aachmann FL, Strand BL, Christensen BE. Efficient functionalization of alginate biomaterials. Biomaterials. 2016;80:146-56.

107. Arlov O, Skjak-Braek G. Sulfated Alginates as Heparin Analogues: A Review of Chemical and Functional Properties. Molecules. 2017;22(5).

108. Wright B, De Bank PA, Luetchford KA, Acosta FR, Connon CJ. Oxidized alginate hydrogels as niche environments for corneal epithelial cells. J Biomed Mater Res A. 2014;102(10):3393-400.

109. Reakasame S, Boccaccini AR. Oxidized alginate-based hydrogels for tissue engineering applications: a review. Biomacromolecules. 2018;19(1):3-21.

110. Hori Y, Winans AM, Huang CC, Horrigan EM, Irvine DJ. Injectable dendritic cell-carrying alginate gels for immunization and immunotherapy. Biomaterials. 2008;29(27):3671-82.

111. Shah NJ, Mao AS, Shih TY, Kerr MD, Sharda A, Raimondo TM, et al. An injectable bone marrow-like scaffold enhances T cell immunity after hematopoietic stem cell transplantation. Nat Biotechnol. 2019;37(3):293-302.

112. Florczyk SJ, Liu G, Kievit FM, Lewis AM, Wu JD, Zhang M. 3D porous chitosan–alginate scaffolds: a new matrix for studying prostate cancer cell–lymphocyte interactions in vitro. Advanced healthcare materials. 2012;1(5):590-9.

113. Majedi FS, Hasani-Sadrabadi MM, Thauland TJ, Li S, Bouchard L-S, Butte MJ. T-cell activation is modulated by the 3D mechanical microenvironment. Biomaterials. 2020:120058.

114. Prasad V, Semwogerere D, Weeks ER. Confocal microscopy of colloids. Journal of Physics: Condensed Matter. 2007;19(11):113102.

115. Haug B, Nordgård CT, Draget KI, Bjørkøy A. Confocal reflectance microscopy and multiple particle tracking for the study of the gelation of biopolymers. 2018.

116. Braga JCT, Scope A, Klaz I, Mecca P, González S, Rabinovitz H, et al. The significance of reflectance confocal microscopy in the assessment of solitary pink skin lesions. Journal of the American Academy of Dermatology. 2009;61(2):230-41.

117. Bianchini P, Diaspro A. Second Harmonic Generation Microscopy (SHG). In: Roberts GCK, editor. Encyclopedia of Biophysics. Berlin, Heidelberg: Springer Berlin Heidelberg; 2013. p. 2280-3.

118. Chen X, Nadiarynkh O, Plotnikov S, Campagnola PJ. Second harmonic generation microscopy for quantitative analysis of collagen fibrillar structure. Nat Protoc. 2012;7(4):654-69.

119. Arlov Ø, Aachmann FL, Sundan A, Espevik T, Skjaˊk-Bræk G. Heparin-like properties of sulfated alginates with defined sequences and sulfation degrees. Biomacromolecules. 2014;15(7):2744-50.

120. Vold IMN, Kristiansen KA, Christensen BE. A study of the chain stiffness and extension of alginates, in vitro epimerized alginates, and periodate-oxidized alginates using size-exclusion chromatography combined with light scattering and viscosity detectors. Biomacromolecules. 2006;7(7):2136-46.

121. Fuertes Marraco SA, Grosjean F, Duval A, Rosa M, Lavanchy C, Ashok D, et al. Novel murine dendritic cell lines: a powerful auxiliary tool for dendritic cell research. Frontiers in immunology. 2012;3:331.

122. Zhao Y, Boczkowski D, Nair SK, Gilboa E. Inhibition of invariant chain expression in dendritic cells presenting endogenous antigens stimulates CD4+ T-cell responses and tumor immunity. Blood. 2003;102(12):4137-42.

123. Strand B, Gåserød O, Kulseng B, Espevik T, Skjåk-Bræk G. Alginate-polylysine-alginate microcapsules: effect of size reduction on capsule properties. Journal of microencapsulation. 2002;19(5):615-30.

124. Tinevez JY, Perry N, Schindelin J, Hoopes GM, Reynolds GD, Laplantine E, et al. TrackMate: An open and extensible platform for single-particle tracking. Methods. 2017;115:80-90.

125. Tarantino N, Tinevez JY, Crowell EF, Boisson B, Henriques R, Mhlanga M, et al. TNF and IL-1 exhibit distinct ubiquitin requirements for inducing NEMO-IKK supramolecular structures. J Cell Biol. 2014;204(2):231-45.

126. Saar G, Shinar H, Navon G. Comparison of the effects of mechanical and osmotic pressures on the collagen fiber architecture of intact and proteoglycan-depleted articular cartilage. European Biophysics Journal. 2007;36(4-5):529-38.

127. Masic A, Bertinetti L, Schuetz R, Chang SW, Metzger TH, Buehler MJ, et al. Osmotic pressure induced tensile forces in tendon collagen. Nat Commun. 2015;6:5942.

128. Hamann A, Syrbe U. T-cell trafficking into sites of inflammation. Rheumatology. 2000;39(7):696-9.

129. Langenkamp A, Messi M, Lanzavecchia A, Sallusto F. Kinetics of dendritic cell activation: impact on priming of TH1, TH2 and nonpolarized T cells. Nat Immunol. 2000;1(4):311-6.

130. Onishi Y, Fehervari Z, Yamaguchi T, Sakaguchi S. Foxp3+ natural regulatory T cells preferentially form aggregates on dendritic cells in vitro and actively inhibit their maturation. Proc Natl Acad Sci U S A. 2008;105(29):10113-8.

131. Oberkampf M, Guillerey C, Mouries J, Rosenbaum P, Fayolle C, Bobard A, et al. Mitochondrial reactive oxygen species regulate the induction of CD8(+) T cells by plasmacytoid dendritic cells. Nat Commun. 2018;9(1):2241.

132. Smidsrod O, Haug A, Larsen BR. Degradation of alginate in the presence of reducing compounds. Acta Chem Scand. 1963;17(10):2628-37.

133. Pasqual G, Chudnovskiy A, Tas JMJ, Agudelo M, Schweitzer LD, Cui A, et al. Monitoring T cell-dendritic cell interactions in vivo by intercellular enzymatic labelling. Nature. 2018;553(7689):496-500.

134. Vacaflores A, Chapman NM, Harty JT, Richer MJ, Houtman JC. Exposure of Human CD4 T Cells to IL-12 Results in Enhanced TCR-Induced Cytokine Production, Altered TCR Signaling, and Increased Oxidative Metabolism. PLoS One. 2016;11(6):e0157175.

135. Drouin M, Saenz J, Chiffoleau E. C-Type Lectin-Like Receptors: Head or Tail in Cell Death Immunity. Front Immunol. 2020;11:251.

136. Walling BL, Kim M. LFA-1 in T cell migration and differentiation. Frontiers in immunology. 2018;9:952.

137. Viswanathan GM. Ecology: Fish in Levy-flight foraging. Nature. 2010;465(7301):1018-9.

138. Harris TH, Banigan EJ, Christian DA, Konradt C, Wojno EDT, Norose K, et al. Generalized Lévy walks and the role of chemokines in migration of effector CD8+ T cells. Nature. 2012;486(7404):545-8.

139. Poree B, Kypriotou M, Chadjichristos C, Beauchef G, Renard E, Legendre F, et al. Interleukin-6 (IL-6) and/or soluble IL-6 receptor down-regulation of human type II collagen gene expression in articular chondrocytes requires a decrease of Sp1.Sp3 ratio and of the binding activity of both factors to the COL2A1 promoter. J Biol Chem. 2008;283(8):4850-65.

140. Tanino Y, Coombe DR, Gill SE, Kett WC, Kajikawa O, Proudfoot AEI, et al. Kinetics of Chemokine–Glycosaminoglycan Interactions Control Neutrophil Migration into the Airspaces of the Lungs. The Journal of Immunology. 2010;184(5):2677-85.

141. Mackay AR, Gomez DE, Cottam DW, Rees RC, Nason AM, Thorgeirsson UP. Identification of the 72-kDa (MMP-2) and 92-kDa (MMP-9) gelatinase/type IV collagenase in preparations of laminin and Matrigel. Biotechniques. 1993;15(6):1048-51.

142. Woolf E, Grigorova I, Sagiv A, Grabovsky V, Feigelson SW, Shulman Z, et al. Lymph node chemokines promote sustained T lymphocyte motility without triggering stable integrin adhesiveness in the absence of shear forces. Nat Immunol. 2007;8(10):1076-85.

143. Ehrbar M, Sala A, Lienemann P, Ranga A, Mosiewicz K, Bittermann A, et al. Elucidating the role of matrix stiffness in 3D cell migration and remodeling. Biophysical journal. 2011;100(2):284-93.

144. Augst AD, Kong HJ, Mooney DJ. Alginate hydrogels as biomaterials. Macromolecular bioscience. 2006;6(8):623-33.

145. Kristiansen KA, Schirmer BC, Aachmann FL, Skjåk-Bræk G, Draget KI, Christensen BE. Novel alginates prepared by independent control of chain stiffness and distribution of G-residues: Structure and gelling properties. Carbohydrate polymers. 2009;77(4):725-35.

146. Sletmoen M, Maurstad G, Nordgård CT, Draget KI, Stokke BT. Oligoguluronate induced competitive displacement of mucin–alginate interactions: relevance for mucolytic function. Soft Matter. 2012;8(32):8413-21.

147. De Bousser E, Meuris L, Callewaert N, Festjens N. Human T cell glycosylation and implications on immune therapy for cancer. Hum Vaccin Immunother. 2020:1-15.

148. Draget K, Bræk GS, Smidsrød O. Alginic acid gels: the effect of alginate chemical composition and molecular weight. Carbohydrate Polymers. 1994;25(1):31-8.

149. Neiser S, Draget K, Smidsrød O. Interactions in bovine serum albumin–calcium alginate gel systems. Food hydrocolloids. 1999;13(6):445-58.

150. Wolf K, Müller R, Borgmann S, Brocker E-B, Friedl P. Amoeboid shape change and contact guidance: T-lymphocyte crawling through fibrillar collagen is independent of matrix remodeling by MMPs and other proteases. Blood. 2003;102(9):3262-9.

151. Jang JM, Tran SH, Na SC, Jeon NL. Engineering controllable architecture in matrigel for 3D cell alignment. ACS Appl Mater Interfaces. 2015;7(4):2183-8.

152. Abraham M, Shapiro S, Karni A, Weiner HL, Miller A. Gelatinases (MMP-2 and MMP-9) are preferentially expressed by Th1 vs. Th2 cells. J Neuroimmunol. 2005;163(1-2):157-64.

153. Cayrol F, Sterle HA, Diaz Flaque MC, Barreiro Arcos ML, Cremaschi GA. Non-genomic Actions of Thyroid Hormones Regulate the Growth and Angiogenesis of T Cell Lymphomas. Front Endocrinol (Lausanne). 2019;10:63.

10 Appendix: Supplementary movies description

S1 Supplementary movie: 0h collagen-alginate multi-compartmental hydrogel. 2x zoomed, 3D reconstruction, 30 minutes time-series of MF2 cells (red) and LPS stimulated 1940DCs (green). Movie time conversion: 3 fps (frames per second). Original time frame: 208 s. Original time

S2 Supplementary movie: 24h collagen-alginate multi-compartmental hydrogel. 2x zoomed, 3D reconstruction, 30 minutes time-series of MF2 cells (red) and LPS stimulated 1940DCs (green). Movie time conversion: 3 fps (frame per second). Original time frame: 200 s.

S3 Supplementary movie: 48h collagen-alginate multi-compartmental hydrogel. 2x zoomed, 3D reconstruction, 30 minutes time-series of MF2 cells (red) and LPS stimulated 1940DCs (green). Movie time conversion: 3 fps (frames per second). Original time frame: 200 s.

S4 Supplementary movie: Migration in Matrigel. 2x zoomed, 3D reconstruction, 30 minutes time-series of MF2 cells (red) migrating in Matrigel at 0h. Movie time conversion: 3 fps (frames per second). Original time frame: 58 s.

S5 Supplementary movie: Sulfated alginate hydrogel. 2x zoomed, 3D reconstruction, 10 minutes time-series of MF2 cells (red) immobilized in sulfated alginate hydrogel at 48h. Movie time conversion: 3 fps (frames per second). Original time frame: 67 s.

S6 Supplementary movie: POAred alginate hydrogel. 2x zoomed, 3D reconstruction, 30 minutes time-series of MF2 cells (red) immobilized in POAred alginate hydrogel at 0h. Movie time conversion: 3 fps (frames per second). Original time frame: 200 s.

S7 Supplementary movie: Migration in RGD-alginate hydrogel. 2x zoomed, 3D reconstruction, 30 minutes time-series of MF2 cells (red) migrating in RGD-alginate hydrogel at 24h (Day1) (RGD:UPLVG 152kD). Movie time conversion: 3 fps (frames per second). Original time frame: 58 s.

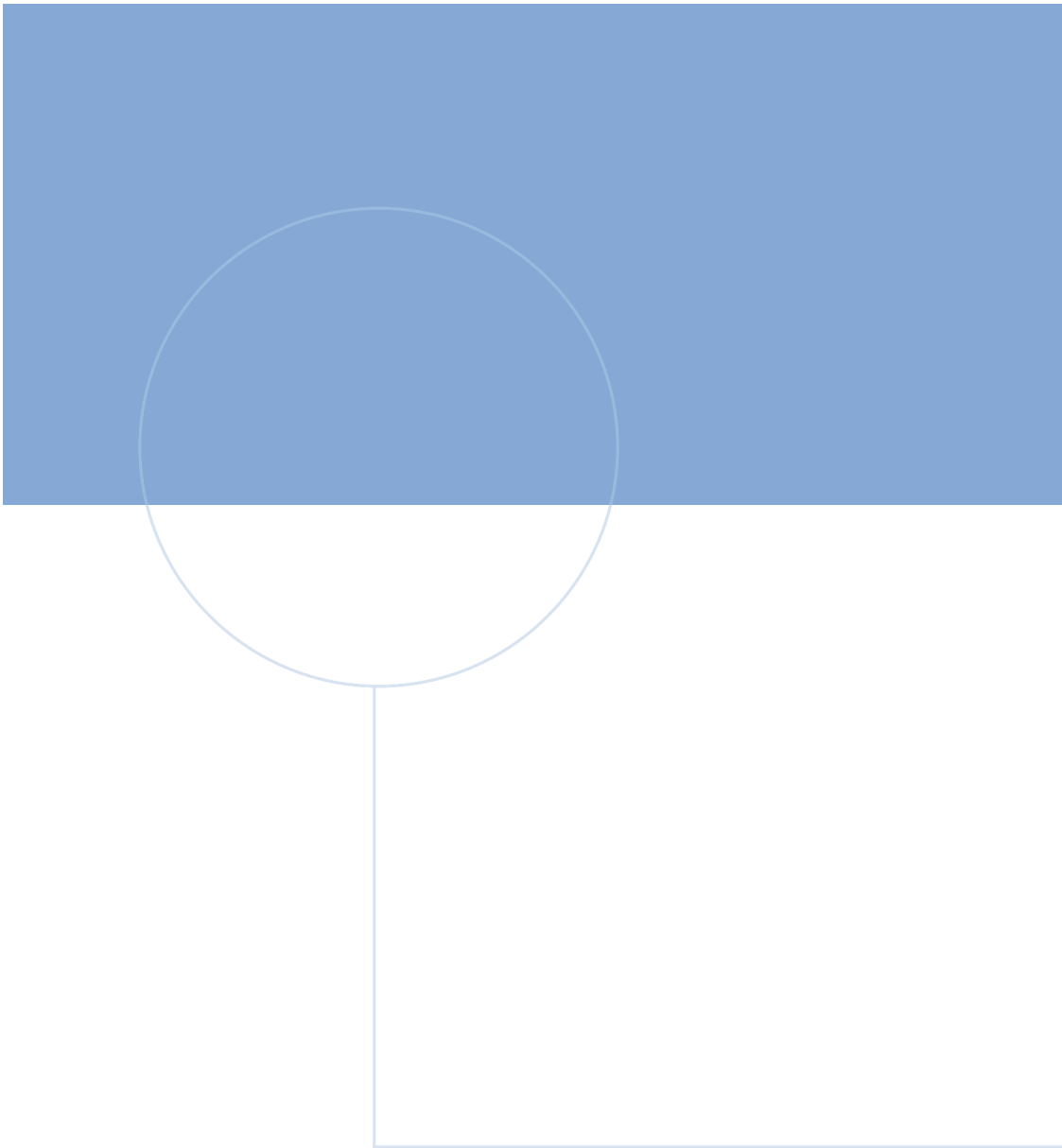

NTNU

Norwegian University of
Science and Technology